NASA Technical Paper 3559

Aerodynamic Characteristics of Two Waverider-Derived Hypersonic Cruise Configurations

Charles E. Cockrell, Jr., Lawrence D. Huebner, and Dennis B. Finley

July 1996

NASA Technical Paper 3559

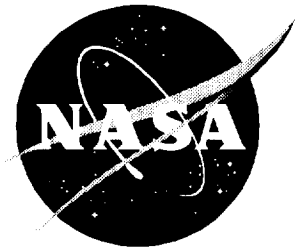

Aerodynamic Characteristics of Two Waverider-Derived Hypersonic Cruise Configurations

Charles E. Cockrell, Jr. and Lawrence D. Huebner
Langley Research Center • Hampton, Virginia

Dennis B. Finley
Lockheed-Fort Worth Company • Fort Worth, Texas

National Aeronautics and Space Administration
Langley Research Center • Hampton, Virginia 23681-0001

July 1996

Available electronically at the following URL address: http://techreports.larc.nasa.gov/ltrs/ltrs.html

Printed copies available from the following:

NASA Center for AeroSpace Information
800 Elkridge Landing Road
Linthicum Heights, MD 21090-2934
(301) 621-0390

National Technical Information Service (NTIS)
5285 Port Royal Road
Springfield, VA 22161-2171
(703) 487-4650

Abstract

An evaluation was made of the effects of integrating the required aircraft components with hypersonic high-lift configurations known as waveriders to create hypersonic cruise vehicles. Previous studies suggest that waveriders offer advantages in aerodynamic performance and propulsion/airframe integration (PAI) characteristics over conventional non-waverider hypersonic shapes. A wind-tunnel model was developed that integrates vehicle components, including canopies, engine components, and control surfaces, with two pure waverider shapes, both conical-flow-derived waveriders for a design Mach number of 4.0. Experimental data and limited computational fluid dynamics (CFD) solutions were obtained over a Mach number range of 1.6 to 4.63. The experimental data show the component build-up effects and the aerodynamic characteristics of the fully integrated configurations, including control surface effectiveness. The aerodynamic performance of the fully integrated configurations is not comparable to that of the pure waverider shapes, but is comparable to previously tested hypersonic vehicle models. Both configurations exhibit good lateral-directional stability characteristics.

1. Introduction

A waverider is any shape designed such that the bow shock generated by the shape is perfectly attached along the outer leading edge at the design flight condition. The waverider design method leads to several potential advantages over conventional non-waverider hypersonic concepts. The attached leading-edge shock wave confines the high-pressure region to the lower surface and results in high lift-drag ratios. Several design predictions suggest that waveriders may offer an aerodynamic performance advantage in terms of higher lift-drag ratios over non-waverider hypersonic concepts (refs. 1 and 2). In addition, the flow field below the waverider bottom surface is uniform and, in the case of waveriders derived from axisymmetric flow fields, there is little or no cross-flow in this region, making these shapes attractive candidates for engine integration. These advantages have led to interest in using waverider shapes for the forebody geometries of hypersonic airbreathing engine-integrated airframes. Waveriders have been considered for various types of missions including hypersonic cruise vehicles, single-stage-to-orbit vehicles, airbreathing hypersonic missiles, and various space-based applications (ref. 3).

The purpose of the current study is to examine the aerodynamic characteristics of two waverider-derived hypersonic cruise vehicles. No experimental data currently exist that address the integration of realistic vehicle components with waverider shapes. Therefore, the objectives of this study were threefold. The first was to create an experimental and computational database for waverider-derived configurations. The second was to examine the effects of individual vehicle components on pure waverider performance and to determine the differences in aerodynamic characteristics that result from integrating all vehicle components. The final objective was to evaluate the controllability of each of the fully integrated vehicles and the effectiveness of the control-surface design. These objectives were accomplished using results from wind-tunnel testing and a limited number of computational fluid dynamics (CFD) solutions. The CFD predictions were obtained for the pure waverider shapes only and provide comparisons with experimental data and design-code predictions. Two wind-tunnel models were designed that integrate canopies, engine packages, and control surfaces with two Mach 4.0 pure waverider shapes. The models were tested in the Langley Unitary Plan Wind Tunnel (UPWT) at NASA Langley Research Center.

This report describes the waverider aerodynamic design code used and discusses the method used in the development of the wind-tunnel models. The details of the experimental study are then presented as well as the computational method used to obtain the CFD predictions. The results are analyzed in three sections. First, the results of the pure waverider shapes without integrated vehicle components are presented. These results include flow-field characteristics from CFD solutions and experimental flow-visualization data as well as aerodynamic characteristics from the experiment and CFD predictions. Second, the experimental results of adding aircraft components to the pure waverider shapes are presented. The effects of the canopy, engine components, and control surface additions on aerodynamic performance and stability are examined. Finally, the aerodynamic characteristics of the fully integrated waverider-derived configurations are examined and compared with those of the pure waverider shapes. Control-surface effectiveness is also addressed in this section.

2. Symbols

B.L.	buttline of model (distance from centerline in spanwise direction), in.
C_D	drag coefficient
C_l	rolling-moment coefficient
$C_{l\beta}$	rolling-moment derivative, $\frac{\partial C_l}{\partial \beta}$
C_L	lift coefficient
C_M	pitching-moment coefficient
C_n	yawing-moment coefficient
$C_{n\beta}$	yawing-moment derivative, $\frac{\partial C_n}{\partial \beta}$
$\bar{c}$	moment reference length, in.
L/D	lift-drag ratio, $\frac{C_L}{C_D}$
M	Mach number
M.S.	model station (distance from nose in streamwise direction), in.
P	pressure, lbf/ft^2
P_{ss}	roll rate, deg/sec
Re	Reynolds number
S_{ref}	planform area, ft^2
u	velocity component, ft/sec
V	total volume, ft^3; velocity, ft/sec
V_{eff}	volumetric efficiency, $\frac{V^{2/3}}{S_{\text{ref}}}$
W.L.	waterline of model (distance from zero reference in vertical direction), in.
$X_{\text{c.g.}}$	moment reference center location
X, Y, Z	Cartesian coordinates, in.
y^+	inner law variable
α	angle of attack, deg
β	sideslip angle, deg
δ_A	angle of aileron deflection (trailing edge down positive), deg
δ_E	angle of elevon deflection (trailing edge down positive), deg
$\Delta\zeta$	distance from solid boundary to first cell center, in.
μ	viscosity coefficient, lbf-sec/ft^2
ξ, η, ζ	computational coordinates
ρ	density, lbm/ft^3

Subscripts:

c	conditions at first cell center next to solid boundaries
c.g.	center-of-gravity location
∞	free-stream conditions

3. Configuration Design and Model Development

3.1. Waverider Design Method

A specific waverider shape is uniquely defined by free-stream conditions, the type of generating flow-field body, and a leading-edge definition (ref. 1). The shapes of the upper and lower surfaces of the configuration follow from these parameters. The free-stream conditions, including Mach number and Reynolds number or altitude, are selected based on mission criteria. The design method used in this study involves a specific design point. The generating flow-field body is used to define the shock shape upon which the leading edge of the waverider is constructed. Although any arbitrary body in supersonic or hypersonic flow can be used as a generating flow-field body, this study focuses specifically on the class of conical-flow-derived waveriders, in which the generating flow-field body is a right circular cone in supersonic or hypersonic flow. At the outset of this research effort, this option was the best available for the application of interest. Other possible generating flow fields include osculating cone flow fields (ref. 4), hybrid cone-wedge generated flow fields (ref. 5), and inclined circular and elliptic conical flow fields (ref. 6). The length of the generating cone, length of the waverider, and semiapex angle of the cone are specified by the designer. The selection of these parameters can significantly affect the shape of the waverider generated as well as the aerodynamic performance of the configuration. Figure 1 illustrates the design of a conical-flow-derived waverider. The planform shape, or leading edge, is defined on the shock wave produced by the cone. The lower surface of the configuration is defined by tracing streamlines from the leading edge to the base of the cone. The result is that the lower compression surface is a stream surface behind the conical shock wave. The configurations studied here have an upper surface that is designed as a constant free-stream pressure surface. However, other techniques may be used, such as shaping the upper surface as an expansion or compression surface. The conical flow field, defined behind the shock wave, exists only below the lower surface of the waverider.

The resulting configuration offers two possible advantages over non-waverider hypersonic configurations. The first is a potential aerodynamic performance advantage (refs. 1, 2, and 7). Theoretically, the shock wave is perfectly attached along the outer leading edge at the design Mach number. The result is that the high-pressure region behind the shock wave is confined to the lower surface, and no flow spillage from the lower surface to the upper surface occurs. The maximum lift-drag ratios this method produces promise to exceed those of existing hypersonic configurations. Figure 2, taken from reference 2, shows the traditional "*L/D* barrier" in the supersonic/hypersonic regime for conventional vehicles. This correlation is empirical, based on actual flight vehicle experience at subsonic and low supersonic speeds and extrapolated to hypersonic Mach numbers (ref. 7). The symbols in figure 2 represent predictions for a variety of conical-flow-derived waverider shapes generated using the current method, which is described in detail in reference 2. The waverider shapes represented here are only the forward portions of possible hypersonic configurations and therefore are not realistic vehicles. The predictions shown assume that the configuration has zero base drag in order to remove the effect of the blunt base, which will be eliminated in a fully integrated vehicle, and show only the performance of the forward portion of such a vehicle. In other words, the predictions assume that free-stream static pressure acts at the base, making a direct comparison of the lift-drag ratios for waveriders and those of existing supersonic/hypersonic configurations difficult. Furthermore, the waveriders represented here do not have levels of volumetric efficiency comparable to those of the vehicles used in the *L/D* barrier calculation and may not have been obtained at similar flight-scaled Reynolds numbers. Although the lift-drag ratios of a fully integrated waverider configuration with the blunt base closed would likely be lower than those for the pure waverider shape, these predictions suggest that waveriders may offer an aerodynamic performance advantage over non-waverider vehicle concepts. Another advantage of axisymmetric waverider flow fields is that the lower surface flow field is uniform, and there is pure conical flow in this region for a perfectly attached shock wave. Therefore, a known uniform flow field can be delivered to scramjet engine modules on the lower surface, providing a benefit in propulsion/airframe integration (PAI) (ref. 8). The osculating cone and cone-wedge concepts mentioned previously may provide an even greater benefit over conical-flow-derived waveriders (refs. 4 and 5). The aerodynamic performance and PAI benefits suggested in previous research efforts have generated interest in using waveriders for various hypersonic vehicle designs.

The design code used in this study is the (University of) Maryland Axisymmetric Waverider Program (MAXWARP) (refs. 1, 2, and 9). The MAXWARP code is an inviscid design method that includes an estimate for skin friction in the design process. Various volumetric constraints may also be imposed by the user in order to produce waveriders with desirable structural characteristics and component packaging. These constraints include aspect ratio, slenderness ratio, and total volume. For the case of conical-flow-derived waveriders, the Taylor-Maccoll equation, which describes the flow field behind a conical shock wave (ref. 10), is integrated using a fourth-order Runge-Kutta method to compute the inviscid conical flow field behind the shock wave. The cone semiapex angle and length of the flow-field generating body are specified by the user along with free-stream conditions. The code starts with an initial leading-edge definition on the conical shock wave and creates a waverider shape from this initial leading edge. The pressure distributions on the surface of the configuration are integrated to calculate lift and drag coefficients. An estimate for skin friction is also included so that force coefficient predictions include both inviscid and viscous effects. This estimate is based on the reference temperature method, which is described in reference 11. The effect is to generate shapes for which wetted surface area is minimized to reduce skin friction drag. The code uses a simplex optimization routine (ref. 1) to optimize waveriders for a given figure of merit: maximum lift-drag ratio or minimum drag. More recent versions of the code allow the user to construct various other objective functions. At each iteration in the optimization process, an updated leading-edge definition is used to generate a new waverider shape that progresses toward the desired figure of merit. This process continues over a number of iterations until the optimum shape is found without violation of any of the user-specified volumetric constraints.

3.2. Waverider Shape Description

The pure waverider shapes used in this study, which define the forward portions of the waverider-derived vehicles, were designed using the MAXWARP design code. Free-stream conditions and optimization parameters were chosen based on the applicability of this study to a hypersonic cruise vehicle, with available ground-based test facility limitations taken into account. The design free-stream Mach number was 4.0 and the design Reynolds number was 2.0×10^6 per foot. Although the specific cruise Mach number for this type of vehicle would be higher, Mach 4.0 was selected as the design point based on the limitations of the UPWT and the range of data desired. The Mach number range of this

facility is 1.47 to 4.63. A design point of Mach 4.0 would permit the validation of the waverider concept at the design Mach number and also allow for the determination of aerodynamic characteristics at off-design Mach numbers. The use of endothermic fuels on this vehicle class is expected to drive the selection of cruise Mach number to approximately 5.0 to 5.5. No significant differences in the flow physics are expected between the ultimate design Mach number and the Mach number range investigated in this study. The Reynolds number chosen is based on nominal facility operating conditions in the UPWT and is not representative of a flight cruise altitude. The configuration was optimized for maximum lift-drag ratio at the design point because this quantity is more appropriate than minimum drag as a hypersonic cruise performance parameter.

A fully turbulent boundary layer and a wall temperature of 585°R were specified in the design. This wall temperature was selected based on previous experimental data from models tested in the UPWT. It is not likely that fully laminar conditions could be maintained in experimental testing at the conditions of interest, and transition is difficult to predict. Fully turbulent conditions can be achieved and maintained by the application of boundary-layer transition grit to the model surface.

Two different pure waverider shapes were developed for this study. The first is referred to as the "straight-wing" shape and was designed using the MAXWARP optimization routine. The second, referred to as the "cranked-wing" shape, was created by adjusting the leading edge of the straight-wing waverider to create a curved wingtip shape that had increased aspect ratio but still maintained shock attachment along the outer leading edge at the design free-stream condition. The term "cranked" in this context refers to a wing shape in which the sweep angle not only changes but also exhibits a large outboard dihedral angle in the plane of the base. The cranked-wing shape was designed to provide improvements in subsonic aerodynamic performance (because of increased aspect ratio) and in lateral-directional stability (because of dihedral effect) while maintaining high performance in the supersonic/hypersonic regime.

Three primary design criteria were used to select the best waverider shape designs for this application. First, the maximum lift-drag ratio was chosen to be as high as possible while not violating other design guidelines. This criterion drives the selection of the cone semiapex angle for the generating flow field. A value of 8.1° was selected for this application. Second, the volumetric efficiency ($V^{2/3}/S_{ref}$) was chosen to be as high as possible. An inverse relationship exists between the volumetric efficiency and the maximum lift-drag ratio for a given set of free-stream conditions. Therefore, an attempt was made to increase the volumetric efficiency as much as possible while accepting a minimum penalty in maximum lift-drag ratio. Finally, a configuration with a flat or slightly convex bottom surface in the cross section was desired for ease in propulsion systems integration. In addition to these three primary design guidelines, a configuration free of substantial curvature over most of the cross section was also desired to provide for the inclusion of an internal spar in an actual aircraft. Furthermore, the target value of span-to-length ratio was 0.8. Information from previous studies shows that larger span (higher aspect ratios) waveriders provide higher lift-drag ratios but are more difficult to integrate as a full waverider-based vehicle (ref. 12).

A three-view drawing and an oblique view of the straight-wing pure theoretical waverider shape generated by the design code are shown in figure 3. Table 1 summarizes the characteristics of this shape. The span-to-length ratio is 0.83. The lower surface of the straight-wing configuration has a slight convex curvature that facilitates integration of the propulsion system. The length selected for the waverider configuration was 24.0 in. based on the size of the test section in the UPWT. The length of the generating cone was selected to fix the location of the waverider leading edge on the conical shock wave to achieve the design criteria noted previously (48.0 in. for this application). A selection of different locations on the conical shock wave would result in waveriders with much different geometric characteristics and may result in the generation of unrealistic shapes that could not be integrated into vehicles. The volumetric efficiency, V_{eff}, of this configuration is 0.11 with a predicted maximum lift-drag ratio of 6.9.

A three-view drawing and an oblique view of the cranked-wing pure theoretical waverider shape generated by the design code are shown in figure 4. The cranked leading edge still lies on the same conical shock wave produced by the generating cone used to design the straight-wing waverider. The characteristics of the cranked-wing waverider shape are summarized in table 2. The span-to-length ratio is 0.96, which represents an approximately 16 percent increase in aspect ratio. This increase in aspect ratio should improve the subsonic aerodynamic performance over the straight-wing waverider while maintaining the structural characteristics of the straight-wing waverider near the centerline of the configuration. The volumetric efficiency of this configuration is 0.108 with a calculated maximum lift-drag ratio of 6.7. This configuration represents only a slight decrease of both parameters from the straight-wing waverider. The slight convex curvature of the bottom surface is maintained toward the centerline of the model. The dihedral angle of the aft cranked section is

approximately 28° when measured from the centerline of this section.

The values for maximum lift-drag ratio given are for the pure waverider shapes only. The waveriders were subsequently altered to close the blunt base and add control surfaces. The predictions assume that free-stream static pressure are acting at the base of the unaltered pure waverider shape, so that only forebody drag values are included in the performance predictions. As will be shown later, the incorporation of aftbody closure is a significant issue in hypersonic vehicle development.

3.3. Wind-Tunnel Model Designs

Two slight modifications to the design-code shapes were implemented in the wind-tunnel model design in order to accommodate model support hardware and additional vehicle components. A smooth ogive-cylindrical fairing was blended on to the upper surface of the pure waverider shapes to accommodate the sting and balance necessary to measure the aerodynamic loads on the model during testing. This volume was added to the upper surface rather than the lower surface because previous research indicates that modifications to the lower surface have an affect on the PAI characteristics of the waverider (ref. 13). Figures 5 and 6 show tunnel installation photographs of the straight-wing and cranked-wing pure waverider models with the upper surface fairing. The lower surface of the theoretical waverider shape was modified slightly by creating an inboard expansion surface with an angle of approximately 10°, beginning approximately 22 in. aft of the nose of the configuration and measuring approximately 3.5 in. in the spanwise direction. The lower surfaces follow the waverider theoretical stream surface up to this point. This modification was made in order to facilitate the integration of engine components and to reduce the closure angle necessary for control surfaces. Figure 7 shows a photograph of the lower surface of the cranked-wing waverider with the expansion on the aft end of this surface.

A realistic canopy was designed for the waverider-based configuration. The canopy was provided with faceted surfaces to resemble the canopy for a hypersonic vehicle. The aft portion of the canopy was designed to blend with the cylindrical fairing on the upper surface discussed previously. Figures 5 and 6 show the pure waverider models with the ogive-cylindrical fairing attached (i.e., canopy-off configuration). Figures 8 and 9 show the model with the faceted canopy attached.

The engine package for this configuration included a compression ramp, a non-flow-through engine module with side walls, and a nozzle/expansion ramp. The engine-package-on configuration provided an indication of the effect of modifying the theoretical waverider lower surface to integrate some type of engine system and is not intended to be a realistic propulsion simulation. The inlet capture area, expansion ramp turning angle, and nozzle exit area were designed for full-scale Mach 4.0 conditions. The compression surface shown in figure 8 is required for additional precompression of the flow entering the inlet. The non-flow-through configuration attempts to model the external cowl drag present on a realistic flow-through nacelle, but does not have the associated internal drag. Two different nozzle/expansion ramps were designed for the model. The first was used with the pure waverider configurations with the nacelle attached and the second was used with configurations that had control surfaces attached. These nozzles are referred to as the "short" and "long" nozzles, respectively (figs. 10(a) and 10(b)). Identical nozzles with static pressure taps were also fabricated in order to obtain surface pressure measurements on the nozzle. The non-instrumented ramps were used for force and moment runs.

Control surfaces were provided to examine their effects on waverider aerodynamic performance as well as the effectiveness of the control concept. The control surfaces were sized based on control-volume trends from supersonic fighter aircraft to extend and close the blunt base of the configurations. Elevon deflections of 0°, positive 20° (trailing edge down), and negative 20° (trailing edge up) were incorporated. A set of outboard ailerons having the same three deflection angles was designed for the straight wing. Because of the curved surface of the cranked wing and the small thickness of the outboard leading edge, the set of ailerons for the cranked-wing configuration consisted of an inboard aileron, which remained fixed at 0°, and a set of outboard ailerons, which were deflected at 0° and ±20°. A vertical tail surface was also designed in order to augment directional stability. Figures 8 and 9 show photographs of the model components with the various control surfaces. Figure 11 shows three-view drawings of the elevons, straight-wing ailerons, cranked-wing inboard ailerons, and cranked-wing outboard ailerons. This figure indicates the pertinent dimensions and shows the hinge-line locations for each control surface.

The model design allowed for testing of the straight-wing and cranked-wing pure waverider models, which are defined as configurations with no engine components or control surfaces. A configuration build up of the waverider models with different vehicle components could also be tested up to and including the fully integrated waverider-derived configurations, which are defined as configurations with engine components, control surfaces, and the canopy. Table 3 shows the pertinent model geometry for each configuration tested. Figure 12

shows a three-view drawing of the fully integrated configurations.

4. Experimental Method

The facility used in this study was the UPWT at NASA Langley Research Center. The UPWT is a closed-circuit, continuous-flow pressure tunnel with two 4- by 4- by 7-ft test sections, which were both used in this study. The Mach number range of the facility is 1.47 to 4.63, with a range in the low Mach number test section of 1.47 to 2.86 and a range in the high Mach number test section from 2.30 to 4.63. Continuous variation of Mach number is achieved by using asymmetric sliding block nozzles to vary the nozzle throat-to-test-section area ratio. The Reynolds number range of this facility is 0.5×10^6 to 8.0×10^6 per foot. However, the nominal Reynolds number for most tests is 2.0×10^6 per foot. A detailed description of the UPWT can be found in reference 14.

The configurations tested ranged from the straight and cranked pure waverider models to the fully integrated waverider-derived vehicles. The test configurations were chosen to show pure waverider performance; to isolate the effects on waverider aerodynamic performance of the canopy, engine package, and control surfaces; and to show the aerodynamic performance and stability characteristics of the fully integrated configurations. Only the cranked-wing configurations were tested in the low Mach number test section. The data were corrected for flow angularity in the test sections. Calibration data for the UPWT shows that the flow in both test sections has an upflow angle generally within 0.5° of the tunnel centerline (ref. 14). In each run, either six-component force and moment data, nozzle pressure data, or vapor-screen photographs were obtained. Schlieren photographs were taken during the force and moment runs.

The test conditions were chosen to investigate the aerodynamic performance and stability of each configuration at both the design Mach number and at off-design Mach numbers. Data were obtained at Mach numbers of 2.3, 4.0, and 4.63 for all configurations studied and, additionally, at Mach numbers of 3.5 and 4.2 for some configurations. Data for the cranked-wing configurations were also obtained at Mach numbers of 1.6, 1.8, and 2.0. The free-stream Reynolds number for most runs was 2.0×10^6 per foot. Some runs were made at Reynolds numbers of 1.5×10^6 per foot and 3.0×10^6 per foot in order to investigate the effects at off-design Reynolds numbers. The angle-of-attack range studied was −6° to 10° at fixed sideslip angles of 0° and 3°. Data were obtained over a sideslip angle range of −5° to 5° for the first configuration run in each test section in order to verify that yawing and rolling moment values are linear over this range (ref. 15). Based on these results, stability derivatives were calculated from data obtained at the two fixed sideslip angles.

The data obtained from the wind-tunnel tests include six-component force and moment data, static pressure readings on the blunt base of the model, static pressure data on the nozzle surfaces, and flow-visualization data. The balance used in this case was the NASA-LaRC-designated UT-50-B balance, which is a six-component strain gauge balance. Unless otherwise noted, the moment reference center for all configurations was located 16.623 in. aft of the nose. A total of 11 5-psi pressure transducers were used to measure the static pressure along the blunt base of the configurations and in the cavity surrounding the sting. Integrated areas were assigned to each tap or averaged group of taps and used to calculate the base axial force. All of the force data presented is corrected to assume free-stream static pressure acting at the base. This procedure is carried out so that the data may be presented showing only the upper and lower surface lift and drag values and eliminating the effect of the blunt base. This procedure is necessary because the base will be eliminated in any realistic waverider-derived configuration. The method of assuming free-stream pressure at the base is consistent with the design-code method and with previous studies showing predictions for waverider aerodynamic performance (refs. 2, 9, and 16). Details on the procedure used are included in reference 15. For configurations with both engines and control surfaces, only two base and two chamber pressures were measured. A 32-port, 5-psi external electronically scanned pressure (ESP) module was used to measure the static pressure on the nozzle surface for four runs. Figure 10 shows the locations of pressure taps on the nozzle surfaces for the short and long nozzles. Recall that the short nozzle is used with configurations having no control surfaces and the long nozzle is used with configurations with control surfaces. A total of 12 pressure taps were located on the short nozzle and 24 pressure taps were located on the long nozzle. The data are used to correct the nozzle surface pressures to assume free-stream static pressure acting on these surfaces for some configurations.

Schlieren and laser-vapor-screen photographs were taken in order to examine flow-field features including the shock attachment characteristics for various configurations. For the vapor-screen runs, the laser was positioned outside of the test section window and the light sheet was projected across the model surface in the spanwise direction, illuminating one cross section at a time. The camera was mounted inside of the test section above and behind the model. This setup gives a

cross-sectional view of the waverider flow field in the vapor-screen photographs.

The accuracy of the UT-50-B balance, based on a May 1993 calibration, is 0.5 percent of full scale for each component to within 95-percent confidence. The full-scale load limits were 600 lbf normal, 40 lbf axial, 1500 in-lbf pitching moment, 400 in-lbf rolling moment, 800 in-lbf yawing moment, and 300 lbf side force. As an example, using the method of root-mean-squares summation to combine independent error sources, these limits correspond to a range of uncertainty in lift coefficient of 0.0053 at $\alpha = 0°$ to 0.0054 at $\alpha = 10°$ and an uncertainty range in drag coefficient of 0.00036 at $\alpha = 0°$ to 0.001 at $\alpha = 10°$ for the $M_\infty = 4.0$ and $Re_\infty = 2.0 \times 10^6$ per foot condition. The repeatability of measurements was observed to be better than these uncertainties. Therefore, differences less than the indicated ranges for comparisons with data from different configurations in the same test, could be considered significant. However, comparisons between independent measurements are only good to within the quoted uncertainty ranges. Transition grit (no. 60 size sand grit in the low Mach number tests section and no. 30 size grit in the high Mach number test section) was applied in a 0.1-in-wide strip to the model upper and lower surfaces along the outboard leading edge at a location approximately 0.4 in. from the leading edge in the streamwise direction. These procedures were established for models tested in the UPWT based on unpublished transition experiments conducted in the UPWT and the methods of references 17 to 19.

5. Computational Method

Computational grids were developed for each of the pure waverider configurations by first developing a numerical surface description and then creating 3-D volume grids. Numerical surface descriptions of the straight-wing and cranked-wing wind-tunnel models were obtained from computer-aided design (CAD) descriptions of the model parts. Three-dimensional volume grids were created for each configuration using the GRIDGEN software package, which uses algebraic transfinite interpolation methods with elliptic interior point refinement (ref. 20). Only the pure waverider shapes with no integrated vehicle components were modeled for the CFD analysis.

The computational grids for each of the two pure waverider shapes model only half of the configuration because each is symmetric about the centerline. The grid orientation is shown in figure 13. The ξ-computational direction runs from the nose of the configuration to the base in the streamwise direction. The η-computational direction begins at the upper centerline and wraps around the leading edge, ending at the lower centerline. The ζ-computational direction runs from the surface of the configuration to the outer boundary. The grids for each of the two pure waverider shapes contained 91 points in the ξ direction, 111 points in the η direction, and 91 points in the ζ direction. Blunt leading edges were modeled for each configuration in order to provide a better comparison with experimental data. Grid points were also clustered near the surface of each configuration in order to adequately resolve the boundary-layer flow. The amount of grid spacing needed is judged by examining the grid spacing parameter, y^+, which is given by

$$y^+ = \sqrt{\frac{\rho_c u_c \Delta\zeta}{\mu_c}} \qquad (1)$$

where ρ_c, u_c, and μ_c are the density, velocity, and viscosity at the first cell center next to the solid surface and $\Delta\zeta$ is the distance from the first cell center to the body surface. Previous research has shown that y^+ values on the order of 1 provide accurate solutions (ref. 21).

The CFD solutions were obtained using the General Aerodynamic Simulation Program (GASP), version 2.2 (refs. 22 and 23). GASP is a finite volume code capable of solving the full Reynolds-averaged Navier-Stokes (RANS) equations as well as subsets of these equations, including the parabolized Navier-Stokes (PNS), thin-layer Navier-Stokes (TLNS), and Euler equations. Time integration in GASP is based on the integration of primitive variables, and convergence to a steady-state solution is obtained by iterating in pseudotime until the L2 norm of the residual vector has been reduced by a sufficient amount. GASP also contains several flux-split algorithms and limiters to accelerate convergence to steady state. Mesh sequencing is available as a means to accelerate convergence.

In this study, each configuration was modeled as a two-zone problem, as illustrated in figure 13. The first zone includes the blunt nose of the configuration. The flow in this region is a combination of subsonic and supersonic flow because a small area of subsonic flow exists behind the detached bow shock. Therefore, the TLNS equations are solved over the first zone using a global iteration procedure. The second zone encompasses the remainder of the configuration, extending from the zonal boundary to the base of the configuration. The flow in this region is computed by solving the PNS equations. These equations are valid for regions of predominately supersonic flow with no streamwise separation. A no-slip boundary condition is applied to all solid boundaries with a fixed wall temperature of 585°R, which is identical to that specified in the MAXWARP optimization routine when designing the waverider shapes. Free-stream conditions are applied at the outer boundary, second-order extrapolation from interior cells

is applied at the last streamwise plane, and symmetry boundary conditions are applied at the center plane. The Baldwin-Lomax algebraic turbulence model was used in these solutions to model turbulent boundary layers, and convergence to a steady state was obtained by reducing the L2 norm of the residual vector by 5 orders of magnitude.

In order to make appropriate comparisons, the conditions at which solutions were obtained were chosen based on conditions at which experimental data were available. Solutions were obtained at Mach 4.0 at angles of attack of −6°, 0°, 2°, 4°, and 8° for the straight-wing model. Solutions were obtained at Mach 4.0 at angles of attack of −6°, 0°, and 8° for the cranked-wing model. Solutions were also obtained at off-design Mach numbers of 2.3 and 4.63 at 0° angle of attack for each configuration.

6. Flow-Field and Aerodynamic Characteristics of Pure Waverider Models

6.1. Flow-Field Characteristics

The flow-field characteristics of the pure waverider models at the design Mach number can be illustrated by examining computational solutions of each configuration and laser vapor-screen photographs from wind-tunnel tests. Figure 14 shows a laser vapor-screen photograph of the flow at the base of the pure straight-wing waverider model and nondimensional static pressure contours at the base of the same configuration from a CFD solution at Mach 4.0, 0° angle of attack, and free-stream Reynolds number of 2.0×10^6 per foot. The model lower surface is highlighted in the photograph by the laser light sheet on the surface. The bow shock is indicated by the contrast between light and dark regions below the light sheet. On the left-hand side of the photograph, the shock is observed to be very near the edge of the lower surface. Thus, the vapor-screen photograph confirms the qualitative shock location predicted by the CFD solution. A small detachment distance exists even at the design point caused by blunt leading edge and boundary-layer displacement effects. These effects are not accounted for in the design code. The CFD predictions also indicate that the high-pressure region remains mostly confined below the model lower surface. A large low-pressure region (P/P_∞ of 0.95 or less) exists near the centerline of the model below the bottom surface because of the bottom surface expansion present on the model. However, the remainder of the bottom surface flow field is a smooth, conical flow field, so the presence of this slight expansion surface does not degrade the favorable PAI characteristics offered by the waverider. Engine modules would be placed upstream of the point where the expansion surface begins, so the flow entering the inlet would be highly compressed. Similar data are shown in figure 15 for the cranked-wing pure waverider model. The shock can be seen in the right-hand side of the photograph to be very near the outer leading edge of the model. The lower surface is again highlighted by the laser light. The full cross-sectional view is not shown because of the poor quality of the photographs. The experimental data confirm the qualitative shock location at the outer leading edge, which is predicted by the CFD solution for this case as well. Figure 16 further illustrates that the shock is slightly detached at the outer leading edge for both models. This figure shows a close-up view of the outer leading edge at the base of the cranked-wing and straight-wing waverider shapes from CFD solutions at Mach 4.0 and 0° angle of attack. Both of the views in figure 16 are to the same length scale, and nondimensional static pressure contours are shown in each view.

The flow-field characteristics of each pure waverider shape at off-design Mach numbers can also be illustrated by examining experimental flow-visualization data and CFD solutions. Figure 17 shows a comparison of a vapor-screen photograph and a CFD solution for the cranked-wing shape at Mach 2.3 and 0° angle of attack. The free-stream Reynolds number is 2.0×10^6 per foot. The data shown in this figure and orientation of the camera in the test section are the same as in figures 14 and 15. At Mach numbers below the design Mach number of 4.0, the shock-wave angle is larger and the detachment distance should be much larger than at the design Mach number. This outcome is predicted by the CFD solution and confirmed by the experimental data. Figure 18 shows similar views of the same configuration at Mach 4.63. The photograph in this figure was taken with the laser light sheet approximately 5 in. upstream of the base because the quality of the photograph taken with the light sheet at the base was poor. At Mach numbers greater than the design Mach number, the shock moves closer to the leading edge than at the design condition, as illustrated in both the vapor-screen photograph and predicted by the CFD solution. A large high-pressure region still exists in the bottom-surface flow field of this configuration at Mach 4.63. The qualitative shock locations can be further illustrated by examining planform schlieren photographs of the cranked-wing model. Figure 19 shows schlieren photographs of the cranked-wing pure waverider model in a planform view at Mach 2.3 (top), Mach 4.0 (middle), and Mach 4.63 (bottom). The right side of the figure shows a close-up view near the leading edge at each Mach number. The schlieren images in this figure have been enhanced by computer imaging techniques in order to show the shock structure more clearly. At Mach 2.3, the schlieren photograph shows that the

shock is detached from the leading edge. The outermost shock in the top view represents the bow shock. At Mach 4.0, the shock is much closer to the outer leading edge, but a small detachment distance still exists. At Mach 4.63, the photograph does not show the presence of a shock wave near the leading edge, possibly because the shock is attached at this condition.

6.2. Aerodynamic Performance

The aerodynamic performance characteristics of the two pure waverider models are examined here using experimental force and moment data and computational predictions. Off-design Mach number and Reynolds number effects are evaluated using experimental data. The longitudinal and lateral-directional stability characteristics are also examined for each configuration using experimental data. Unless otherwise indicated, all of the experimental and computational data presented have been corrected to a condition of free-stream pressure acting at the blunt bases of the configurations, as previously discussed.

The aerodynamic performance of the straight-wing and cranked-wing pure waverider shapes at the design Mach number is shown in figures 20 and 21. These figures show experimental data, CFD predictions, and design-code predictions for the lift, drag, and lift-drag ratios of each configuration at Mach 4.0 and a Reynolds number of 2.0×10^6 per foot. The computational values were obtained by integrating surface pressure and skin friction predictions from CFD solutions. Because the data are corrected to eliminate the base drag, these data should be interpreted as the performance of the forward portion (or forebody) of a possible hypersonic configuration and not that of a realistic hypersonic vehicle. In general, agreement is good between the experimental data and computational predictions. Both the computational predictions and experimental data show lower lift and higher drag values than the predicted design-code values, and these differences can be attributed to several causes. The flow-visualization data and CFD flow-field solutions showed that a slight detachment distance exists at the outer leading edge even at the design condition, which results in a lift loss and a drag decrease. However, the design code assumes an infinitely sharp leading edge with a perfectly attached shock wave. An additional lift loss results from the expansion ramp on the bottom surface of the waverider, and an increase in drag results from the additional volume added to the upper surface of the model. The experimental data also show that the maximum lift-drag ratio occurs near 2° angle of attack for each configuration. This finding is also consistent with previous studies, such as those in references 13 and 16, which show that the maximum lift-drag ratio occurs at an angle of attack greater than 0° for the waverider configurations studied in these references.

A direct comparison of the experimental aerodynamic performance of the two pure waverider models is shown in figure 22. The experimental data show that the cranked-wing shape has a slightly higher maximum lift-drag ratio than the straight-wing shape. At positive angles of attack, the straight-wing shape produced slightly higher lift coefficients. Aside from these observations, there are no significant differences between the two configurations.

The off-design performances of the straight-wing pure and cranked-wing pure waverider models are shown in figures 23 and 24, respectively. Each of these figures shows the experimental lift, drag, and lift-drag ratio at all Mach numbers studied as well as maximum lift-drag ratio versus Mach number. The data indicate that there is no significant performance degradation at off-design Mach numbers. Both configurations show higher maximum lift-drag ratios than the design point value at Mach numbers less than 4.0, using the assumption of free-stream pressure acting at the base. Similar results have been found in previous waverider studies (refs. 13, 16, and 24) and are also typical for non-waverider supersonic/hypersonic configurations. The cranked-wing waverider shape provides better aerodynamic performance at Mach numbers of 4.0 and below. At higher Mach numbers, there are no significant differences between the performance of the two configurations.

The effects of Reynolds number on aerodynamic performance of the straight-wing and cranked-wing configurations are shown in figures 25 and 26, respectively. No significant effects of Reynolds number variation were observed for either configuration in the range studied, except for a slight increase in maximum lift-drag ratio at the 3.0×10^6-per-foot condition for both configurations. This result is most likely because the skin friction coefficient decreases as Reynolds number increases, resulting in decreased drag and thus increased lift-drag ratios at higher Reynolds numbers. The decrease in drag observed experimentally is approximately equal to the decrease in viscous drag predicted by the reference temperature method (ref. 11). Computational solutions at Mach 4.0 and a Reynolds number of 2.0×10^6 per foot show that the viscous drag contribution is approximately 34 percent of total drag. By comparison, the MAXWARP design code predicts a viscous contribution of approximately 38 percent to the total drag.

The pitching-moment characteristics of the straight-wing and cranked-wing pure waverider configurations are shown in figure 27. This figure shows the pitching-moment coefficient versus angle of attack at each Mach number studied. Both configurations are longitudinally

unstable at all Mach numbers studied. The moment reference center location here is an arbitrarily selected location at the approximate location of the center of gravity of the fully integrated model. This moment reference center location (16.623 in. aft of the nose) is used for all configurations studied unless otherwise stated. The cranked-wing pitching moment curve is more nonlinear than that for the straight-wing shape, indicating that the shock may be detached at higher angles of attack for the cranked-wing configuration. The yawing moment characteristics are shown in figure 28. This figure shows the yawing moment derivative versus angle of attack at each Mach number studied for both configurations. The straight-wing configuration is directionally unstable at all Mach numbers studied at angles of attack of 8° and below. The cranked-wing configuration is directionally stable at all Mach numbers studied above an angle of attack of 4°. Both configurations experience a destabilizing effect as Mach number increases. The cranked-wing configuration was expected to provide improved directional stability from the increased dihedral along the outboard leading edge. The rolling moment characteristics are shown in figure 29 for each configuration. The cranked-wing waverider shows better lateral stability characteristics than the straight-wing model. The cranked-wing configuration exhibits positive effective dihedral above 0° angle of attack at all Mach numbers. The straight-wing model is unstable at angles of attack below 6.0° at Mach numbers of 4.0 and 4.63 and is unstable at angles of attack below 4° at a Mach number of 2.3.

7. Component Build-Up Effects

7.1. Effect of Canopy

The effects of adding the canopy on the aerodynamic performance of the pure straight-wing and cranked-wing waverider models are illustrated in figures 30 and 31, respectively. These data were obtained for configurations that have no control surfaces or engine components attached, and the data are corrected to assume free-stream static pressure acting at the base. Each figure shows the lift and drag coefficients as well as lift-drag ratios at Mach 4.0 and the maximum lift-drag ratio at each comparative Mach number studied for the canopy-off and faceted-canopy configurations. The canopy-off configurations have the ogive-cylindrical fairing on the upper surface, as discussed previously. Both the straight-wing and cranked-wing configurations show little difference in lift when the canopy is added. The canopy-on configurations show slightly higher drag than those with no canopy and an accompanying decrease in lift-drag ratios at positive values of lift over the Mach number range studied. The maximum lift-drag ratio at Mach 4.0 is reduced by 3.6 percent for the straight-wing configuration when the faceted canopy is used. Similarly, a 5.1-percent reduction in maximum lift-drag ratio occurs for the cranked-wing configuration. The data indicate that a penalty was incurred for the canopy, and therefore attention should be paid to the canopy design in a hypersonic waverider-based vehicle.

7.2. Effect of Engine Package

The engine component effects are evaluated by comparing experimental data from engine-on and engine-off configurations. Figures 32 and 33 show the effects of adding the engine package (ramp, inlet, and nozzle components) to the straight-wing and cranked-wing configurations, respectively. The data shown here are for configurations with the canopy and no control surfaces. The data are corrected to assume free-stream static pressure acting at the base. No correction is applied to these data for the nozzle surface pressures. Each figure shows lift and drag coefficients as well as lift-drag ratios at Mach 4.0 and the maximum lift-drag ratio at comparative Mach numbers for engine-on and engine-off configurations. The addition of engine components results in a slight increase in lift and a significant increase in drag at Mach 4.0. These effects are caused by the inlet compression surface and the increase in projected frontal area and produce a decrease in lift-drag ratio at positive values of lift and a reduction in maximum lift-drag ratio over the Mach number range studied. The straight-wing engine-on configuration shows a 19.7-percent reduction in the maximum lift-drag ratio at Mach 4.0 over the engine-off configuration. The cranked-wing model shows a 17.7-percent reduction at the same condition.

7.3. Effect of Control Surface Addition

The effects of adding undeflected control surfaces are illustrated by comparing data for configurations with no control surfaces to those with undeflected ailerons and elevons attached. Each configuration includes the canopy and engine components. Data for both the straight-wing and cranked-wing configurations are shown. The coefficient data are reduced by the planform areas of each corresponding configuration so the effects of increased planform are accounted for in the normalization of these data. The plots showing drag and lift-drag data include three separate data sets. The first is the data for the controls-off configuration corrected to assume free-stream pressure at the base. Therefore, only forebody drag values are included in these data and base drag is not included. The second data set is the controls-on data and the third set is the controls-off data with base drag included (i.e., uncorrected data from wind-tunnel measurements), so that these data include the effect of the blunt base. A comparison between the second and third data sets shows the aerodynamic effect of adding control

surfaces to the configuration, and a comparison between the first two data sets shows the relative performance between the closed configurations and that of the forebody surface only without the effect of the blunt base.

The effect of adding undeflected control surfaces to straight-wing waverider configuration with the canopy and engine components attached is summarized in figure 34. The addition of control surfaces causes a slight decrease in lift coefficient at Mach 4.0. This decrease is partially caused by the large expansion angle that is present on the elevon lower surfaces and a 16-percent increase in reference area for the controls-on configuration. A comparison of the controls-off data with base drag and the controls-on data shows a decrease in drag at a given lift-coefficient value. There is a slight increase in lift-drag ratios at low positive angles of attack and an increase in maximum lift-drag ratios when 0° control surfaces were added to the configuration. However, a comparison of the controls-on data with the controls-off data with no base drag shows that the closed configuration has significantly higher drag values and lower maximum lift-drag ratios than the forebody-only values. This result indicates that the inclusion of aftbody closure presents a significant challenge in the integration of pure waverider shapes into hypersonic vehicles and that this aspect of the configuration deserves special consideration in the design process. It is likely that the lift-drag ratios of a closed configuration cannot approach those of pure waverider shapes because the effect of base drag is often not included in lift-drag values for these configurations. The effects of control surface addition are similar for the cranked-wing configuration as indicated in figure 35. For reference, the base area is approximately 8.3 percent of the planform area for the straight-wing model with no control surfaces and approximately 9.1 percent for the cranked-wing model.

The control surface design for the configuration used in this study was a somewhat arbitrary design based only on trends from various supersonic fighter aircraft. A more optimum design could minimize the performance degradation caused by the closure of the blunt base. A performance improvement could be obtained by including the aftbody closure in the design/optimization process. Previous studies have examined the possibility of using blunt trailing edges on control surfaces as a means of enhancing the aerodynamic performance (refs. 25 to 27). The blunt base reduces the strength of the base recompression shock and proper design of the trailing edge can result in an increase in base pressure and a decrease in drag. A control surface design that takes advantage of these effects would enhance the aerodynamic performance of the configuration. This enhancement could be accomplished by reducing the thickness of the base by maintaining the lower surface as a waverider stream surface all the way to the base while designing the upper surface as an expansion surface. Longer control surfaces would also reduce the closure angle and enhance the pitch control power of the configuration.

8. Characteristics of Fully-Integrated Waverider-Derived Hypersonic Cruise Configurations

8.1. Aerodynamic Performance

Aerodynamic characteristics of each of the fully integrated waverider-derived configurations are examined over the Mach number range using experimental data, and the performance of these configurations are compared to that of the pure waverider shapes. The fully integrated configurations are defined here to have the canopy, the engine components, the undeflected ailerons, the undeflected elevons, and the vertical tail attached. The aerodynamic characteristics of the straight-wing and cranked-wing configurations are presented first followed by comparisons to the corresponding pure waverider configuration.

The aerodynamic performance of the straight-wing and cranked-wing waverider-derived hypersonic cruise configurations are shown in figures 36 and 37, respectively. The data presented here have the nozzle surface pressures corrected to assume free-stream pressure acting on the nozzle surface. The data are presented using this method to show the aerodynamic characteristics without any propulsive effect on the nozzle surface. The force data were corrected by assigning integration areas to each pressure tap measurement and computing the corrected coefficients. The locations of pressure taps are shown in figure 10. The straight-wing configuration has a maximum lift-drag ratio of 4.69 at Mach 4.0 and the cranked-wing configuration has a value of 4.56 when the nozzle surface pressures are corrected to free-stream pressure. The aerodynamic performance of each configuration does not vary significantly at off-design Mach numbers. The maximum lift-drag ratio for each configuration also occurs near 2° angle of attack at Mach 4.0. The angle of attack for maximum lift-drag ratio increases as Mach number decreases. At Mach numbers of 2.0 and below, the maximum lift-drag ratios for the cranked-wing configuration do not follow the general trend of increasing maximum lift-drag ratio with decreasing Mach number. This situation results from lift curve slope values that show similar inconsistencies at Mach numbers less than 2.3.

A direct comparison of the straight-wing and cranked-wing fully integrated vehicles is shown in figure 38. The straight-wing configuration produces slightly

higher values of maximum lift-drag ratio than the cranked-wing configuration at Mach numbers of 2.3 and higher. The straight-wing model also shows higher lift coefficient values at Mach 4.0. The straight-wing model shows a maximum lift-drag ratio that is 3.0 percent higher than that of the cranked-wing configuration at the design Mach number of 4.0.

Comparisons of the aerodynamics of the straight-wing pure waverider model and the fully integrated configuration are shown in figure 39. This figure shows lift and drag coefficients as well as lift-drag ratios at Mach 4.0 and the maximum lift-drag ratios at each Mach number studied. As in figures 34 and 35, these data sets are presented for comparison in the drag and lift-drag plots. The first data set represents the pure waverider shape with no base drag included. The second represents the waverider shape with base drag, and the third represents the fully integrated configuration. The nozzle surface pressures are corrected to assume free-stream pressure on the nozzle surface for the fully integrated vehicles. A comparison of the pure waverider data with base drag and the fully integrated data shows that the aerodynamic performance of the pure waverider shape is degraded when all of the various vehicle components are added. A reduction in lift coefficient for the fully integrated configuration is observed at Mach 4.0 above 0° angle of attack, which increases as angle of attack increases. An increase in drag is observed when all components are integrated with the pure waverider model. These effects result in a decrease in lift-drag ratios at Mach 4.0 and in maximum lift-drag ratios at comparative Mach numbers of 4.0 and above. At Mach 2.3, there is a slight increase in maximum lift-drag ratio when all vehicle components are added. This increase is most likely caused by the nozzle surface pressure correction to free-stream pressure. The free-stream static pressure increases as Mach number decreases. However, the aerodynamic performance of the fully integrated vehicle is significantly degraded from that of the pure waverider shape only with no base drag included, because of the drag produced by the control surface addition. The maximum lift-drag ratio at Mach 4.0 for the fully integrated vehicle is 4.69, compared to 6.68 for the pure waverider shape.

A comparison of the fully integrated cranked-wing configuration and the pure cranked-wing waverider model yields conclusions similar to those of the comparison of the straight-wing configurations. Figure 40 shows the aerodynamic performance of the cranked-wing waverider forebody and the cranked-wing fully integrated configuration. The addition of vehicle components causes a slight degradation in the aerodynamic performance, but the lift-drag ratios observed for the fully integrated model are significantly lower than those for the pure waverider shape only with no base drag. The maximum lift-drag ratio at Mach 4.0 for the fully integrated configuration is 4.56, compared to a value of 6.72 for the fully integrated vehicle.

From these results, it can be concluded that the maximum lift-drag ratios of a fully integrated waverider-derived configuration with aftbody closure likely cannot approach those of pure waverider shapes. Theoretical predictions for waverider configurations do not include the effects of aftbody closure. However, it will be shown that the fully integrated waverider-derived configurations studied here are comparable in aerodynamic performance to previously tested hypersonic models with performance improvements possible through enhanced control surface and propulsion system designs.

In order to characterize the lift-drag values of the configurations studied here, a comparison is made between data for the present cranked-wing fully integrated waverider-derived configuration and experimental data from six hypersonic vehicle wind-tunnel models previously tested in NASA Langley facilities (refs. 28 to 33) in figure 41. Although direct comparisons of these data are not possible here because of different conditions, geometries, levels of volumetric efficiencies, and force accounting methodologies, a range of values can be obtained to compare with the data from the current study. As shown in figure 41, the waverider falls within the same general range of lift-drag values as the non-waverider hypersonic configurations. The lift-drag ratios of the waverider configurations studied could be improved significantly through a better design of the propulsion system and control surface closure. Therefore, the waverider configurations studied here offer at least comparable aerodynamic performance and perhaps a modest advantage over conventional non-waverider hypersonic vehicles.

8.2. Longitudinal Control Effectiveness and Trim

Both fully integrated configurations are longitudinally unstable at each Mach number studied. The pitching-moment coefficient data as a function of angle of attack at each Mach number studied are shown in figure 42. Data for the straight-wing and cranked-wing fully integrated waverider-derived hypersonic cruise configurations are shown. The moment reference center is located at 62.5 percent of the centerline chord. At higher angles of attack, the cranked-wing configuration shows a destabilizing increase in the pitching moment curve. This increase indicates that the shock may have detached from the leading edge of the outer cranked portion of the wing at higher angles of attack. The longitudinal instability of these configurations may be addressed in one of two ways. First, it may be possible to shift the center-of-gravity location for a fully integrated flight vehicle to a

location that would provide at least neutral stability over the Mach number range. Recommendations for such locations are presented later in this section. Second, the addition of a fully functioning propulsion system would enhance the longitudinal instability by increasing the aft-body lower surface pressures.

The pitch control effectiveness of the elevons and elevon/aileron combination for the straight-wing configuration is shown in figure 43. Data are shown for three trim settings. The first is one with both the elevons and ailerons at 0°, the second with a positive 20° elevon deflection (δ_E) and a 0° aileron deflection (δ_A), and the third with both elevons and ailerons deflected at 20°. The effectiveness of the elevon decreases as Mach number increases, as evidenced by the smaller increments in lift and pitching-moment coefficients produced by each deflection. The ailerons were more effective than the elevons in pitch control because of the shadowing of the elevon behind the thick wing shape and the location of the elevon in an expansion flow field. The CFD flow field solutions showed that the bottom surface flow field expands to pressure below free-stream pressure in the region where the elevons are placed. Also, the closure angle for the elevon was severe because of the thick base of the waverider. Each aileron has only 70 percent of the planform area of the elevon but at higher angles of attack generates substantially more pitching moment. These characteristics may be unacceptable and indicate that the pitch control concept should be redesigned.

The pitch control effectiveness of the elevons for the cranked-wing configuration is shown in figure 44. Each figure shows data for 0°, 20°, and −20° elevon deflections with 0° ailerons. No runs were made with both ailerons and elevons deflected at the same angle because of the shape of the trailing edge for the cranked-wing configuration. The elevon pitch control power for this configuration also decreases as Mach number increases. However, in contrast to the straight-wing pitch control data, the cranked-wing pitching moment curves are nonlinear. This factor makes the elevon pitch control power even more critical for this configuration than for the straight-wing vehicle. These data indicate that the nose-down pitch control power of this configuration is not sufficient. Either symmetric ailerons must be used to provide additional pitch control power or the elevon area should be increased.

Because of the combination of unstable pitching moment characteristics and low pitch control power observed in the experimental data, the configurations should be balanced such that they are at least neutrally stable to ensure adequate pitch control power throughout the angle-of-attack range. For a realistic full-scale flight vehicle, it should be possible to control the center-of-gravity location through packaging. Also, it may be possible to control the shift in static margin from subsonic to supersonic speeds using fuel transfer. Neutral stability can be achieved by placing the center of gravity at a location equal to 58 percent of the centerline chord for the fully integrated straight-wing configuration and 59 percent of the centerline chord for the cranked-wing configuration. Data for lift and pitching-moment coefficients referenced to these center-of-gravity locations are shown in figure 45 for the straight-wing vehicle and in figure 46 for the cranked-wing vehicle. In figure 45, the data for the trailing-edge-up elevon deflections were extrapolated from the cranked-wing data and applied to the straight-wing configuration. Also note that all of the data presented here are for unpowered conditions. The addition of a functioning propulsion system will enhance the longitudinal stability of the vehicle even further. These data are presented only to indicate the effects of an alternative choice of center-of-gravity locations. Subsequent data are presented at the original moment reference center location of 62.5 percent of the centerline chord.

8.3. Lateral-Directional Stability and Control Effectiveness

The lateral-directional stability of the straight-wing and cranked-wing hypersonic cruise vehicles are shown in figures 47 and 48, respectively. Each figure shows yawing and rolling moment derivatives at each Mach number studied. Both configurations are directionally stable at all Mach numbers investigated, with the cranked-wing model providing higher stability levels than the straight-wing model. The cranked-wing fully integrated configuration is laterally stable across the angle-of-attack range at all Mach numbers studied. The straight-wing fully integrated configuration is laterally unstable at angles of attack below 6° (at Mach 4.0). This roll instability may be caused in part by the high placement of the balance in the model. No transfer distance in the vertical direction was applied to the moment reference center in the presentation of data.

Figures 49 and 50 show the effect of the vertical tail on yawing moment derivative and rolling moment derivative values for each configuration. The effect of the vertical tail is to significantly enhance the directional stability of both the straight-wing and cranked-wing configurations, indicated by the large positive shift in yawing moment derivatives when the vertical tail is added to each model. No rudder control effectiveness runs were made in this study, so it is not clear whether sufficient yaw control power exists to augment stability. The addition of the vertical tail does not cause any significant change in the lateral stability characteristics of either configuration.

The effectiveness of a 20° aileron deflection on the straight-wing configuration is shown in figure 51. A 20°

aileron deflection indicated here implies one aileron with a 20° trailing-edge-down deflection and the other with a 20° trailing-edge-up deflection. The elevons remained fixed at 0° for these runs. Figure 51 shows rolling moment and yawing moment increments between the deflected and nondeflected runs. Additionally, the DATCOM computer code was used to estimate the steady state roll rates for this configuration (ref. 34). Table 4 shows the steady roll rate capabilities as predicted by this method. The roll rate is shown as deg/sec of roll, normalized by flight velocity. For most vehicles of this type, excess roll-control power is available at lower angles of attack. The requirements for pitch and roll control surfaces for the waverider-derived vehicles may be driven by low-speed flying qualities. These qualities include roll-rate capabilities at subsonic speeds and crosswind landing requirements.

Figure 52 shows the effectiveness of the ailerons for the cranked-wing fully integrated configuration. However, a significant difference exists between these results and those for the straight-wing configuration. The cranked-wing ailerons produce considerably more adverse yaw at 0° angle of attack than the straight-wing configuration, as evidenced by the large negative values of ΔC_n. The adverse yaw produced by the cranked-wing ailerons will further drive the control power requirements of the rudder.

Figure 53 shows the aileron effectiveness on lateral-directional stability with the ailerons deflected at 20° for the cranked-wing fully integrated configuration. Rolling moment and yawing moment increments for a positive 20° elevon deflection and a ±20° aileron deflection are shown. A comparison of these data shows that a 20° elevon deflection has no effect on roll control power, indicating that interaction between controls is minimal at the Mach numbers studied here.

9. Concluding Remarks

The aerodynamic performance and stability and control characteristics of two Mach 4.0 waverider-derived hypersonic cruise configurations were examined. Experimental force, moment, and flow-visualization data were obtained for the two Mach 4.0 waverider configurations in both test sections of the Langley Unitary Plan Wind Tunnel (UPWT). The wind-tunnel models were designed to allow testing of various configurations ranging from pure waveriders to fully integrated vehicles. The two pure waverider shapes were referred to as the straight-wing pure and the cranked-wing pure waveriders. Experimental data as well as limited computational solutions were used to examine the flow field and aerodynamic characteristics of the two pure waverider shapes, the component build-up effects, and the aerodynamic and controllability characteristics of the fully integrated hypersonic cruise vehicles.

The flow-field characteristics and aerodynamic performance of the two pure waverider shapes were examined using experimental and computational data. Computational fluid dynamics (CFD) predictions and laser vapor-screen photographs of the straight-wing and cranked-wing pure waverider models confirmed the shock attachment/detachment characteristics of each configuration. The shock was slightly detached from the outer leading edge at the design Mach number of 4.0 and 0° angle of attack. This detachment distance exists because of boundary-layer displacement effects as well as blunt leading-edge effects. The design code assumes an infinitely sharp leading edge and does not account for the physical presence of a boundary layer. Comparisons between experimental force data and CFD predictions were generally good. The maximum lift-drag ratios observed experimentally were lower than the design-code predictions, as expected. These lower lift-drag ratios were caused by a loss of lift and an increase in drag caused by the shock not being perfectly attached as well as to loss of lift from the lower-surface expansion and an increase in drag from the additional volume added to the upper surface to accommodate model support hardware. The maximum lift-drag ratio for each configuration occurs at an angle of attack above 0°. Both the CFD predictions and experimental data showed that there were no significant performance degradations at off-design Mach numbers. The cranked-wing pure waverider model exhibited slightly better aerodynamic performance at the comparative Mach numbers studied than the straight-wing model.

Component build-up effects of waverider-derived vehicles were examined by comparing experimental force and moment data. The primary effect of individually adding the canopy and the engine package was to increase the drag of the configuration, thereby resulting in a degradation in aerodynamic performance. The aerodynamic effect of adding control surfaces was to increase the maximum lift-drag ratios slightly at each Mach number studied. However, the aerodynamic performance of the controls-on configurations was significantly degraded from that of the pure waverider shape only by the addition of aftbody closure and the associated drag production. The values presented for the pure waverider model show the performance of the waverider surface only and do not include base drag. These results indicate that additional consideration should be applied to the design of control surfaces and aftbody closure in waverider-based hypersonic cruise configurations. A control surface configuration with a less severe closure angle or controls with blunt trailing edges may result in improved performance. Inclusion of the aftbody closure

in the optimization process for the waverider shape may also improve the performance significantly.

The characteristics of the fully integrated waverider-derived hypersonic cruise vehicles were also examined by comparisons of experimental force and moment data. The aerodynamic performance of each fully integrated waverider model (straight-wing and cranked-wing configuration) was significantly degraded from that of the pure waverider shapes, because of the inclusion of aftbody closure in the fully integrated configuration. The straight-wing fully integrated configuration provided slightly better aerodynamic performance than the cranked-wing fully integrated model. The maximum lift-drag ratios at Mach 4.0 were 4.69 for the straight-wing model and 4.56 for the cranked-wing model. The waverider concept also provides a uniform compressed flow field to the inlet, which offers potential advantages for airbreathing propulsion systems integration. The use of different generating flow fields, such as osculating-cone and cone-wedge flow fields, may further improve these characteristics. Furthermore, the results of this study have identified areas where design improvements could enhance performance, such as control surfaces, aftbody closure, and propulsion system design.

Both fully integrated vehicles are longitudinally unstable across the Mach number range studied for unpowered conditions with the selected reference moment center. Additionally, locations were recommended for placement of the center of gravity in each configuration in order to ensure at least neutral stability across the Mach number range. The pitch-control effectiveness of the elevons was judged to be unacceptable for both configurations, and the data indicate that the pitch control concept should be redesigned. The ailerons were significantly more effective than the elevons for pitch control. The cranked-wing vehicle shows significantly better lateral-directional stability than the straight-wing vehicle. The straight-wing configuration was unstable at angles of attack below 6° at Mach 4.0. The vertical tail has a significant stabilizing effect on directional stability, but very little effect on lateral stability. The ailerons are also highly effective for the cranked-wing vehicle, but produce a significant amount of adverse yaw.

NASA Langley Research Center
Hampton, VA 23681-0001
May 6, 1996

References

1. Bowcutt, K. G.; Anderson, J. D.; and Capriotti, D.: Viscous Optimized Hypersonic Waveriders. AIAA-87-0272, Jan. 1987.

2. Corda, Stephen; and Anderson, John D., Jr.: Viscous Optimized Hypersonic Waveriders Designed From Axisymmetric Flow Fields. AIAA-88-0369, Jan. 1988.

3. Eggers, A. J., Jr.; Ashley, Holt; Springer, George S.; Bowles, Jeffrey V.; and Ardema, Mark D.: Hypersonic Waverider Configurations From the 1950's to the 1990's. *Proceedings of the 1st International Hypersonic Waverider Symposium*, John D. Anderson, Jr., Mark J. Lewis, Stephen Corda, and Isaiah M. Blankson, eds., Univ. of Maryland, 1990.

4. Sobieczky, H.; Dougherty, F. C.; and Jones, K.: Hypersonic Waverider Design From Given Shock Waves. *Proceedings of the 1st International Hypersonic Waverider Symposium*, John D. Anderson, Jr., Mark J. Lewis, Stephen Corda, and Isaiah M. Blankson, eds., Univ. of Maryland, 1990.

5. Takashima, Naruhisa; and Lewis, Mark J.: Waverider Configurations Based on Non-Axisymmetric Flow Fields for Engine-Airframe Integration. AIAA-94-0380, Jan. 1994.

6. Rasmussen, Maurice L.: Waverider Configurations Derived From Inclined Circular and Elliptic Cones. *J. Spacecr. & Rockets*, vol. 17, no. 6, Nov.–Dec. 1980, pp. 537–545.

7. Kuchemann, D.: *The Aerodynamic Design of Aircraft*. Pergamon Press, Inc., 1978.

8. O'Neill, Mary K. L.; and Lewis, Mark J.: Optimized Scramjet Integration on a Waverider. *J. Aircr.*, vol. 29, no. 6, Nov.–Dec. 1992, pp. 1114–1121.

9. Corda, Stephen; and Seifert, E. Scott: *User Information for Maryland Axisymmetric Wave Rider Program (MAXIWARP)*. Univ. of Maryland, Jan. 1989.

10. Anderson, John D., Jr.: *Modern Compressible Flow—With Historical Perspective*. McGraw-Hill, Inc., 1982.

11. Anderson, John D., Jr.: *Hypersonic and High Temperature Gas Dynamics*. McGraw-Hill, Inc., 1989.

12. Beuerlein, David L.: Optimization of Waveriders to Maximize Mission Performance. *Proceedings of the 1st International Hypersonic Waverider Symposium*, John D. Anderson, Jr., Mark J. Lewis, Stephen Corda, and Isaiah M. Blankson, eds., Univ. of Maryland, 1990.

13. Cockrell, Charles E., Jr.: Interpretation of Waverider Performance Data Using Computational Fluid Dynamics. AIAA-93-2921, July 1993.

14. Jackson, C. M., Jr.; Corlett, W. A.; and Monta, W. J.: *Description and Calibration of the Langley Unitary Plan Wind Tunnel*. NASA TP-1905, 1981.

15. Cockrell, Charles Edward, Jr.: *Vehicle Integration Effects on Hypersonic Waveriders*. NASA TM-109739, 1994.

16. Bauer, Steven X. S.; Covell, Peter F.; Forrest, Dana K.; and McGrath, Brian E.: Analysis of Two Viscous Optimized Waveriders. *Proceedings of the 1st International Hypersonic Waverider Symposium*, John D. Anderson, Jr., Mark J. Lewis, Stephen Corda, and Isaiah M. Blankson, eds., Univ. of Maryland, 1990.

17. Braslow, A. L.; and Knox, Eugene C.: *Simplified Method for Determination of Critical Height of Distributed Roughness Particles for Boundary-Layer Transition at Mach Numbers From 0 to 5.* NACA TN-4363, Sept. 1958.

18. Braslow, A. L.; Harris, R. V., Jr.; and Hicks, R. M.: *Use of Grit-Type Boundary-Layer-Transition Trips on Wind-Tunnel Models.* NASA TN D-3579, 1966.

19. Stallings, Robert L., Jr.; and Lamb, Milton: *Effects of Roughness Size on the Position of Boundary-Layer Transition and on the Aerodynamic Characteristics of a 55 Degree Swept Delta Wing at Supersonic Speeds.* NASA TP-1027, 1977.

20. Steinbrenner, John P.; and Chawner, John R.: *The GRIDGEN Version 8 Multiple Block Grid Generation Software.* MDA Engineering Report 92-01, 1992.

21. Richardson, Pamela F.; McClinton, Charles R.; Bittner, Robert D.; Dilley, A. Douglas; and Edwards, Kelvin W.: *Hypersonic CFD Applications for the National Aero-Space Plane.* SAE 892310, Sept. 1989.

22. McGrory, W. D.; Huebner, L. D.; Slack, D. C.; and Walters, R. W.: Development and Application of GASP 2.0. AIAA-92-5067, Dec. 1992.

23. McGrory, William D.; Slack, David C.; Applebaum, Michael P.; and Walters, Robert W.: *GASP Version 2.2—The General Aerodynamic Simulation Program.* AeroSoft, Inc., 1993.

24. Takashima, Naruhisa: *Navier-Stokes Computations of a Viscous Optimized Waverider.* NASA CR-189658, 1992.

25. Bushnell, D. M.: Supersonic Aircraft Drag Reduction. AIAA-90-1596, June 1990.

26. Chapman, Dean R.: *Reduction of Profile Drag at Supersonic Velocities by the Use of Airfoil Sections Having a Blunt Trailing Edge.* NACA TN-3503, 1955. (Supersedes NACA RM A9H11.)

27. Dutton, J.; Herrin, J.; Molezzi, M.; Mathur, T.; and Smith, K.: Some Problems in Transonic Aerodynamics. AIAA-95-0476, Jan. 1995.

28. Penland, Jim A.; Hallissy, James B.; and Dillon, James L.: *Aerodynamic Characteristics of a Hypersonic Research Airplane Concept Having a 70° Swept Double-Delta Wing at Mach Numbers From 0.80 to 1.20, With Summary of Data From 0.20 to 6.0.* NASA TP-1552, 1979.

29. Dillon, James L.; and Pittman, Jimmy L.: *Aerodynamic Characteristics at Mach 6 of a Wing-Body Concept for a Hypersonic Research Airplane.* NASA TP-1249, 1978.

30. Penland, Jim A.; Edwards, Clyde L. W.; Witcofski, Robert D.; and Marcum, Don C., Jr.: *Comparative Aerodynamic Study of Two Hypersonic Cruise Aircraft Configurations Derived From Trade-Off Studies.* NASA TM X-1436, 1967.

31. Small, William J.; Kirkham, Frank S.; and Fetterman, David E.: *Aerodynamic Characteristics of a Hypersonic Transport Configuration at Mach 6.86.* NASA TN-D-5885, 1970.

32. Watts, Joe D.; Olinger, Frank V.; Weidner, John P.; Johnson, Stuart K.; Sanders, Bobby W.; and Keyes, J. Wayne: Mach 5 Cruise Aircraft Research. *Proceedings of the Langley Symposium on Aerodynamics,* Volume 2, Sharon H. Stack, Compiler, NASA CP-2398, 1986, pp. 285–304.

33. Ellison, James C.: *Investigation of the Aerodynamic Characteristics of a Hypersonic Transport Model at Mach Numbers to 6.* NASA TN D-6191, 1971.

34. Williams, John E.; and Vukelich, Steven R.: *The USAF Stability and Control Digital Datcom. Volume I: User's Manual.* AFFDL-TR-79-3032-VOL-1, Apr. 1979. (Supersedes AFFDL-TR-73-23, AFFDL-TR-74-68, and AFFDL-TR-76-45-VOL-1.)

Table 1. Characteristics of Straight-Wing Waverider Designed by MAXWARP

Waverider length, in.	24.0
Span/length	0.83
Base height/length	0.092
Volumetric efficiency (V_{eff})	0.112
Planform area, S_{ref}, ft^2	1.89
Predicted maximum L/D	6.9
Base area, ft^2	0.136

Table 2. Characteristics of Cranked-Wing Waverider Designed by MAXWARP

Waverider length, in.	24.0
Span/length	0.96
Base height/length	0.092
Volumetric efficiency (V_{eff})	0.108
Planform area, S_{ref}, ft^2	2.05
Predicted maximum L/D	6.7
Base area, ft^2	0.153

Table 3. Reference Quantities for Various Configurations

Configuration	S_{ref}, ft^2	Span, in.	Length, in. $\bar{c}$	Base area, ft^2	$X_{c.g.}$, percent of $\bar{c}$
Straight-wing pure model	1.894	19.80	24.0	0.1580	69.3
Straight-wing pure model with engine components	1.894	19.80	24.0	0.1481	69.3
Straight-wing fully integrated model	2.202	19.80	26.60	0.0194	62.5[a]
Cranked-wing pure model	2.052	23.016	24.0	0.1860	69.3
Cranked-wing pure model with engine components	2.052	23.016	24.0	0.1745	69.3
Cranked-wing fully integrated model	2.346	23.016	26.60	0.0194	62.5[b]

[a]For some data: 58.0.
[b]For some data: 59.0.

Table 4. Steady-Roll-Rate Capabilities Calculated From DATCOM for Straight-Wing Fully Integrated Configuration

Mach number	P_{ss} per unit velocity, $\frac{\text{deg/sec}}{\text{ft/sec}}$
2.3	0.119
4.0	0.095
4.63	0.095

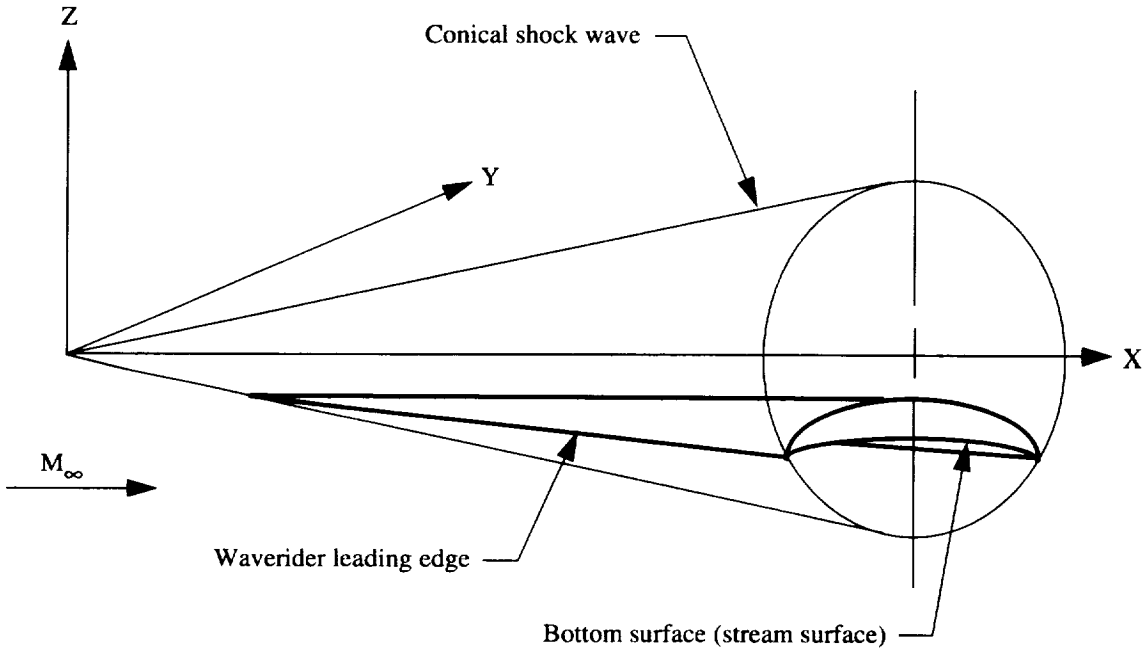

Figure 1. Design of conical-flow-derived waverider.

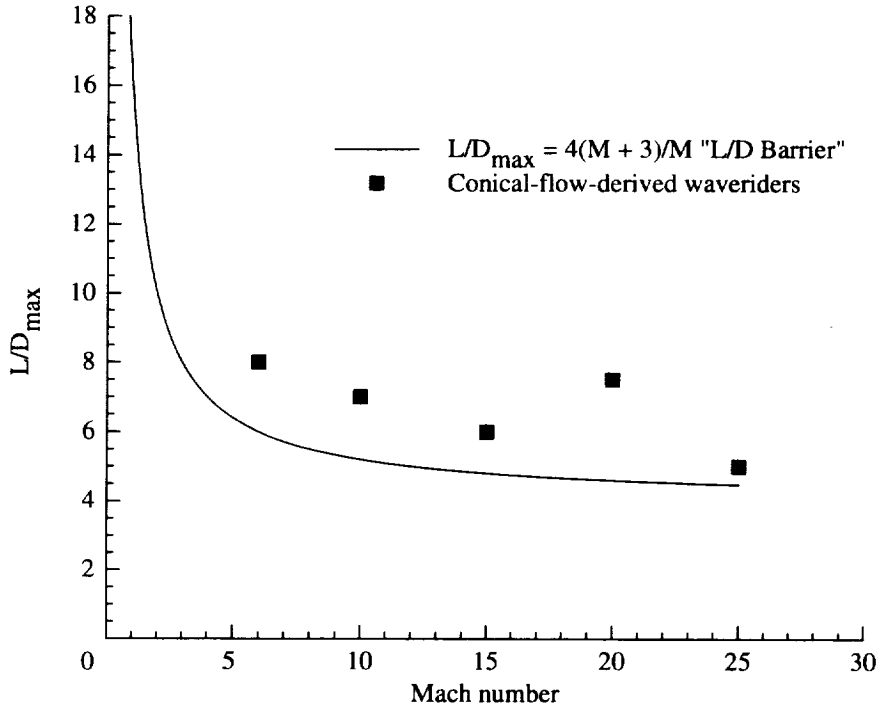

Figure 2. Comparison of L/D_{max} values of conventional vehicles and waveriders.

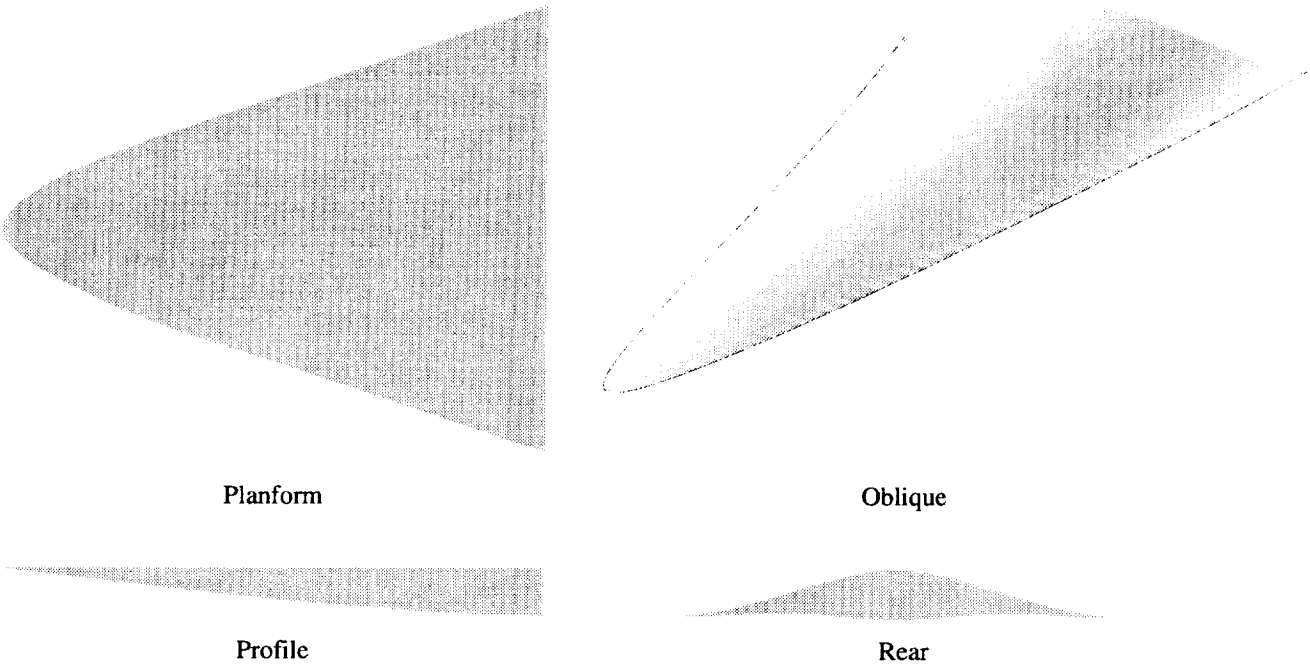

Figure 3. Straight-wing pure waverider shape designed by MAXWARP.

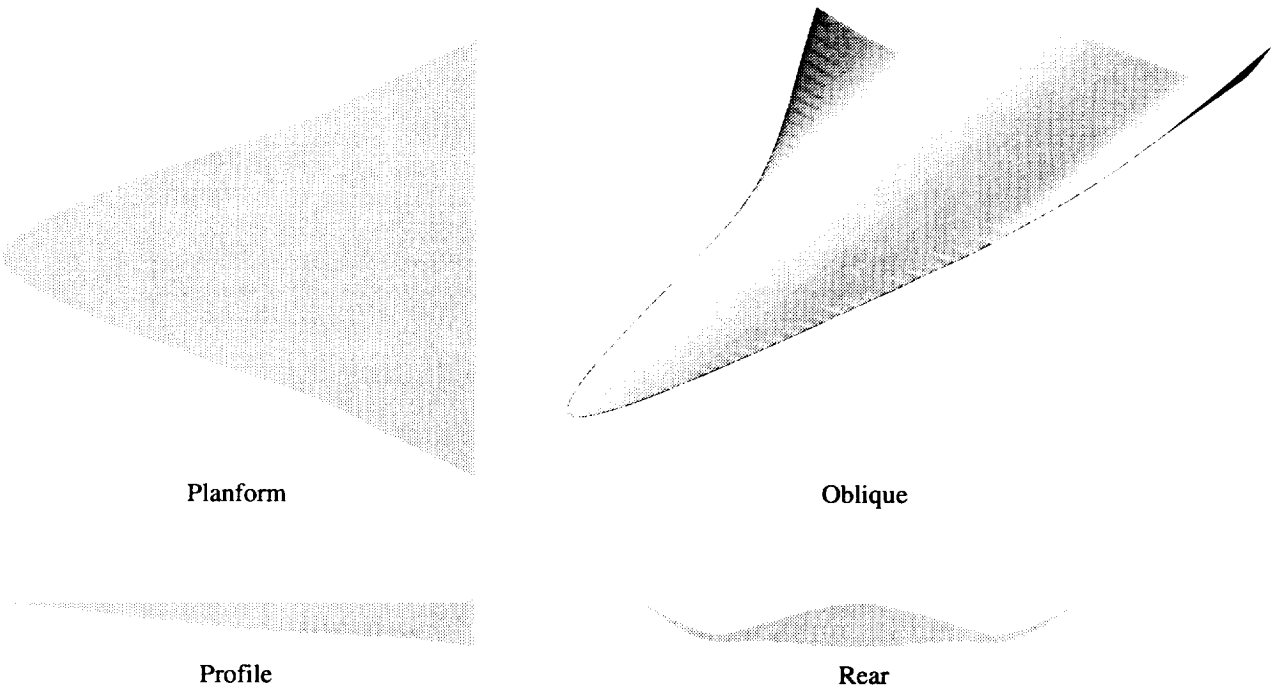

Figure 4. Cranked-wing pure waverider shape designed by MAXWARP.

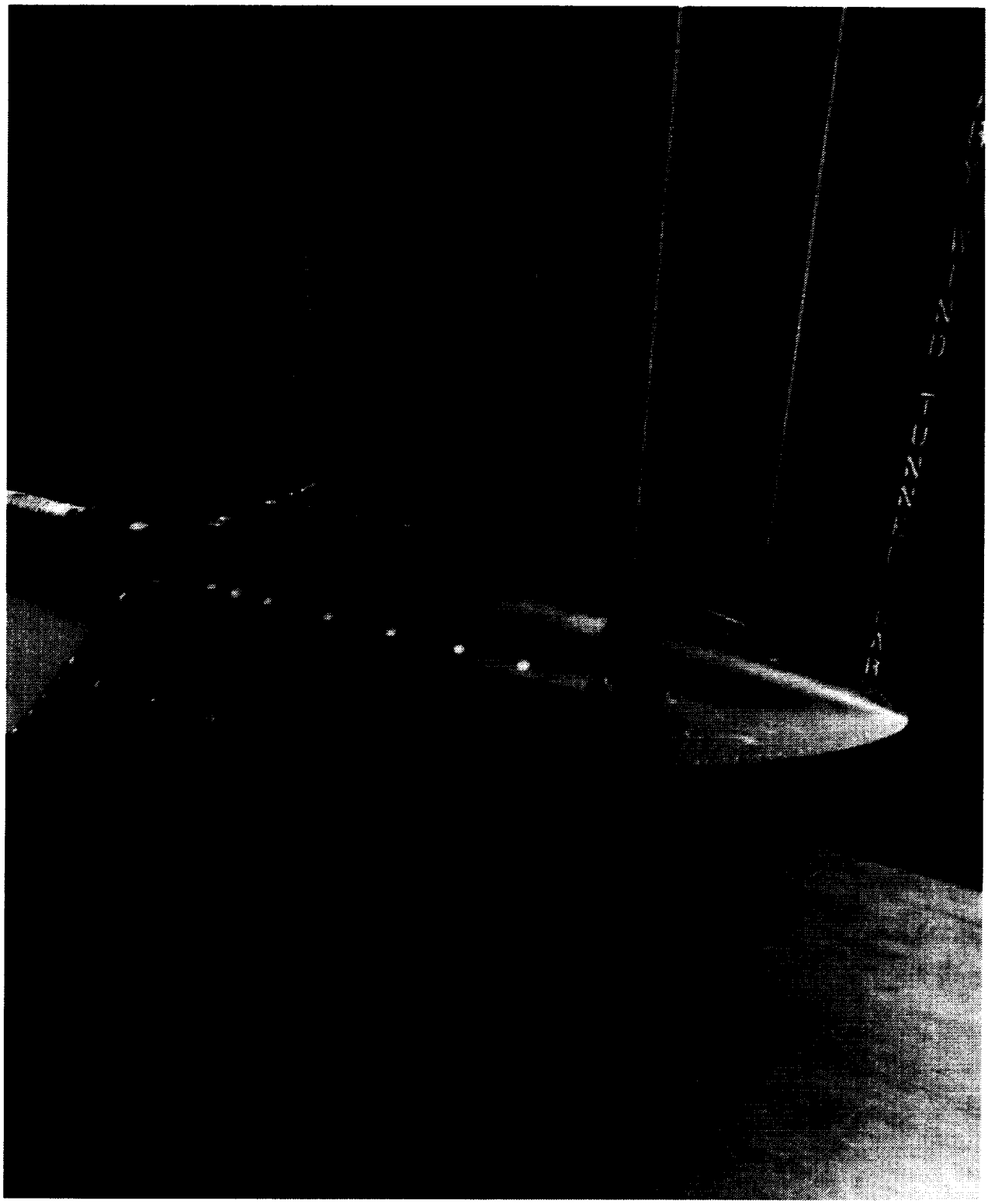

Figure 5. Straight-wing pure waverider model in UPWT.

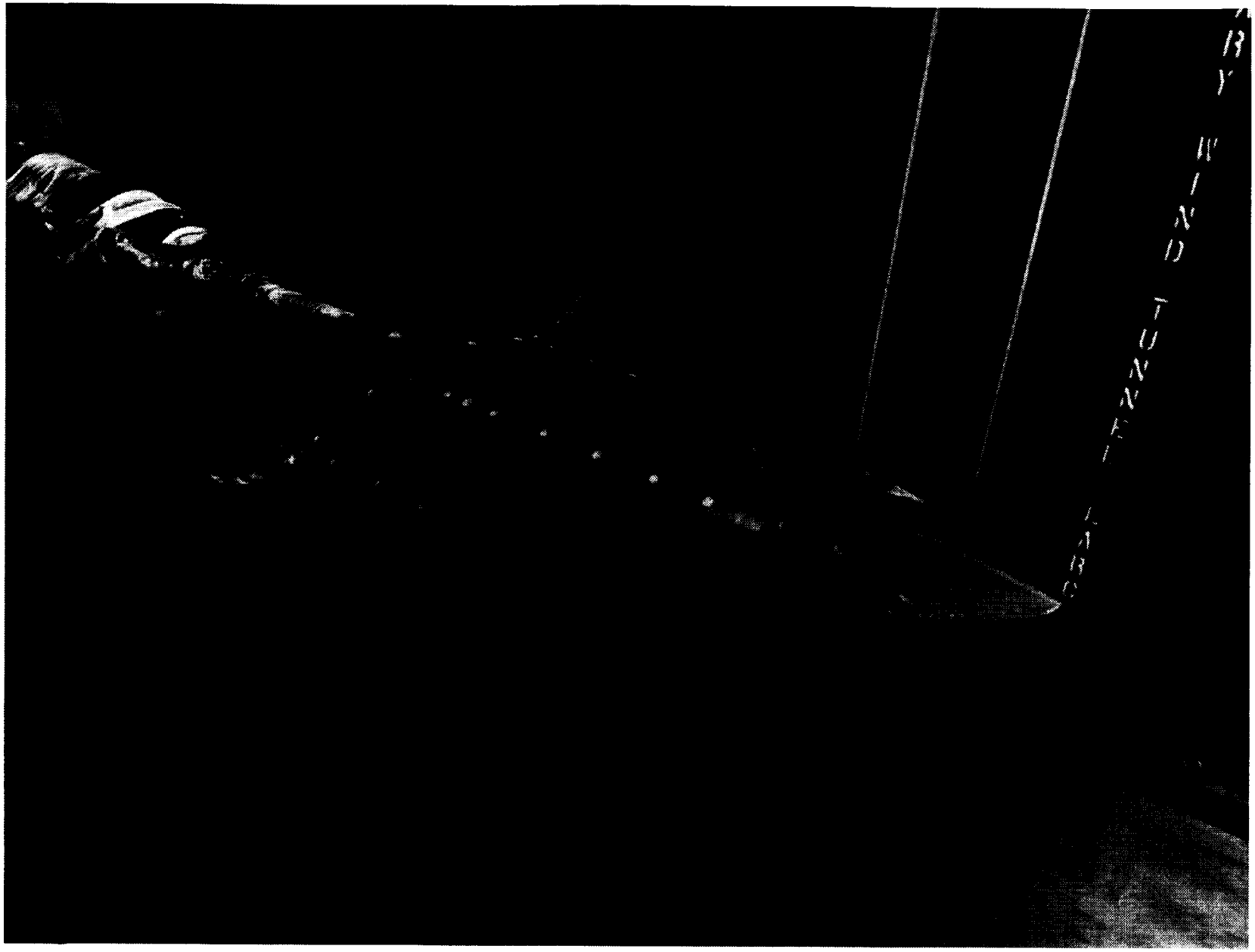

Figure 6. Cranked-wing pure waverider model in UPWT.

Figure 7. Lower surface of cranked-wing pure waverider model.

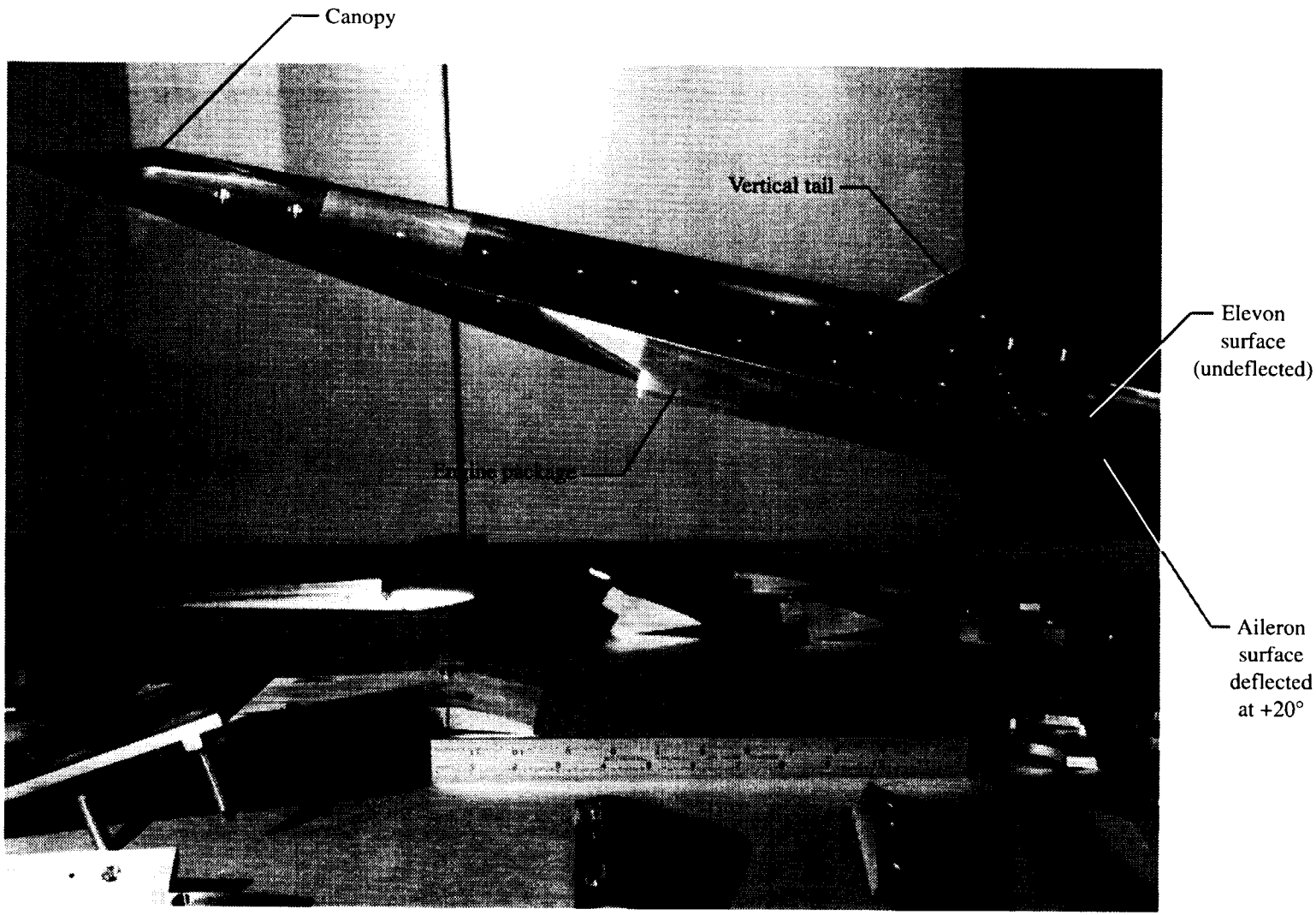

Figure 8. Straight-wing fully integrated waverider model.

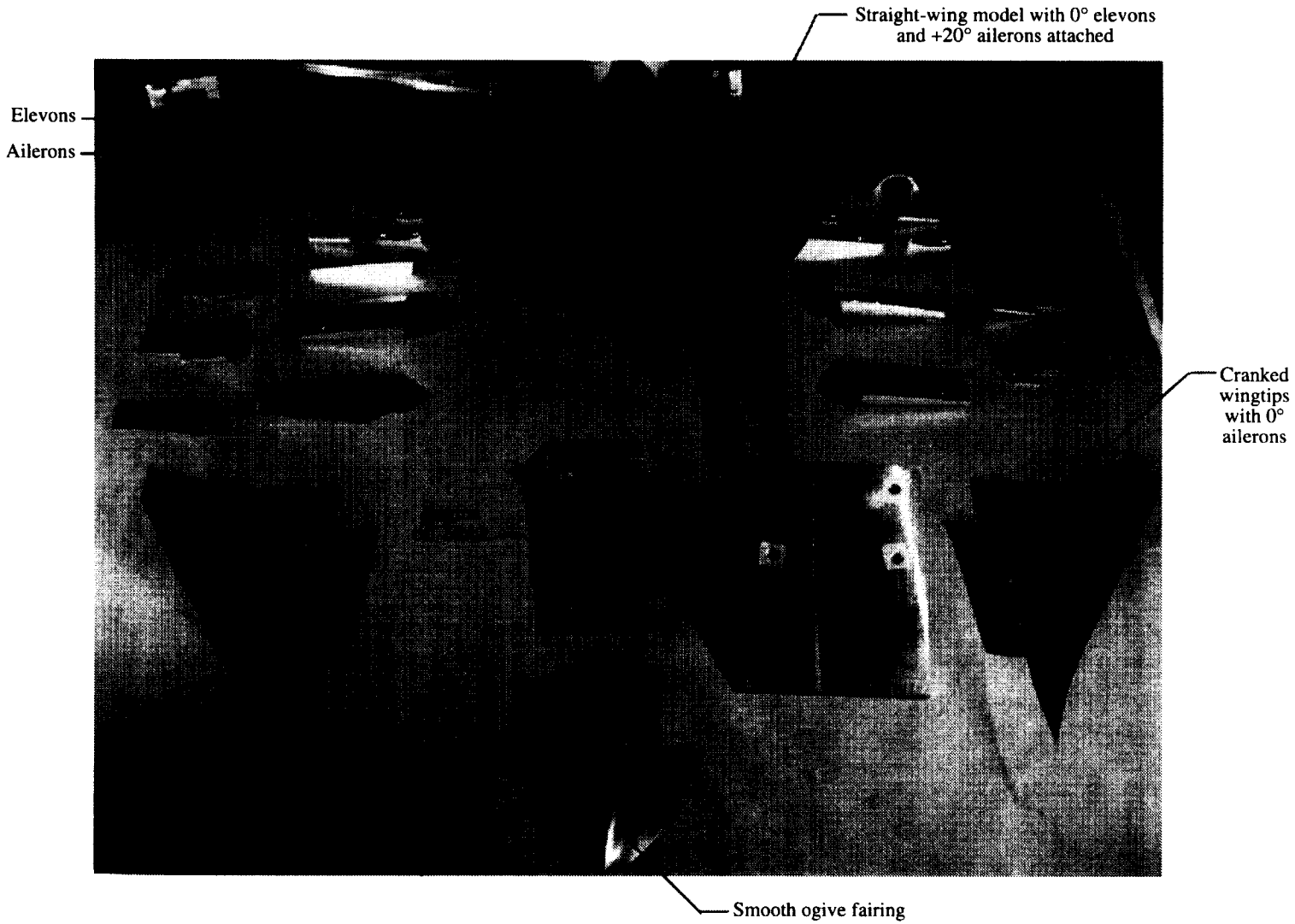

Figure 9. Fully integrated model with various components.

Tap No.	Model Sta.	B.L.	W.L.
1	22.030	–1.353	–1.785
2	22.030	–1.015	–1.788
3	22.030	–0.676	–1.792
4	22.030	–0.338	–1.796
5	22.791	–1.353	–1.244
6	22.791	–1.015	–1.252
7	22.791	–0.676	–1.254
8	22.791	–0.338	–1.255
9	23.552	–1.353	–0.964
10	23.552	–1.015	–0.974
11	23.552	–0.676	–0.974
12	23.552	–0.338	–0.975

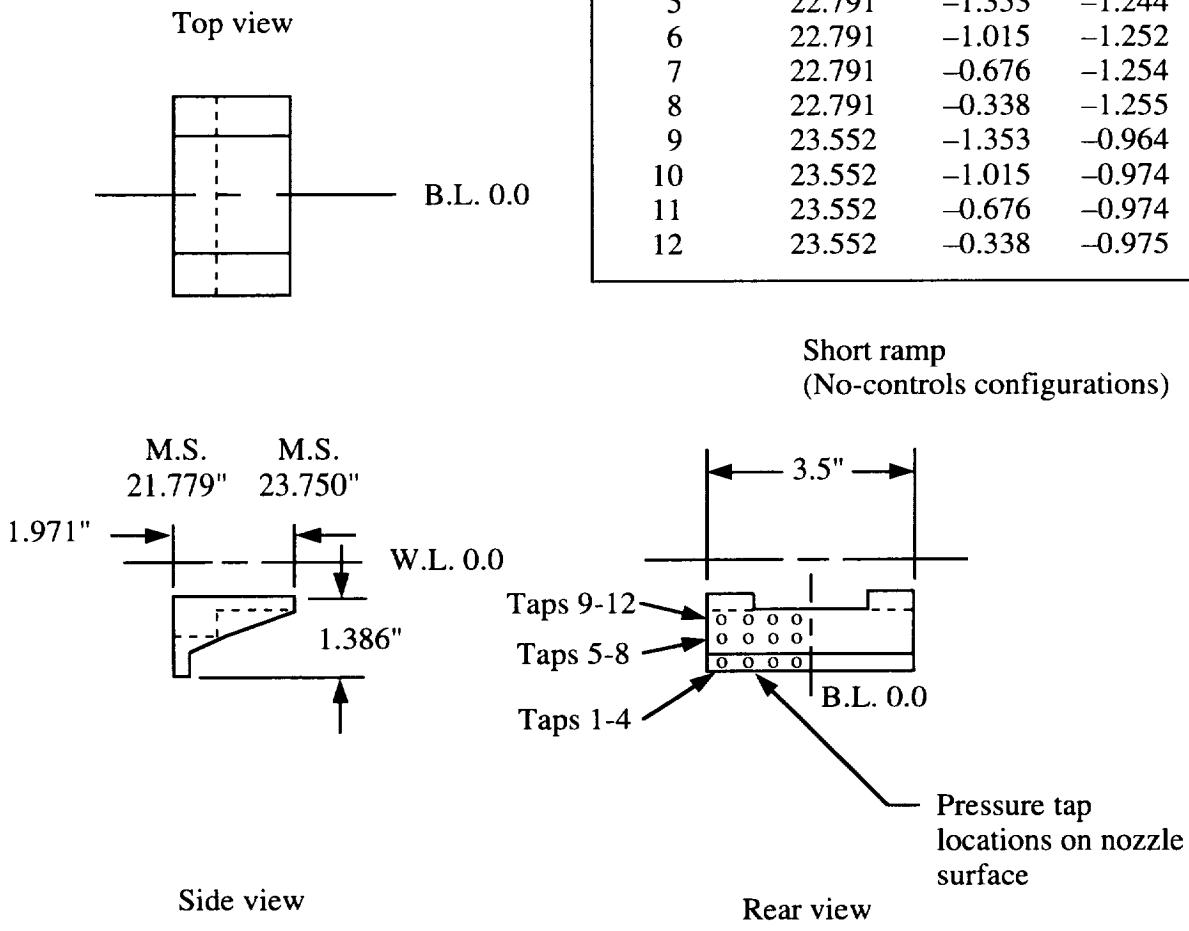

(a) Short expansion ramp used with no-controls configurations.

Figure 10. Three-view drawings of expansion ramps.

Tap No.	Model Sta.	B.L.	W.L.
13	24.313	–1.353	–0.724
14	24.313	–1.015	–0.731
15	24.313	–0.676	–0.734
16	24.313	–0.338	–0.745
17	25.075	–1.353	–0.516
18	25.075	–1.015	–0.523
19	25.075	–0.676	–0.532
20	25.075	–0.338	–0.739
21	25.836	–1.353	–0.332
22	25.836	–1.015	–0.339
23	25.836	–0.676	–0.451
24	25.836	–0.338	–0.739

Locations for taps 1 to 12 are given on previous page.

Long ramp
(Fully integrated configurations)

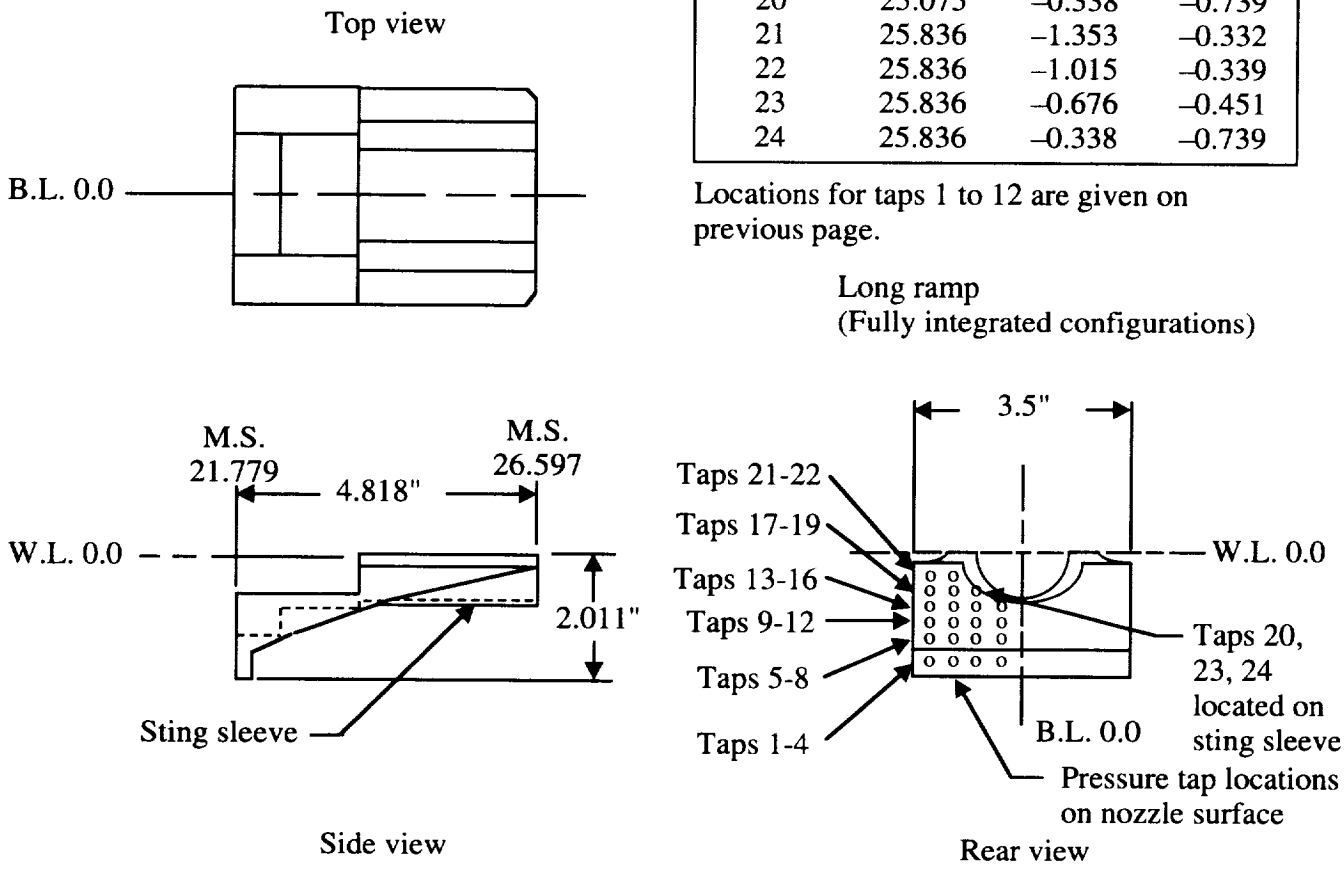

(b) Long expansion ramp used with fully integrated configurations.

Figure 10. Concluded.

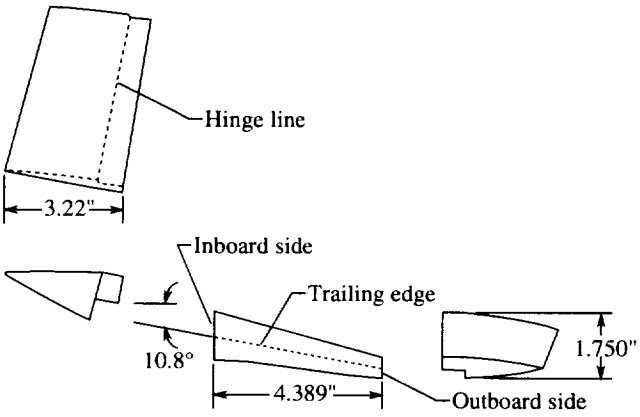

(a) Elevons.

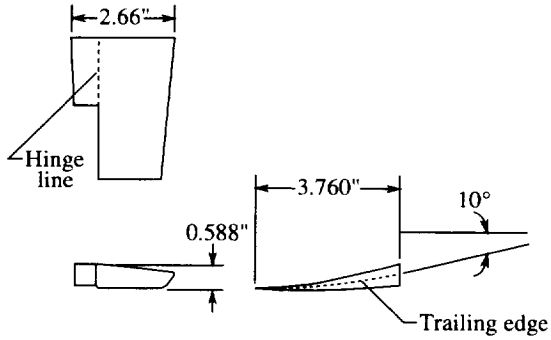

(b) Straight-wing ailerons.

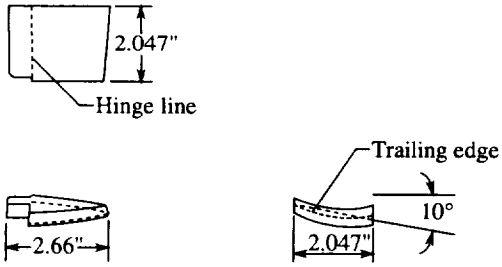

(c) Cranked-wing inboard ailerons.

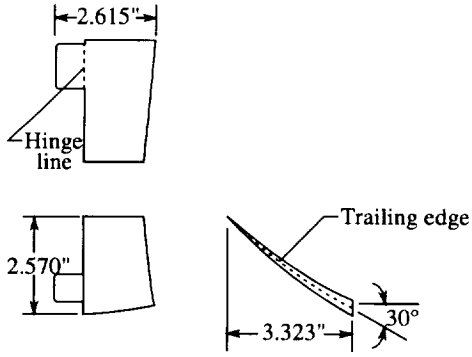

(d) Cranked-wing outboard ailerons.

Figure 11. Dimensions of elevons and ailerons.

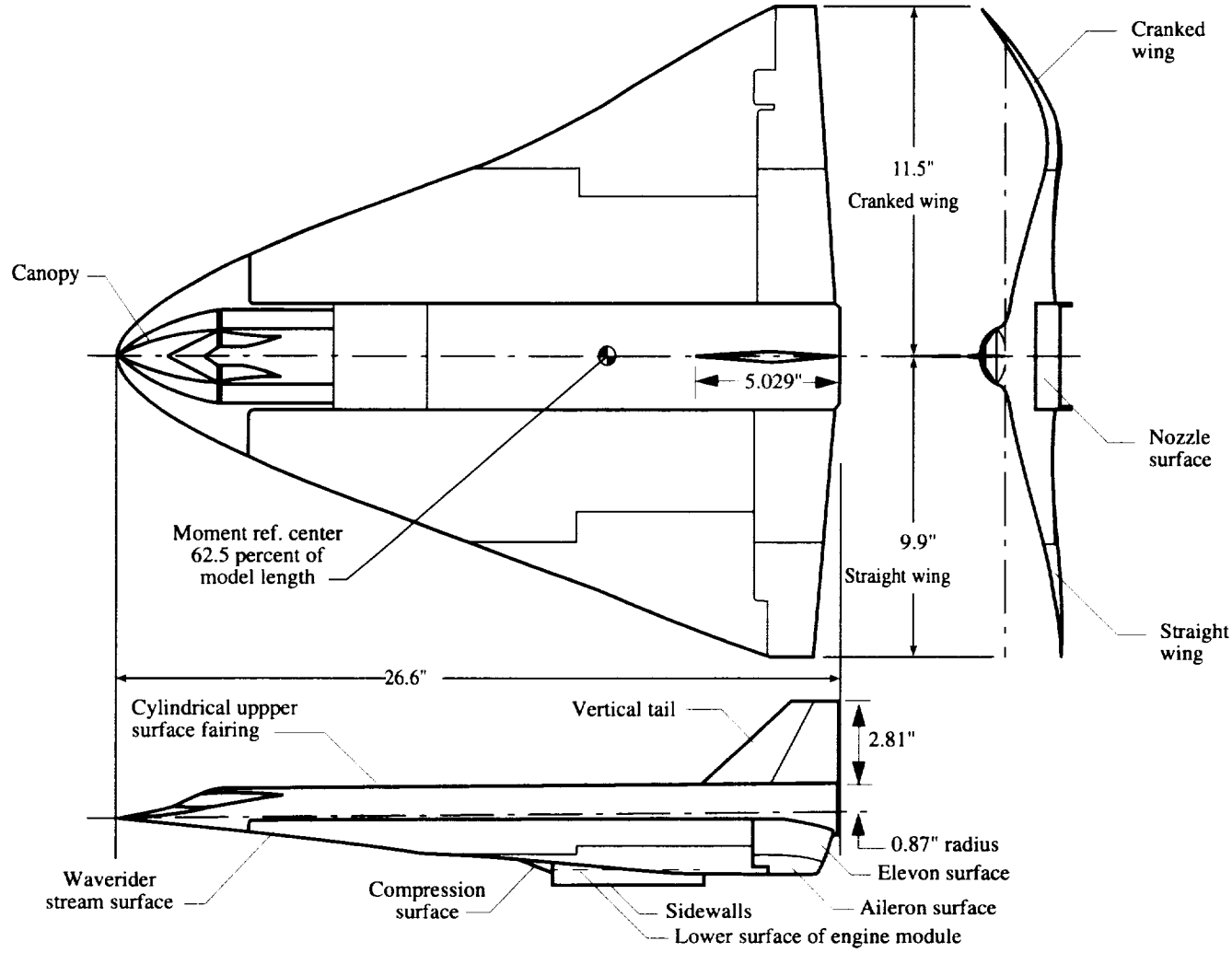

Figure 12. Three-view drawing of fully integrated waverider model.

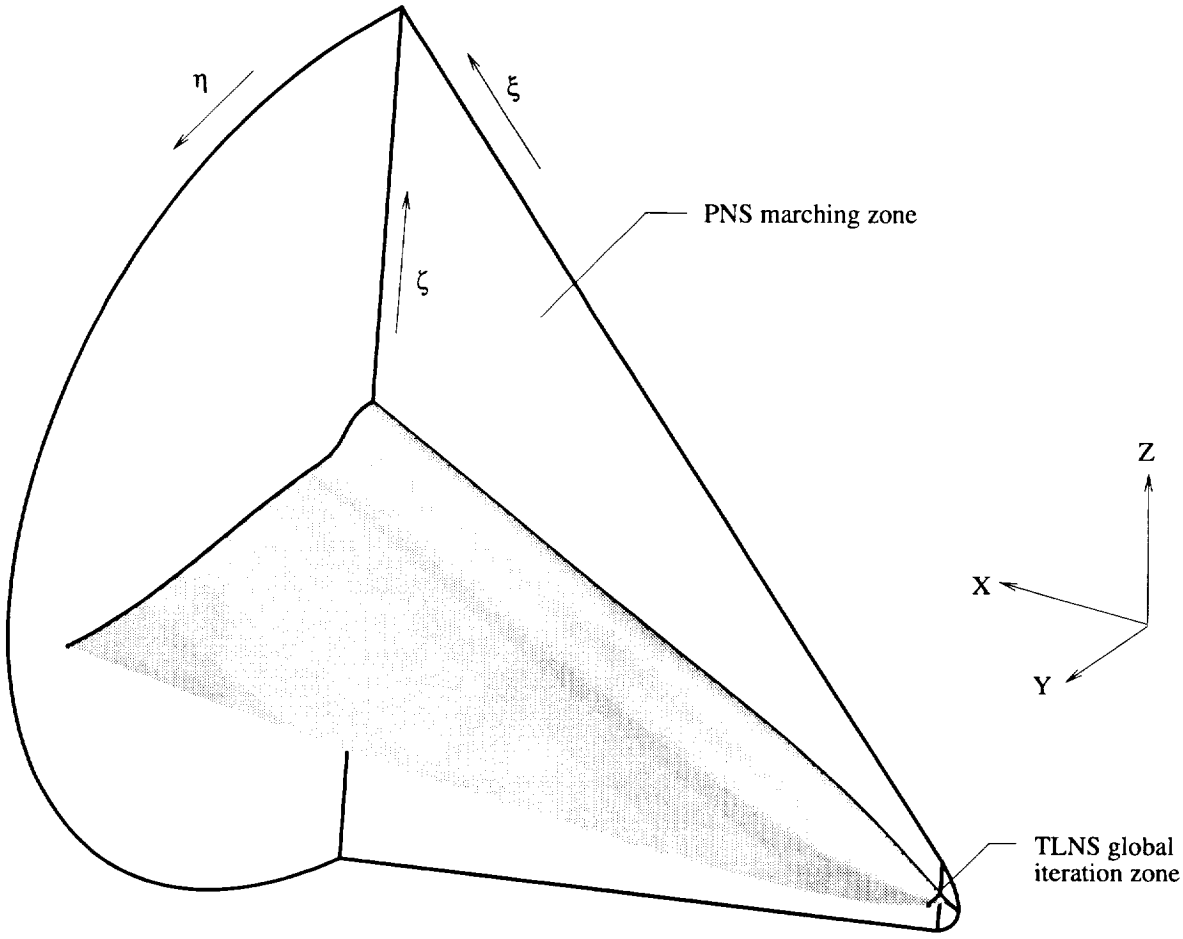

Figure 13. Coordinates and computational scheme for waverider CFD solutions.

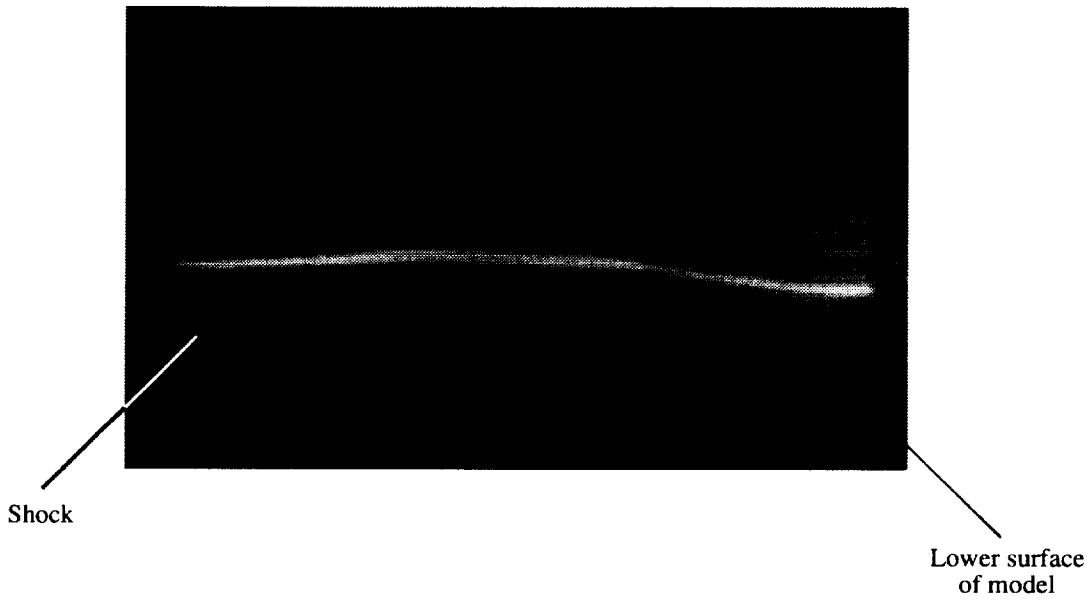

(a) Vapor-screen photograph of base.

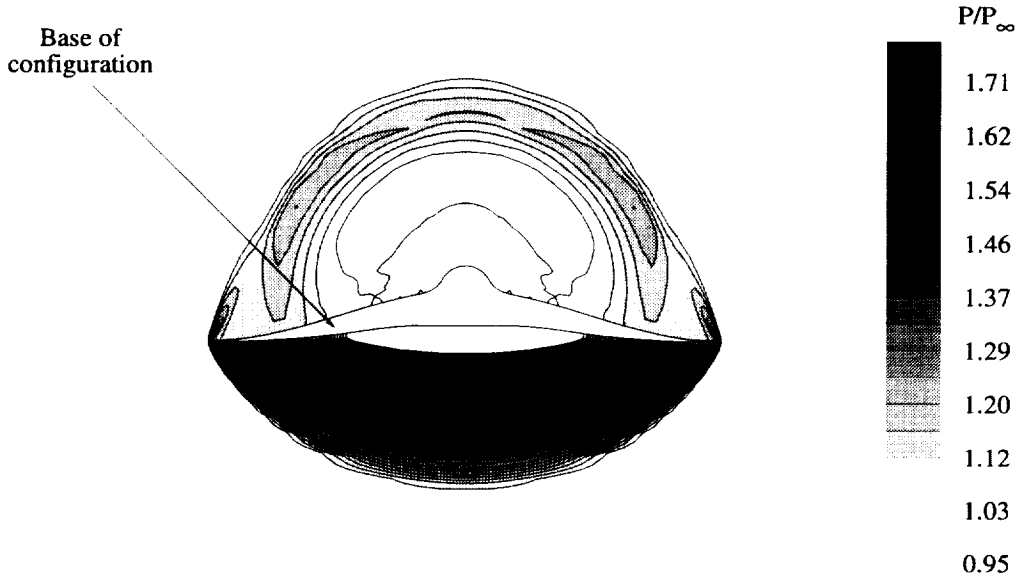

(b) Base view of CFD solution.

Figure 14. Comparison of base-view vapor-screen photograph and CFD nondimensional static pressure contours of straight-wing pure waverider model at $M = 4.0$ and $\alpha = 0°$.

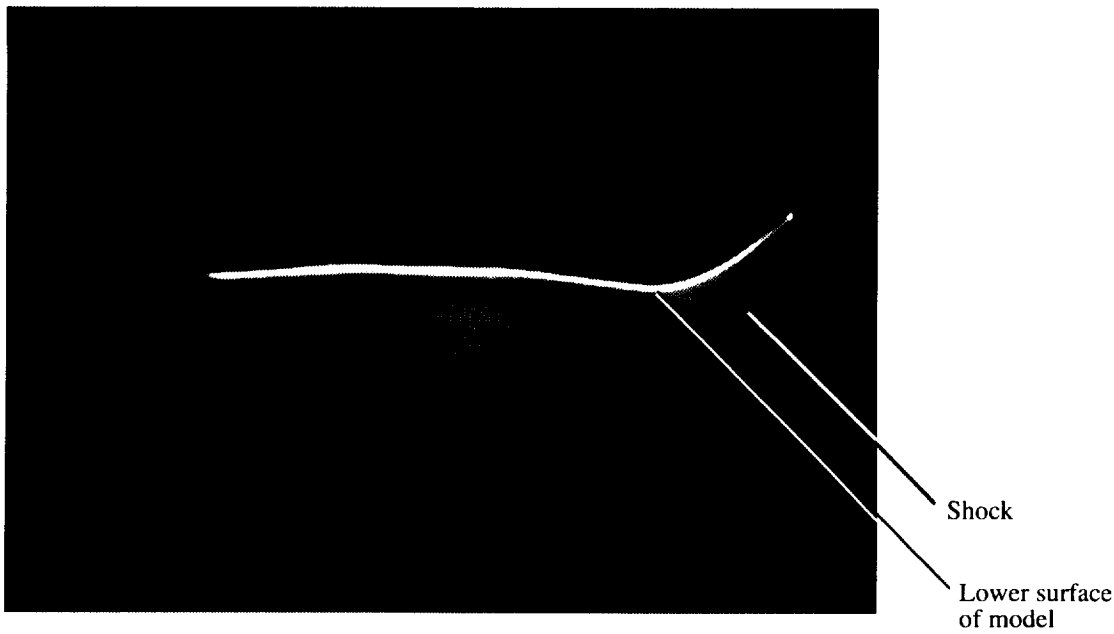

(a) Vapor-screen photograph of base.

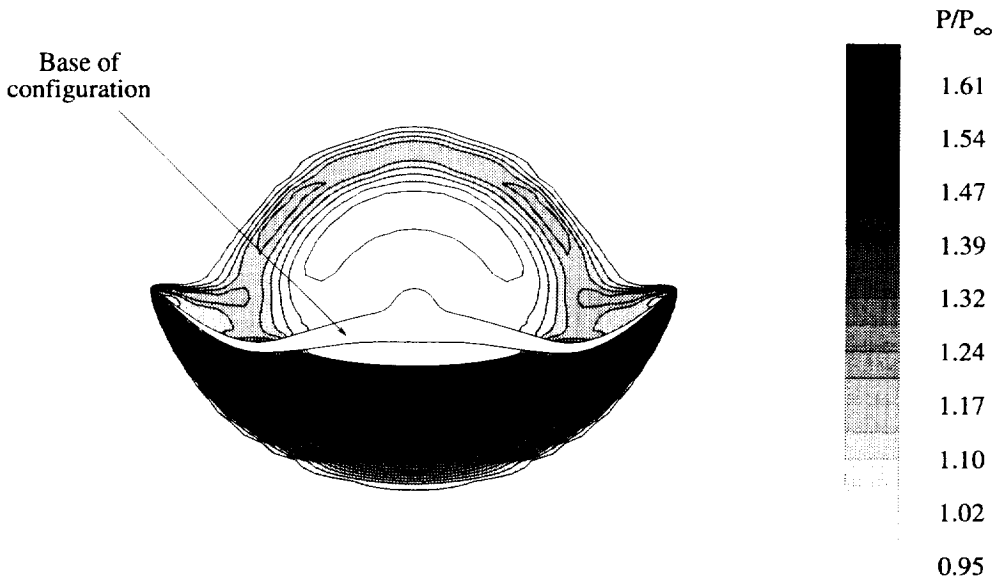

(b) Base view of CFD solution.

Figure 15. Comparison of base-view vapor-screen photograph and CFD nondimensional static pressure contours of pure cranked-wing waverider model at $M = 4.0$ and $\alpha = 0°$.

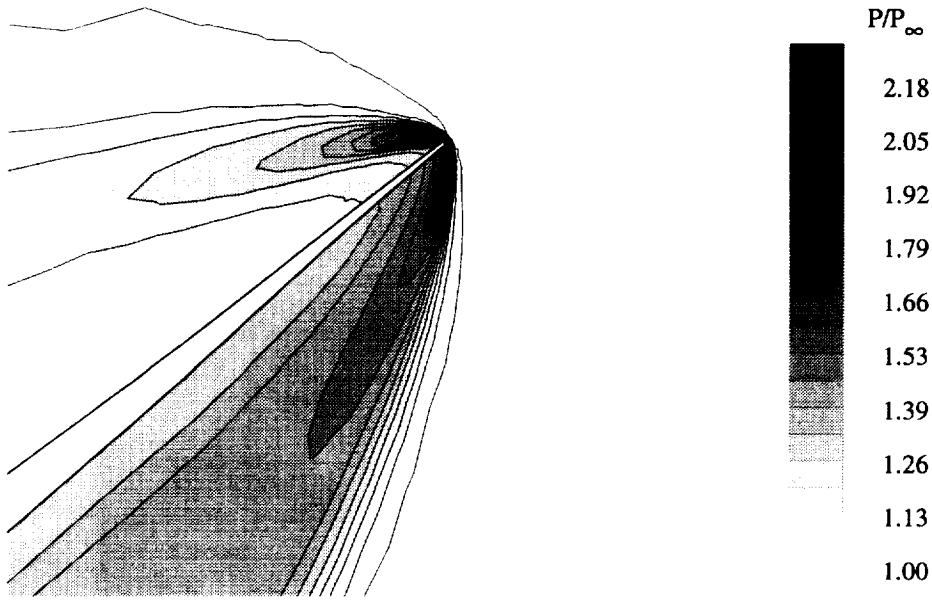

(a) Cranked-wing pure waverider model.

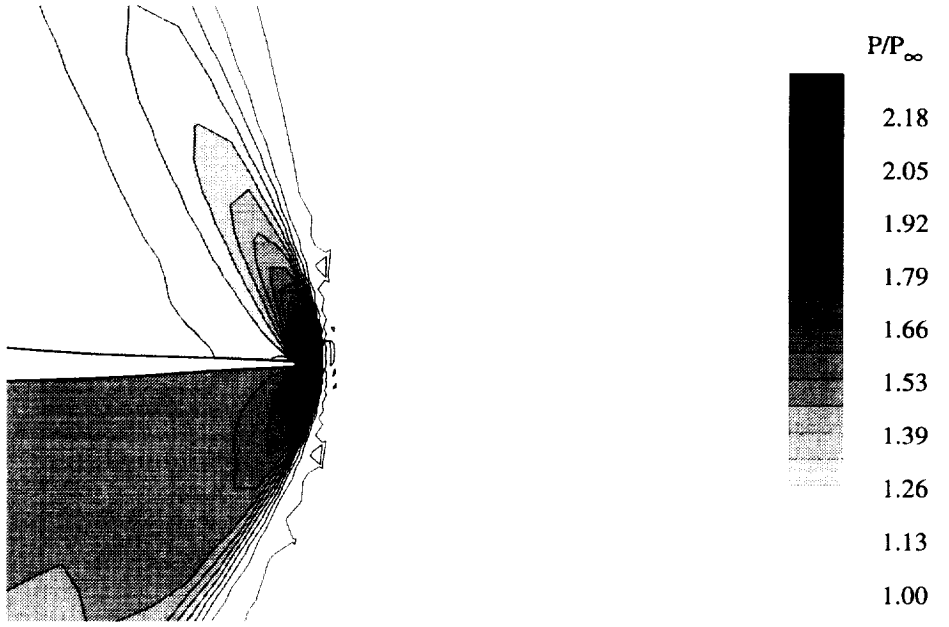

(b) Straight-wing pure waverider model.

Figure 16. Comparison of CFD nondimensional static pressure contours near leading edge at base of cranked-wing and straight-wing pure waverider models at $M = 4.0$ and $\alpha = 0°$.

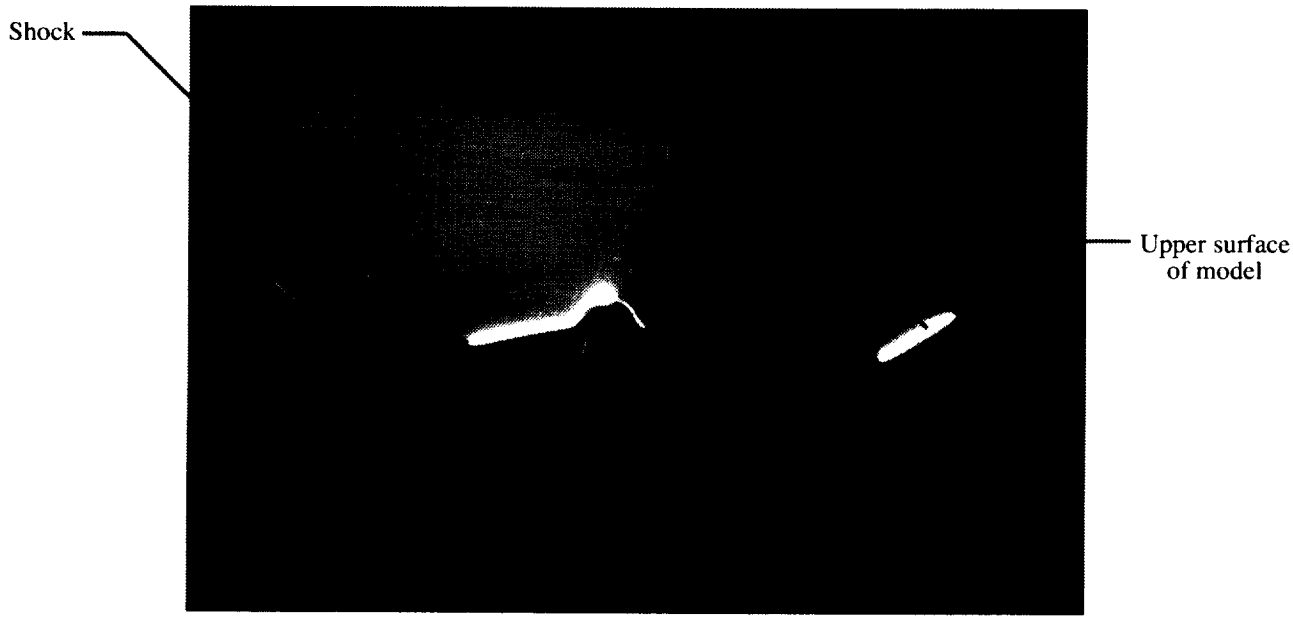

(a) Vapor-screen photograph at base.

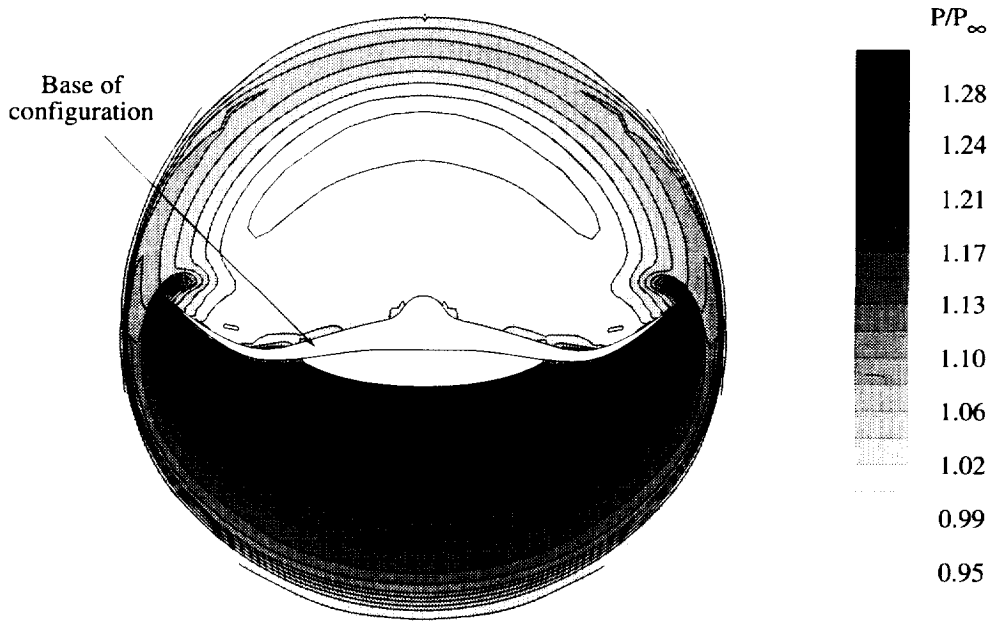

(b) Base view of CFD solution.

Figure 17. Comparison of base-view vapor-screen photograph and CFD nondimensional static pressure contours of cranked-wing pure waverider model at $M = 2.3$ and $\alpha = 0°$.

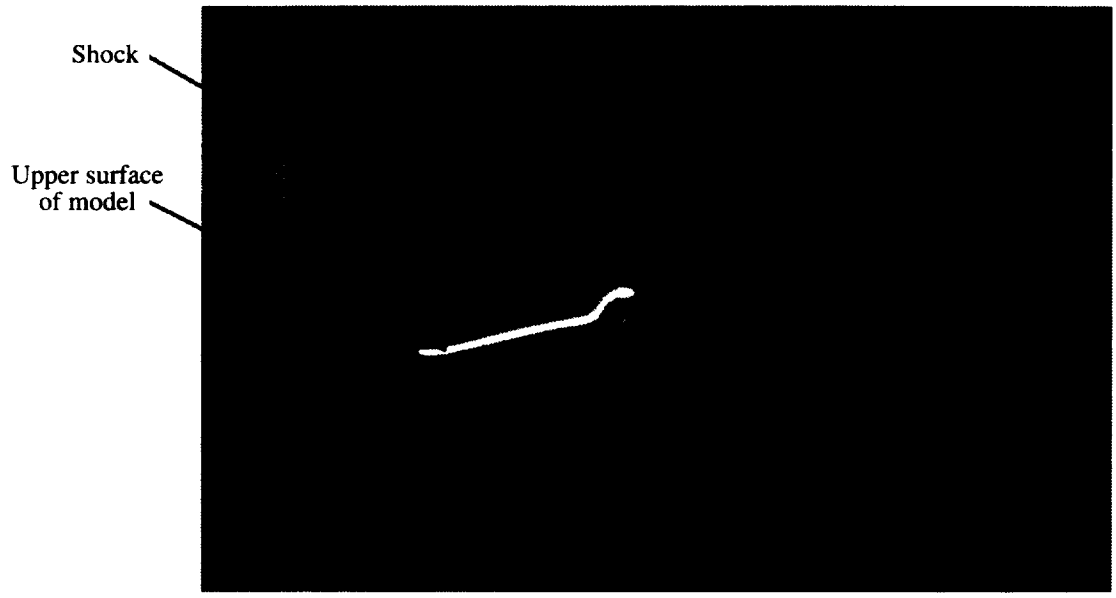

(a) Vapor-screen photograph 5 in. upstream of base.

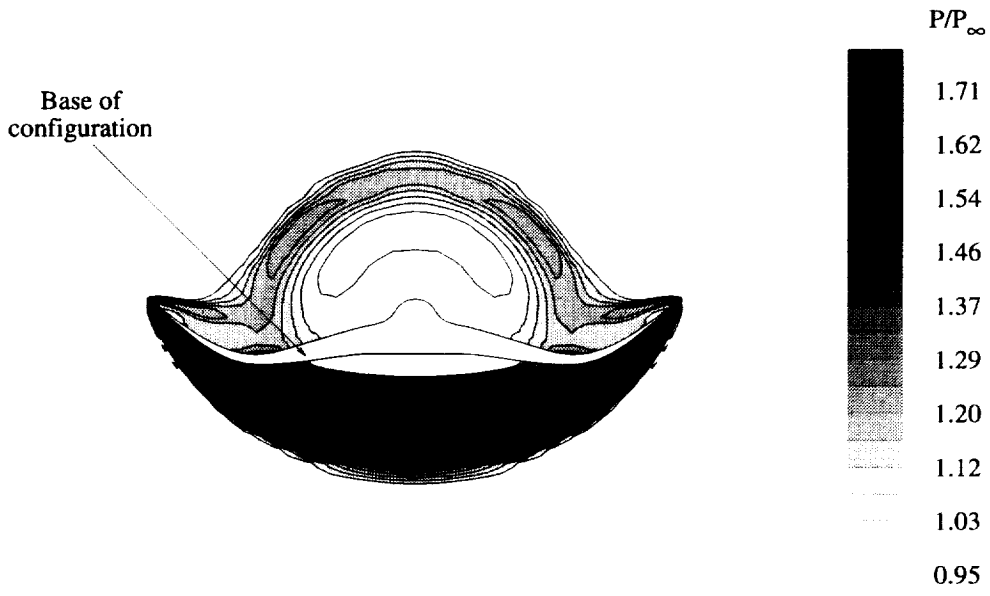

(b) Base view of CFD solution.

Figure 18. Comparison of base-view vapor-screen photograph and CFD nondimensional static pressure contours of cranked-wing pure waverider model at $M = 4.63$ and $\alpha = 0°$.

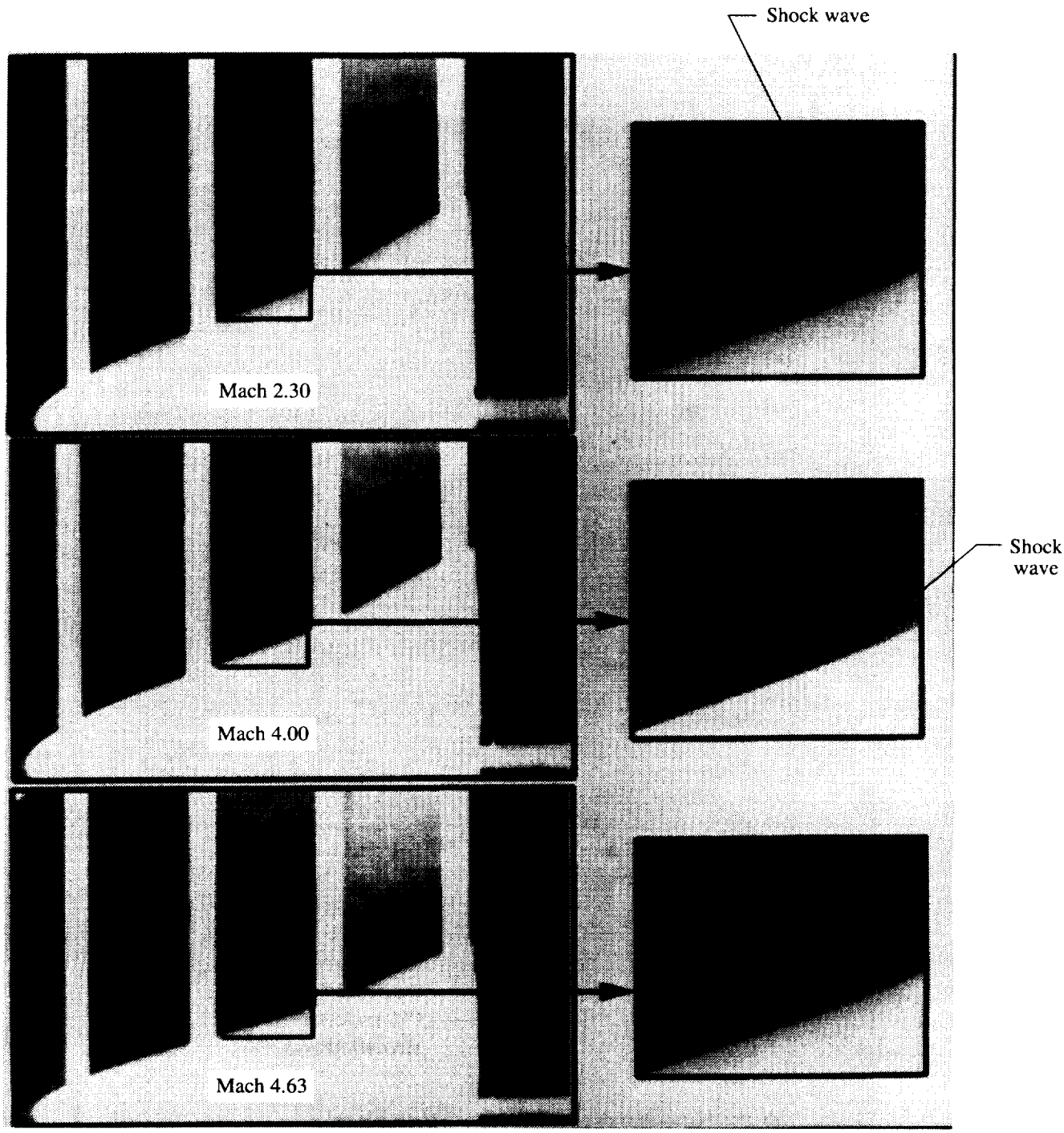

Figure 19. Comparison of planform schlieren photographs of cranked-wing pure waverider model at $M = 2.3$, 4.0, and 4.63.

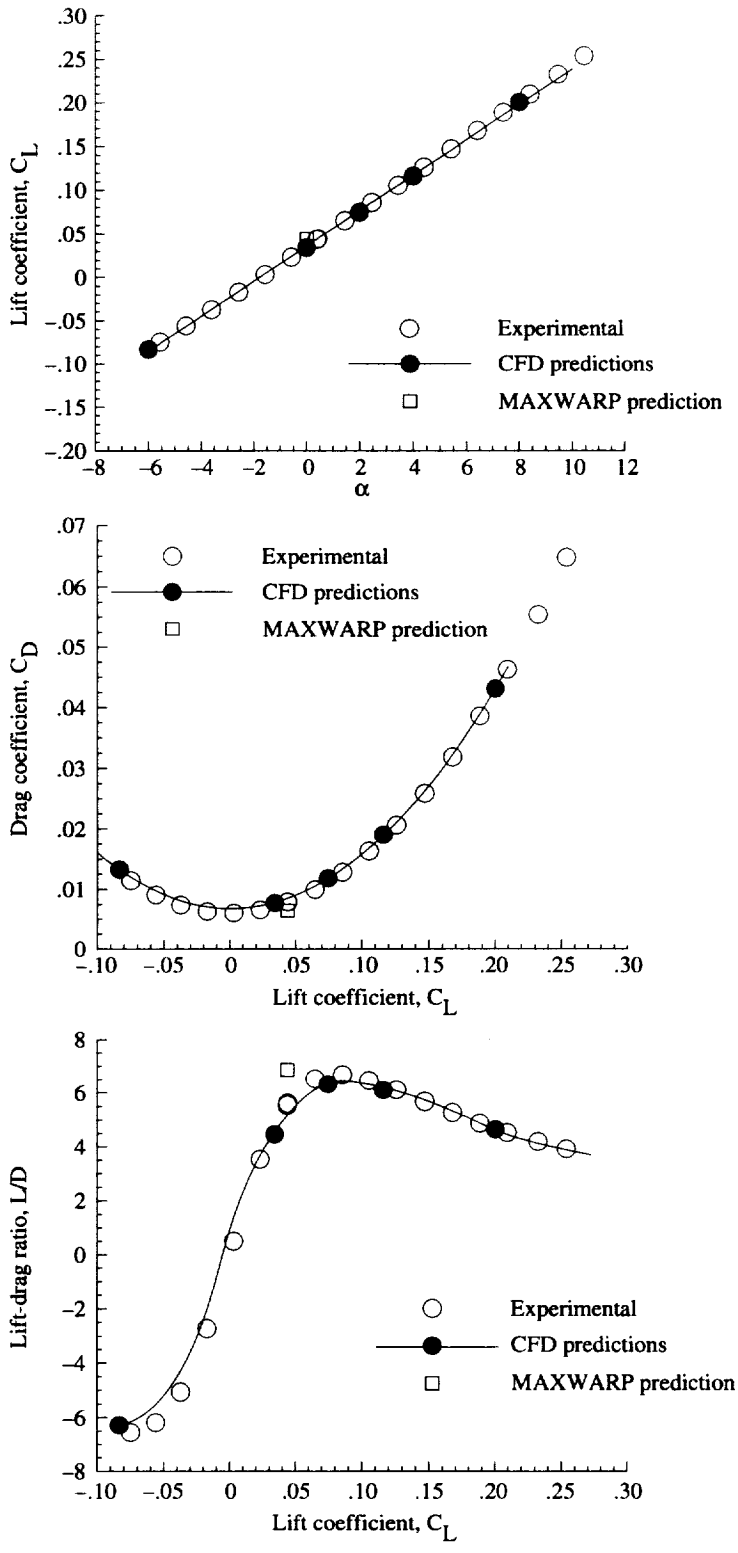

Figure 20. Comparison of experimental data, CFD predictions, and design-code predictions for aerodynamic performance of straight-wing pure waverider model at $M = 4.0$ and Reynolds number of 2.0×10^6 per foot.

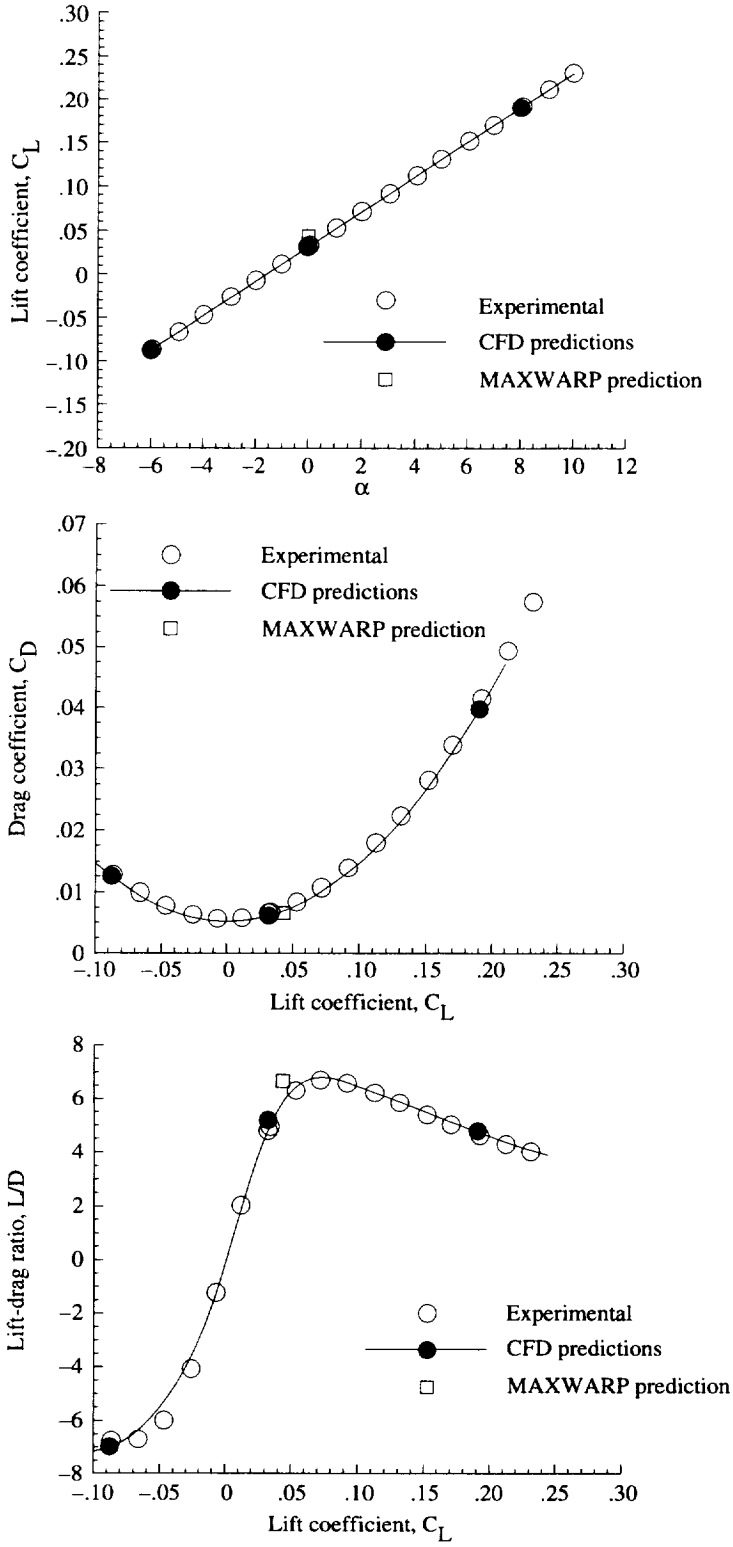

Figure 21. Comparison of experimental data, CFD predictions, and design-code predictions for aerodynamic performance of cranked-wing pure waverider model at $M = 4.0$ and Reynolds number of 2.0×10^6 per foot.

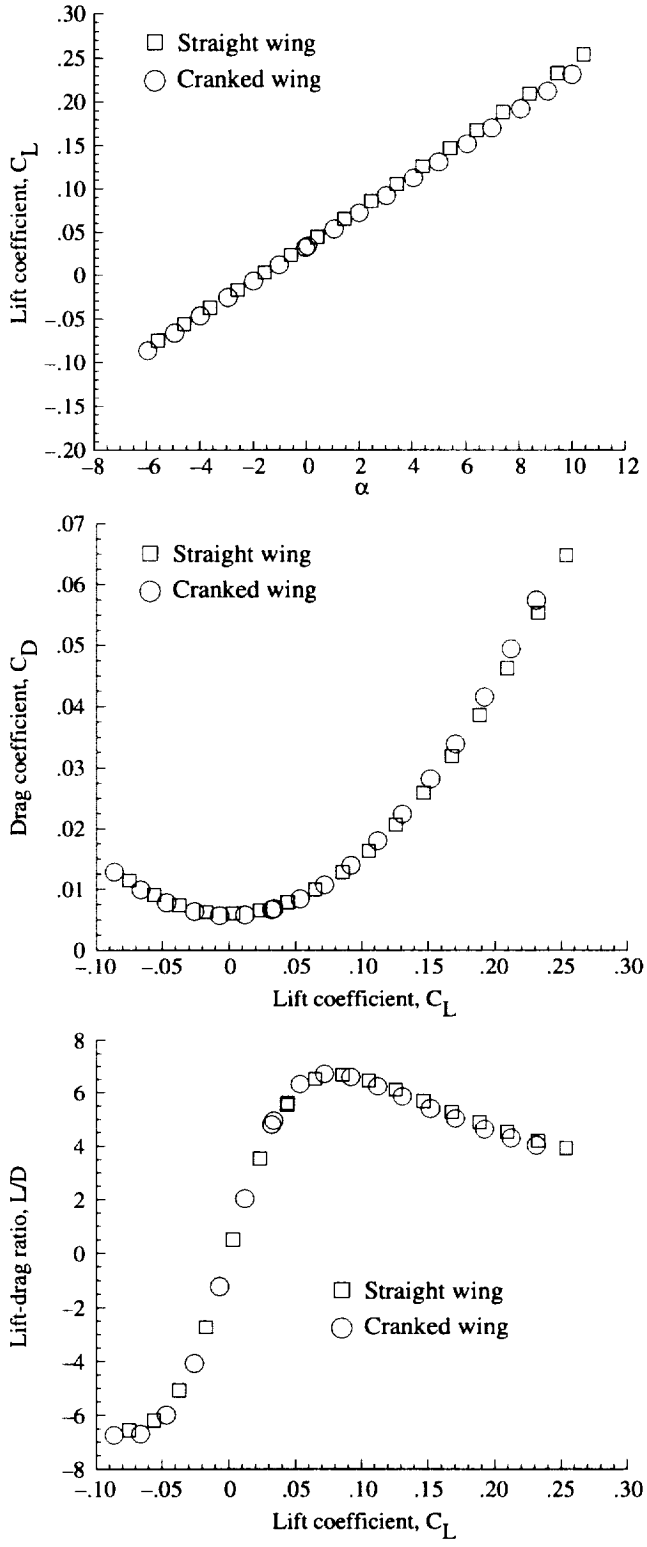

Figure 22. Comparison of aerodynamic performance of straight-wing and cranked-wing pure configurations at $M = 4.0$ and Reynolds number of 2.0×10^6 per foot.

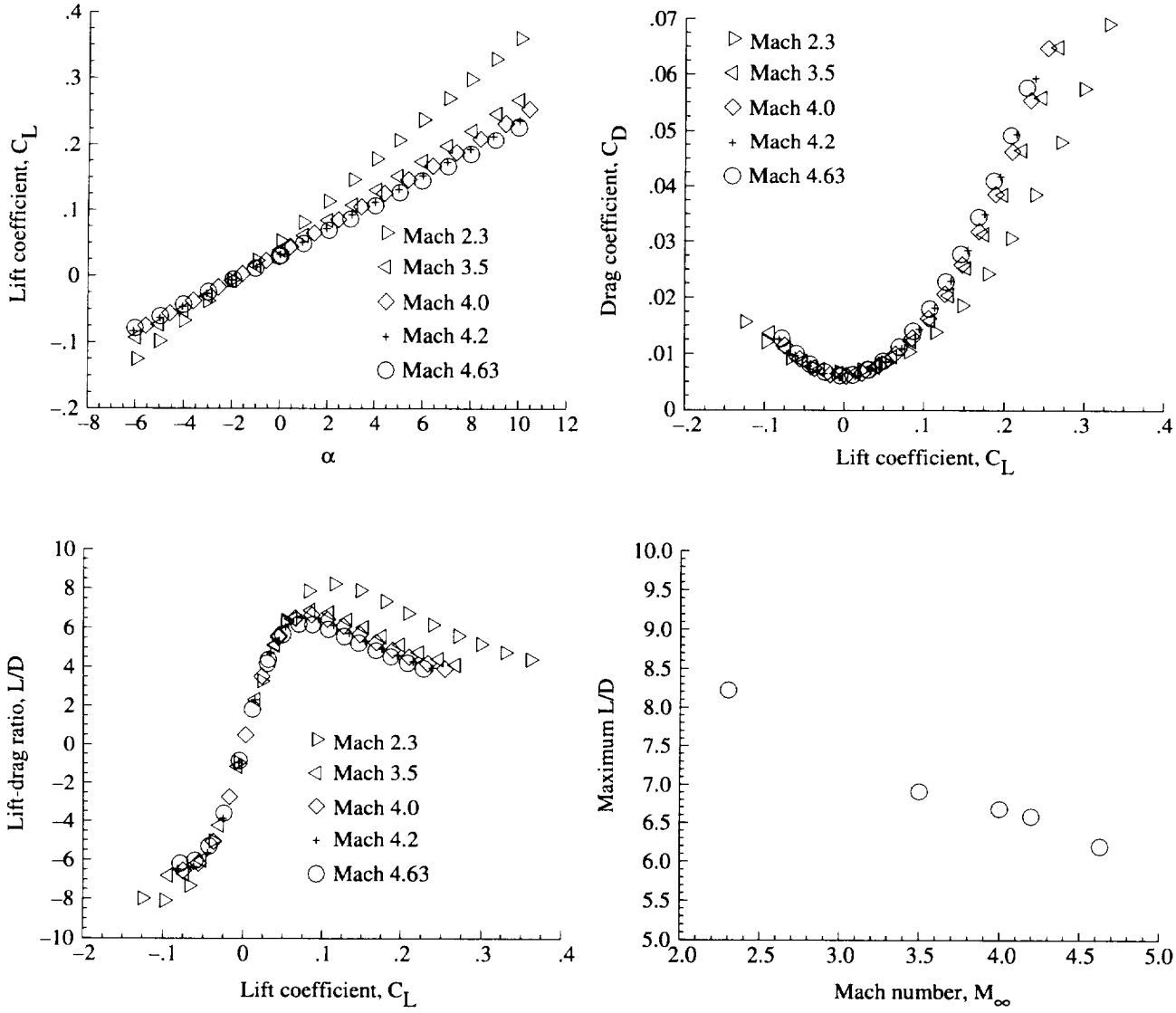

Figure 23. Aerodynamic performance of straight-wing pure waverider configuration across Mach number range studied.

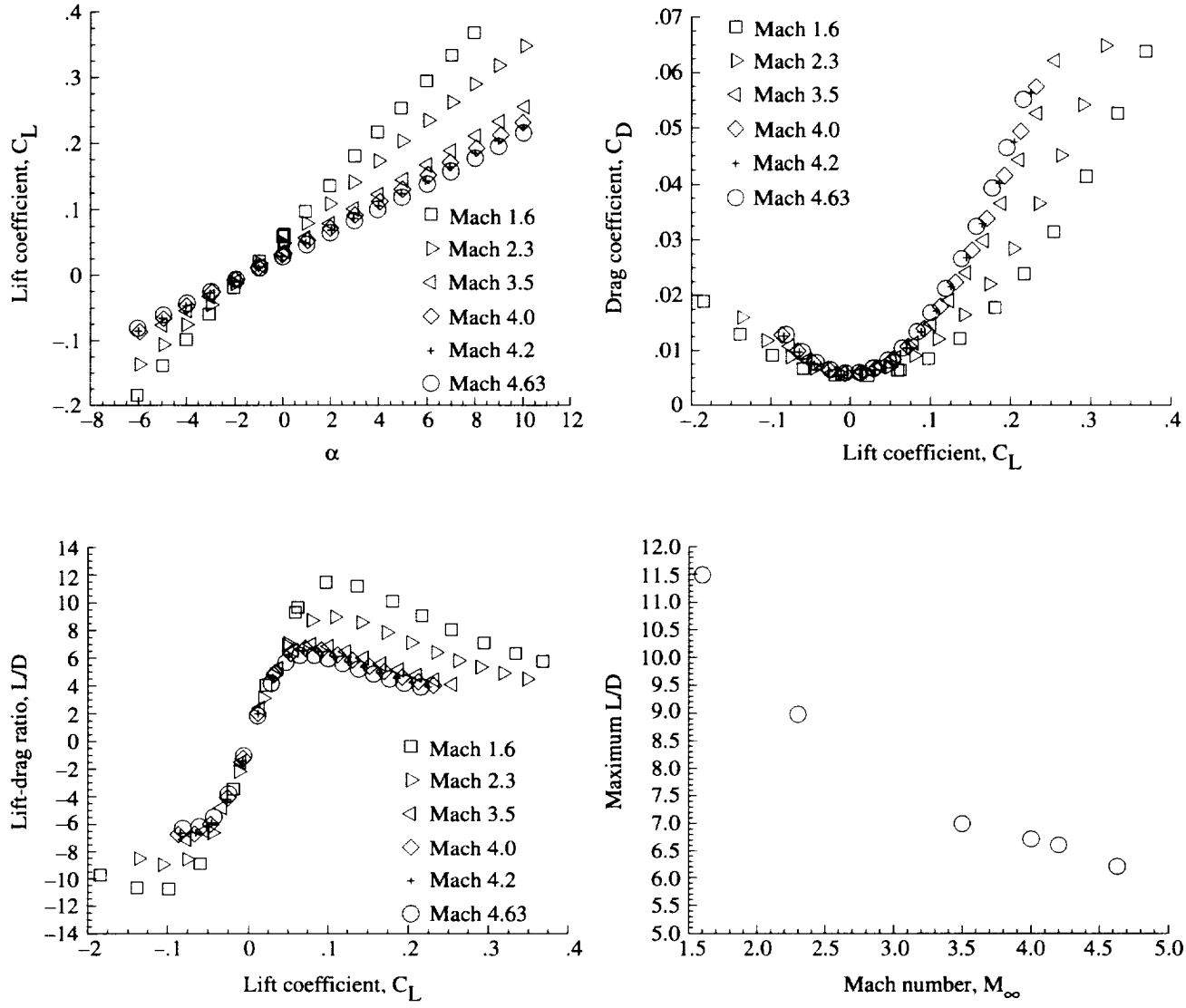

Figure 24. Aerodynamic performance of cranked-wing pure waverider configuration across Mach number range studied.

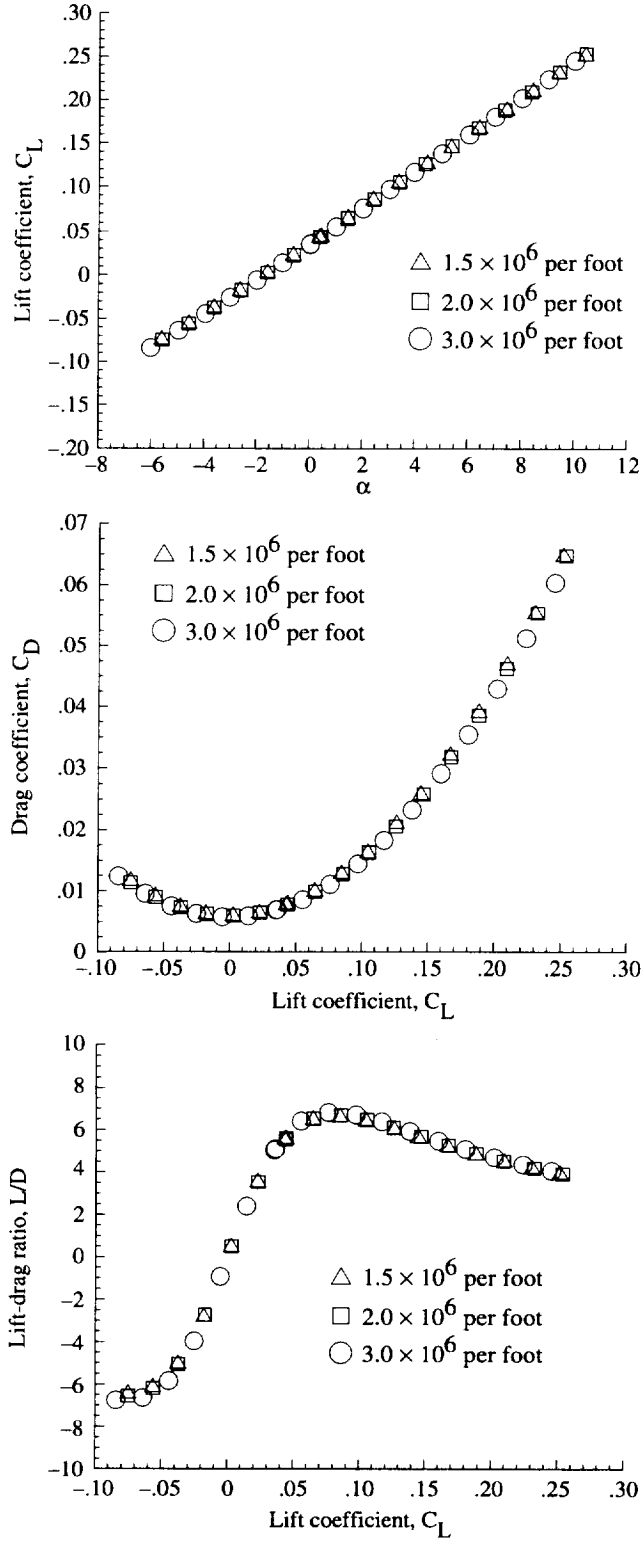

Figure 25. Effects of Reynolds number on aerodynamic performance of straight-wing pure waverider configuration at $M = 4.0$.

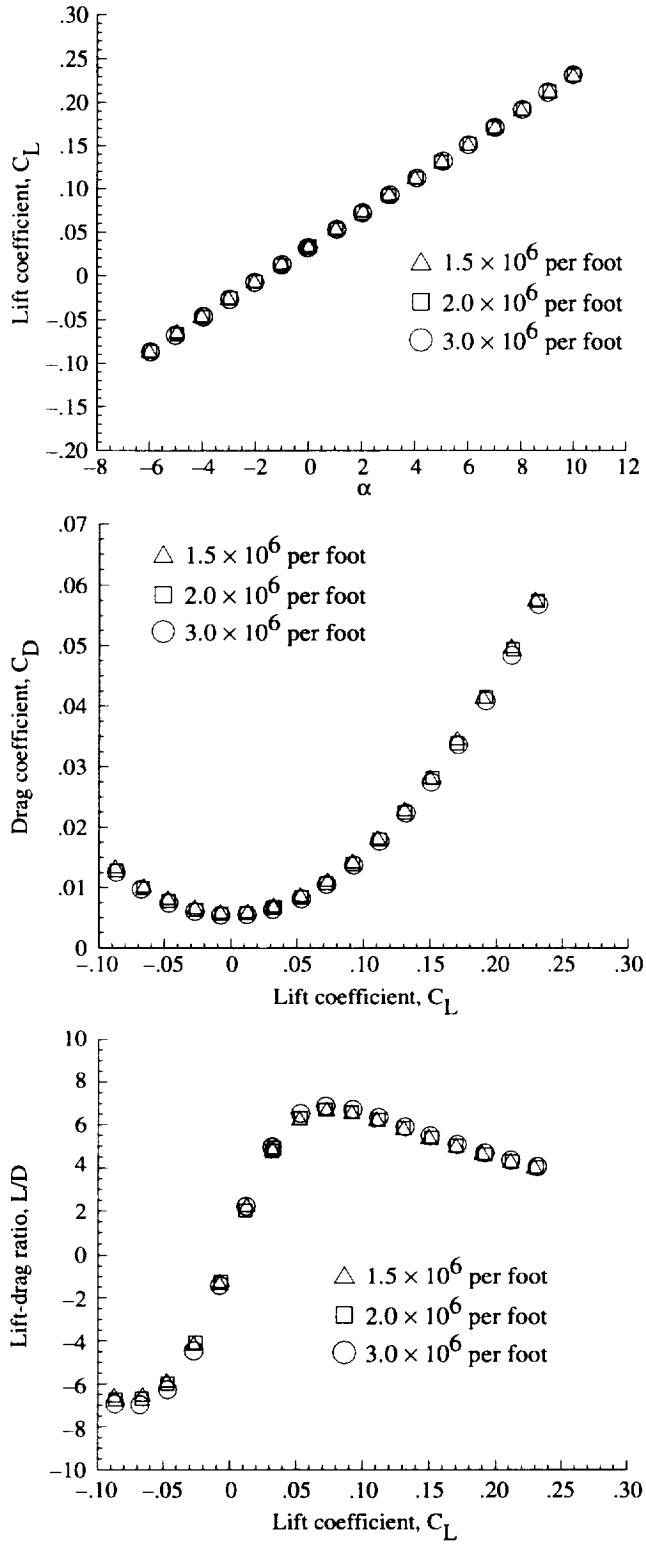

Figure 26. Effects of Reynolds number on aerodynamic performance of cranked-wing pure waverider configuration at $M = 4.0$.

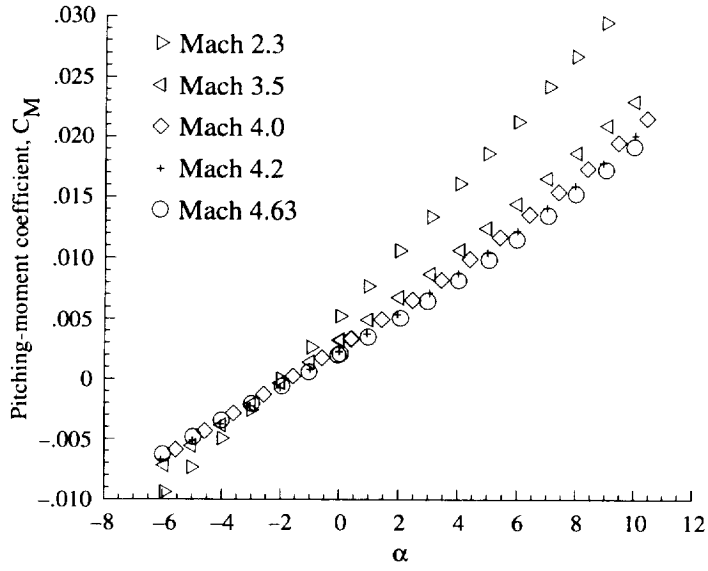

(a) Straight wing.

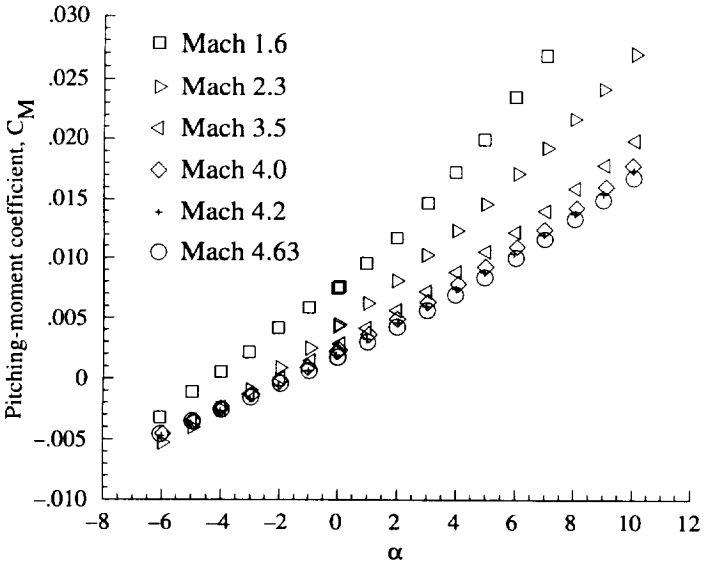

(b) Cranked wing.

Figure 27. Pitching moment characteristics of pure waverider configurations.

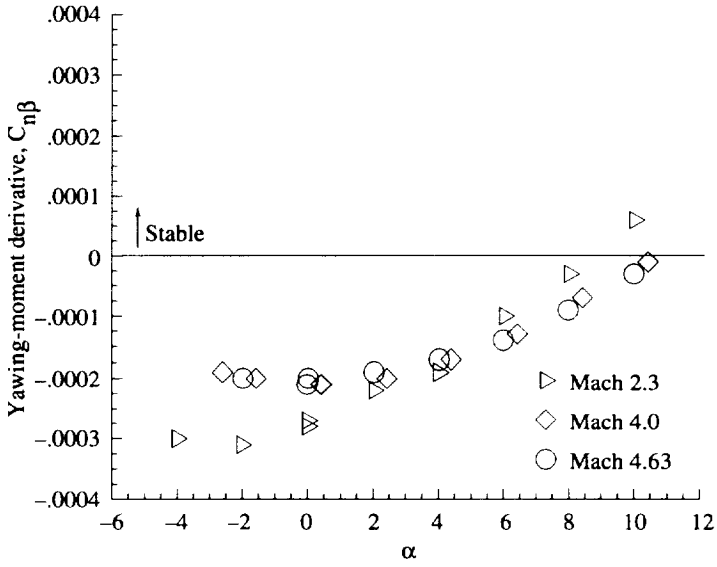

(a) Straight wing.

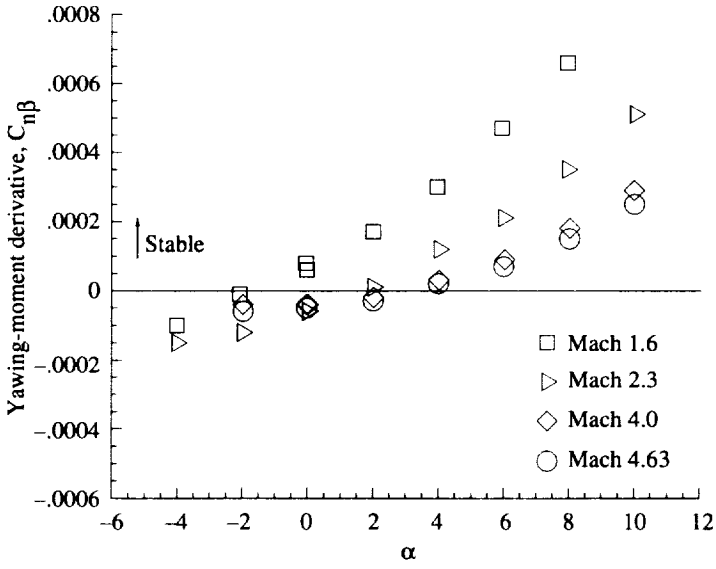

(b) Cranked wing.

Figure 28. Yawing moment characteristics of pure waverider configurations.

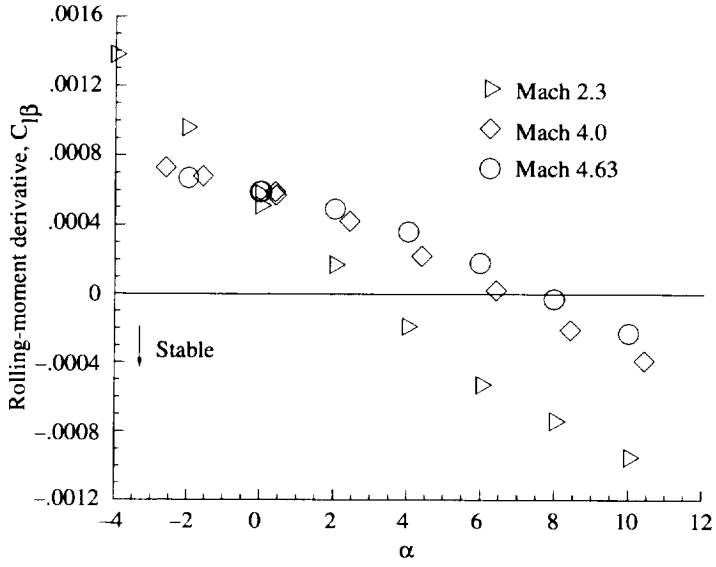

(a) Straight wing.

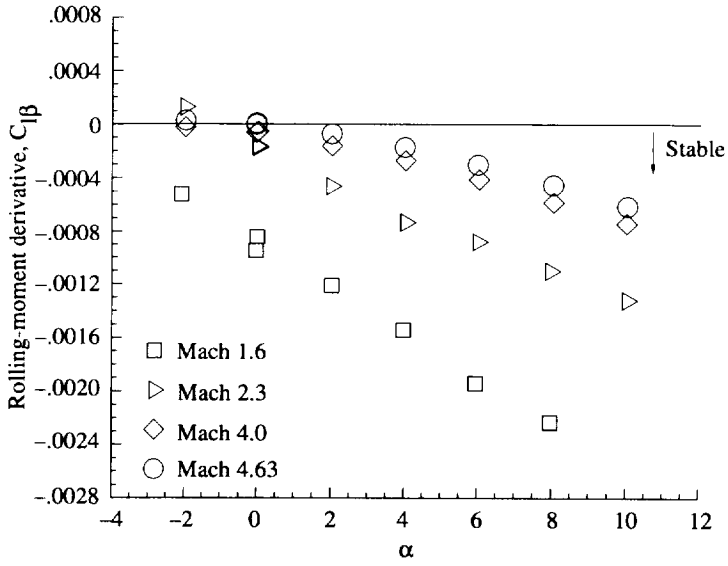

(b) Cranked wing.

Figure 29. Rolling moment characteristics of pure waverider configurations.

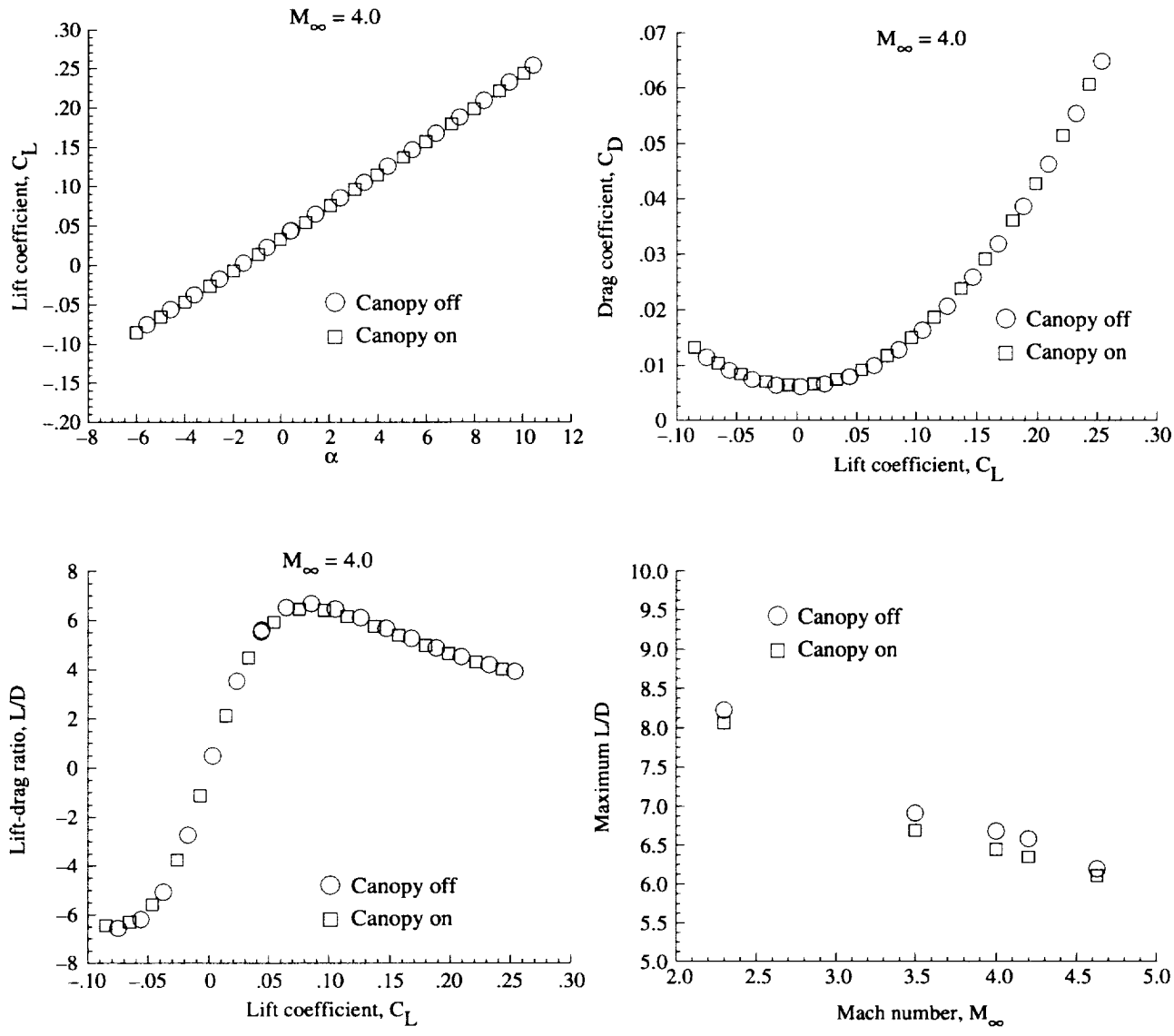

Figure 30. Effect of canopy on aerodynamic performance of straight-wing pure waverider configuration.

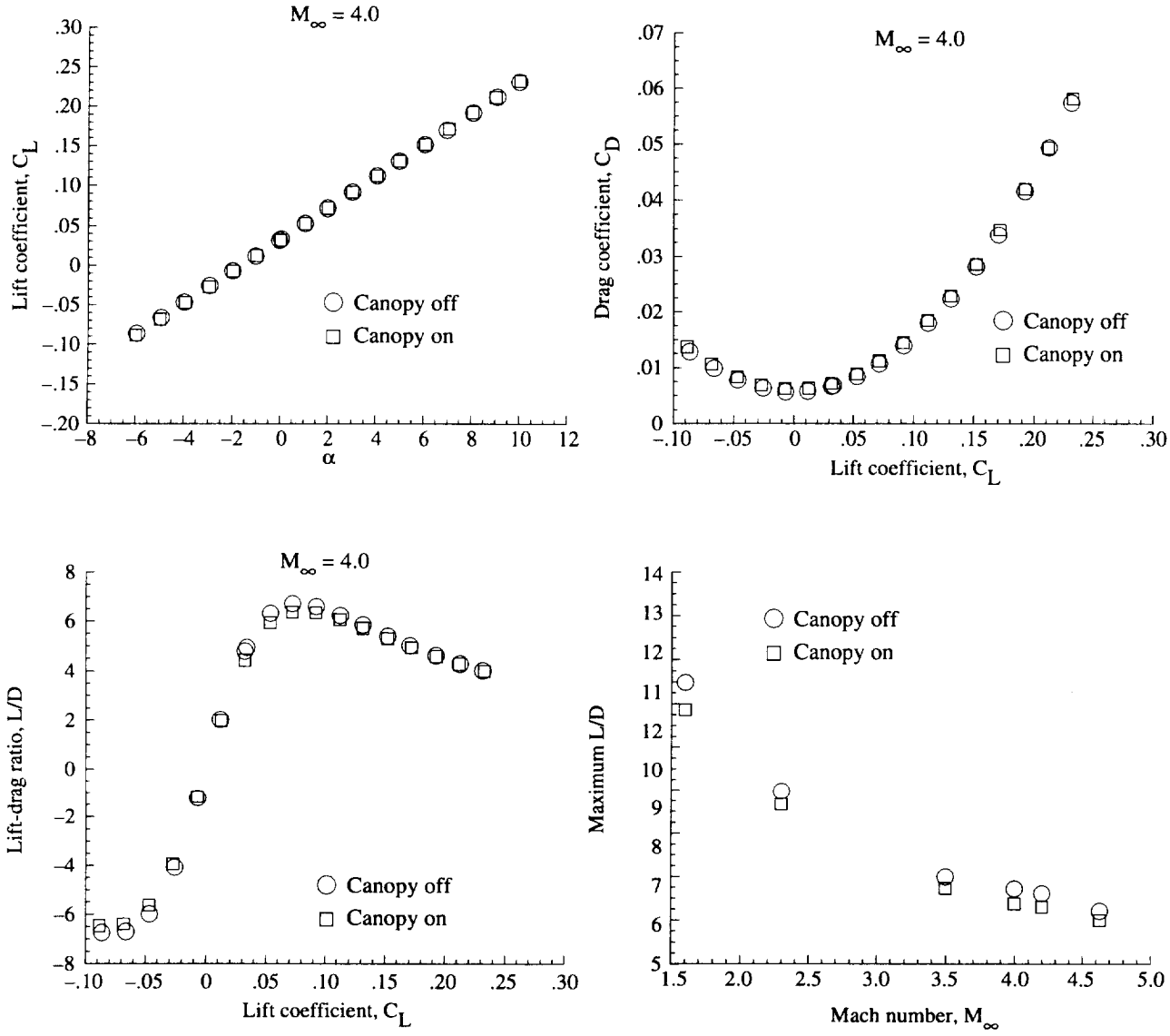

Figure 31. Effect of canopy on aerodynamic performance of cranked-wing pure waverider configuration.

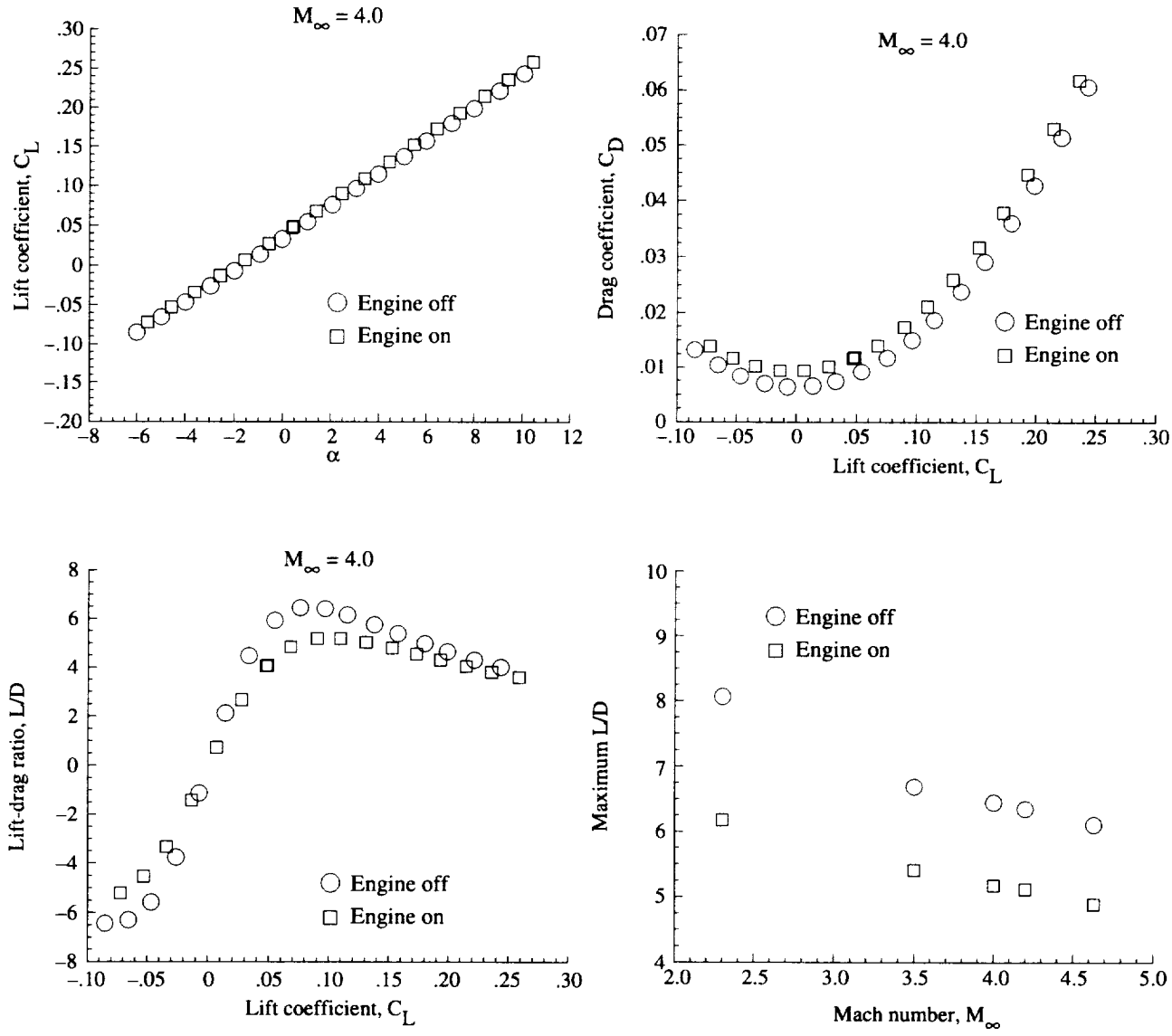

Figure 32. Effect of adding engine package on aerodynamics of straight-wing pure waverider model with canopy.

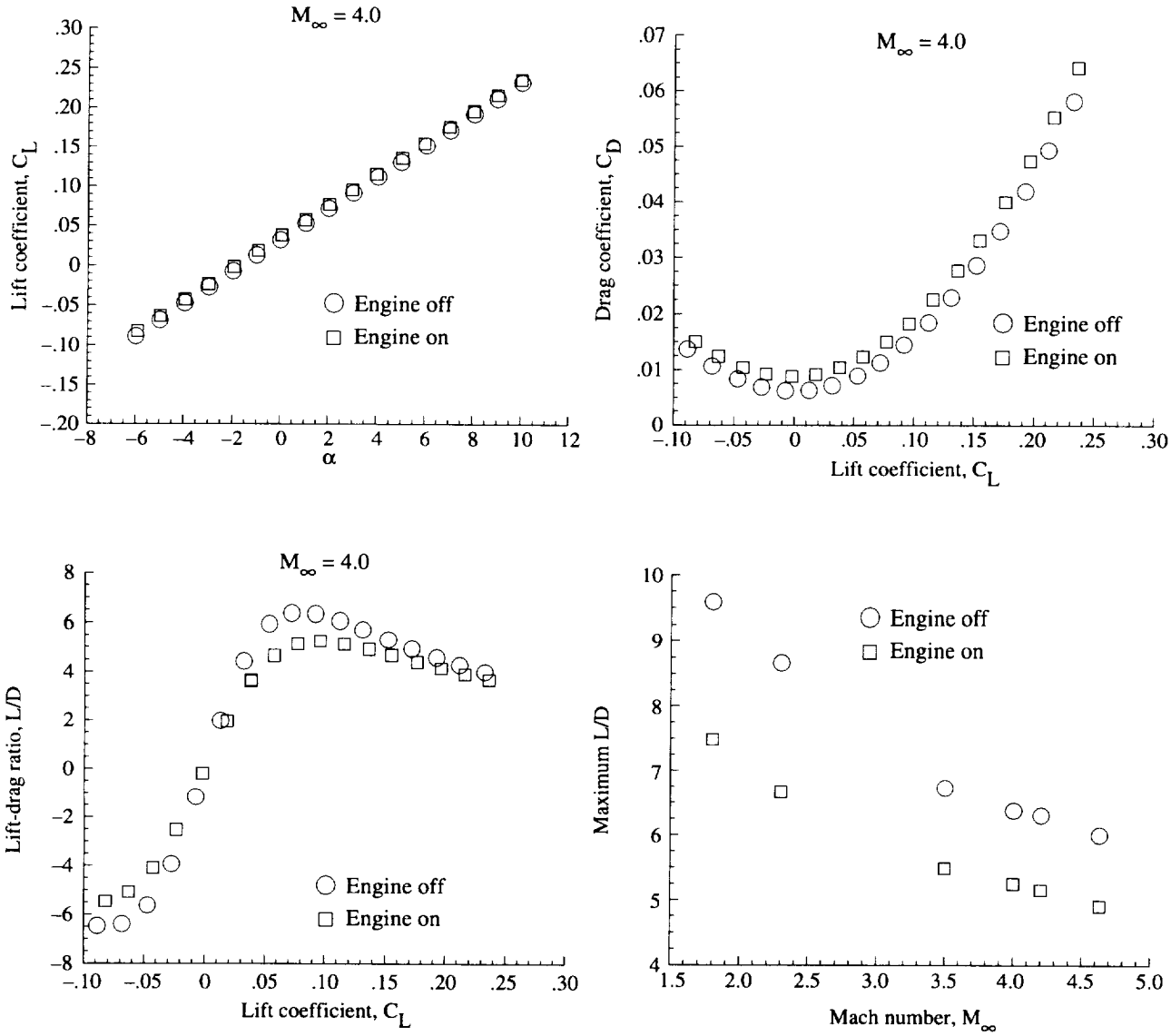

Figure 33. Effect of adding engine package on aerodynamics of cranked-wing pure waverider model with canopy.

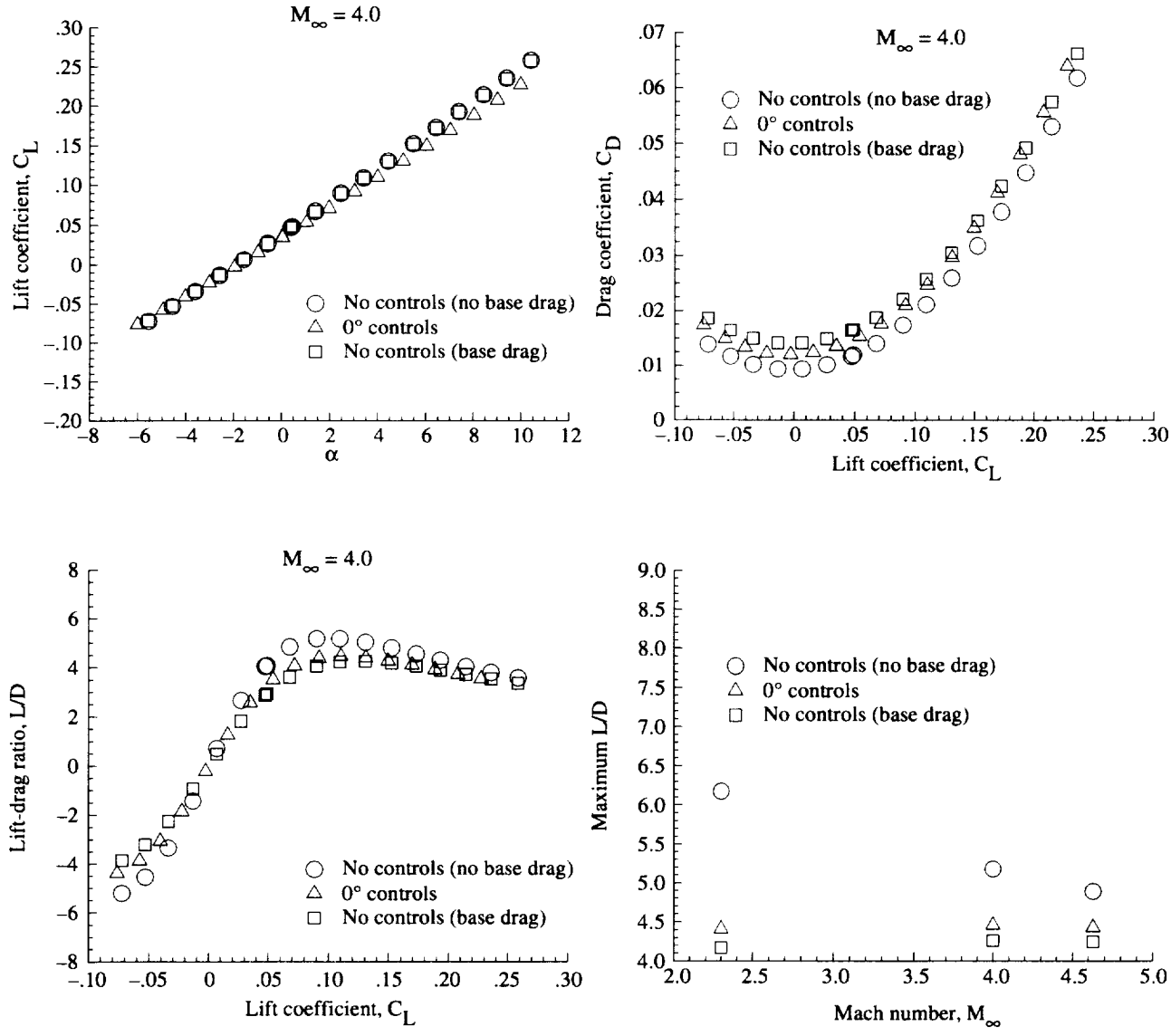

Figure 34. Effect of undeflected control surface addition on aerodynamics of straight-wing pure waverider configuration with canopy and engine package attached.

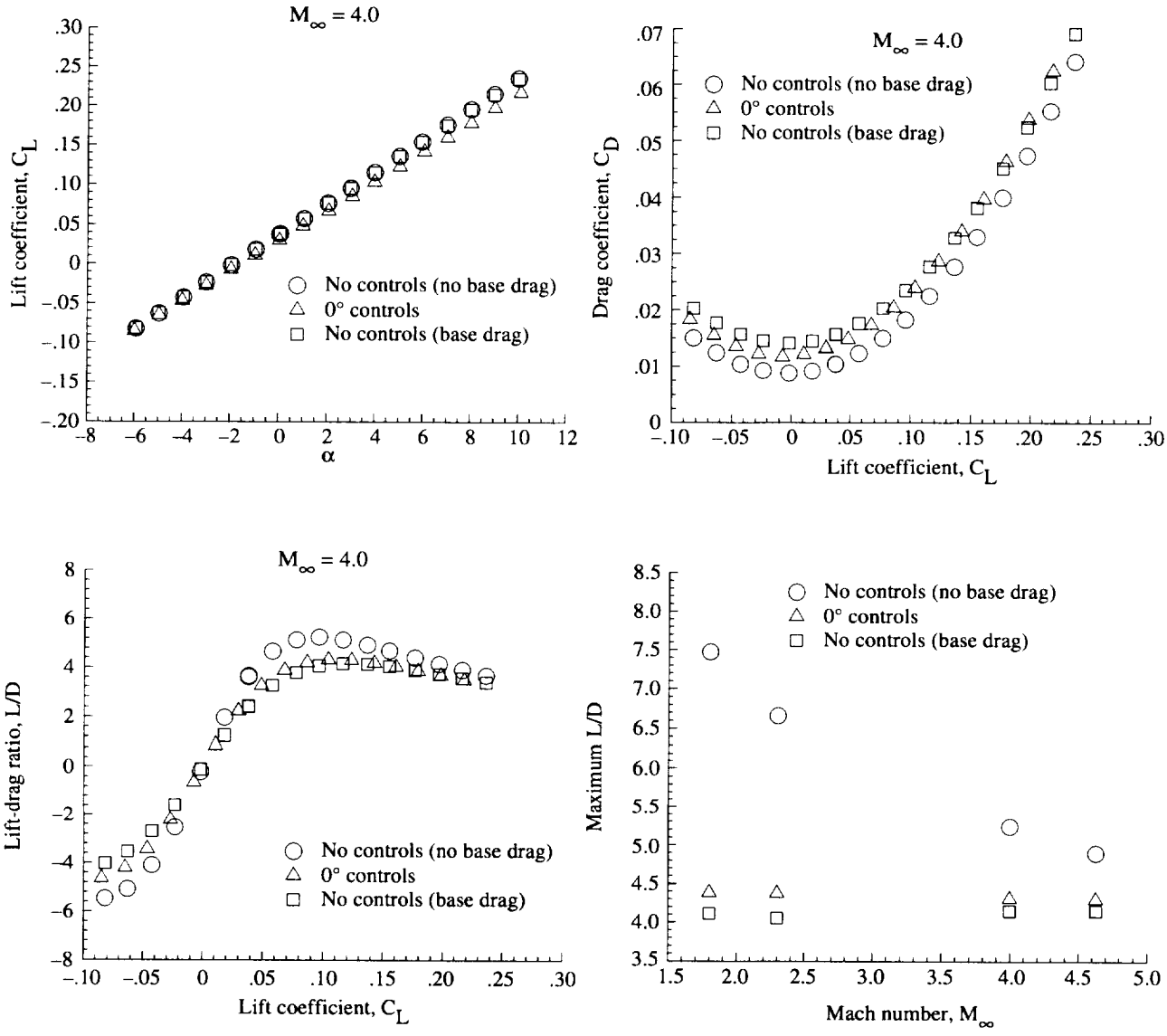

Figure 35. Effect of undeflected control surface addition on aerodynamics of cranked-wing pure waverider configuration with canopy and engine package attached.

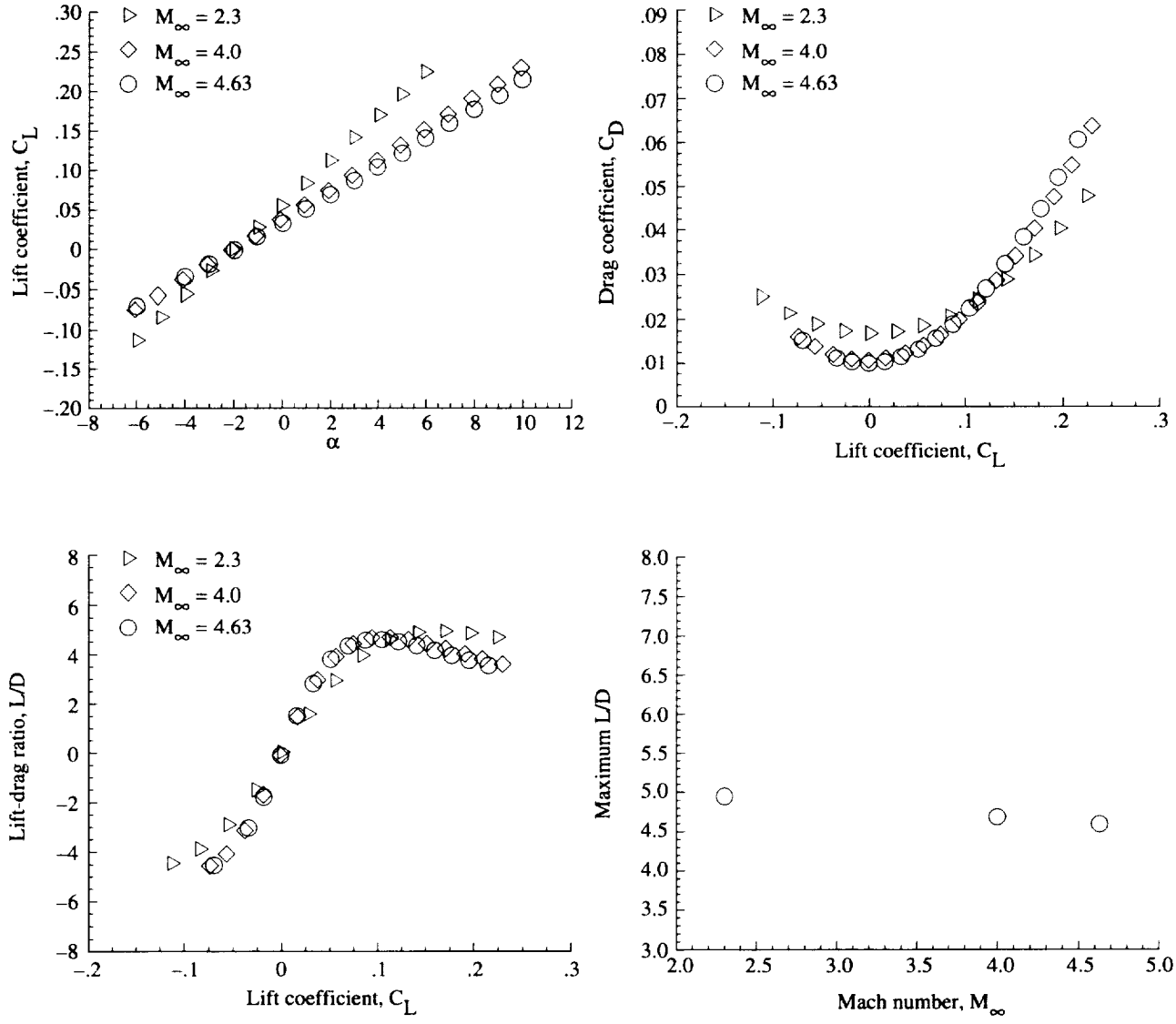

Figure 36. Aerodynamics of fully integrated straight-wing configuration.

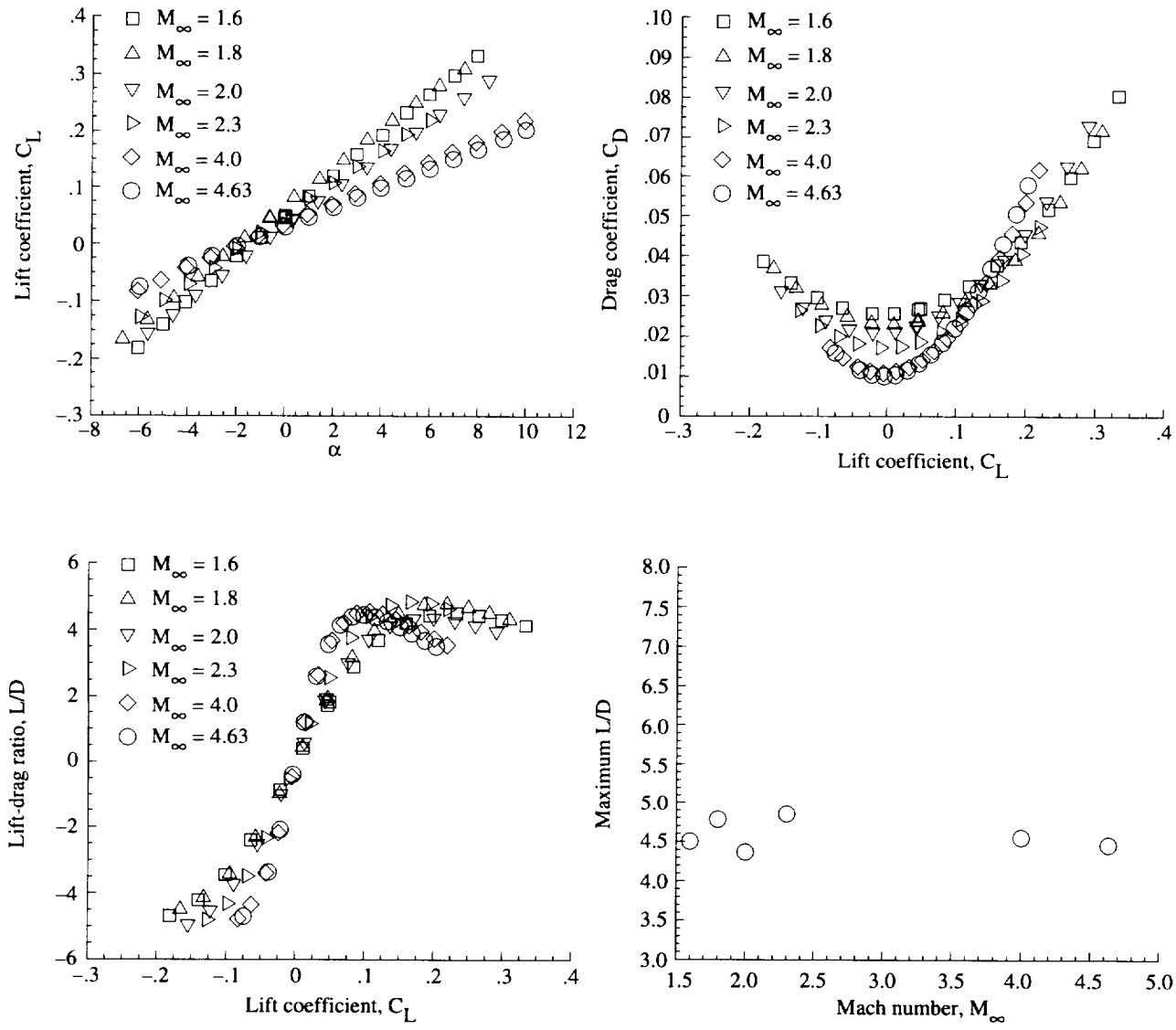

Figure 37. Aerodynamics of fully integrated cranked-wing configuration.

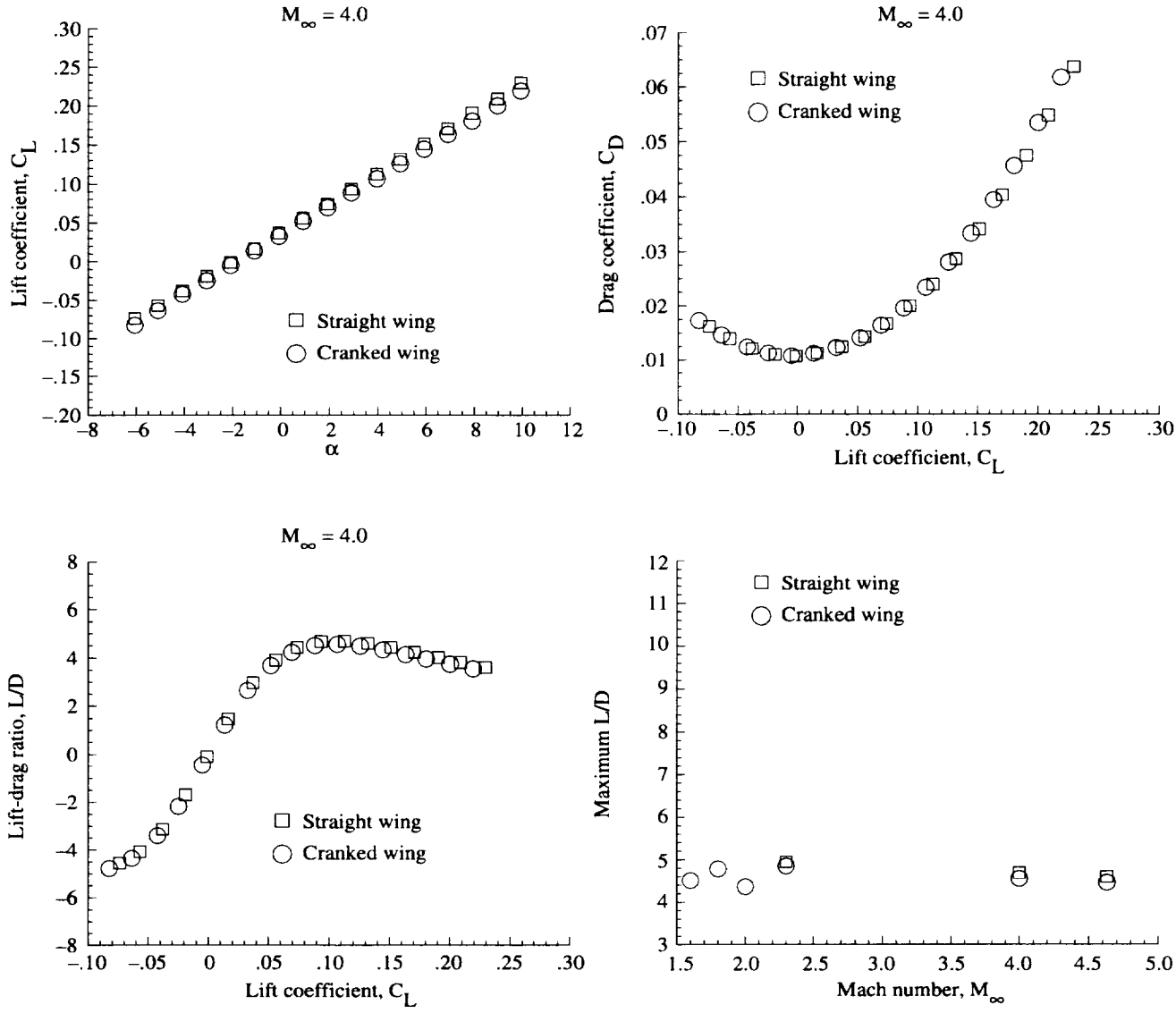

Figure 38. Comparison of aerodynamics of straight-wing and cranked-wing fully integrated configurations.

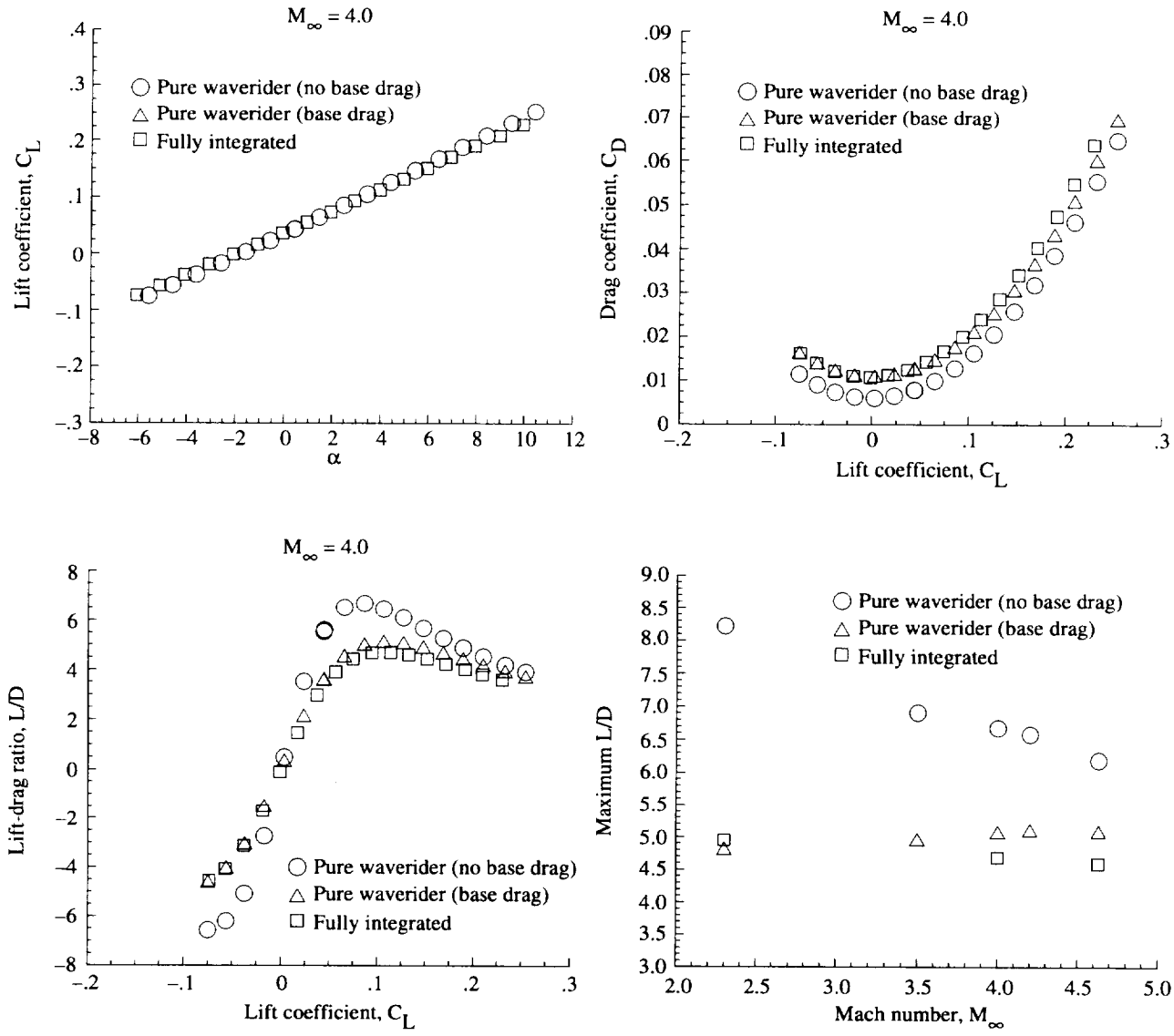

Figure 39. Comparison of aerodynamic performance of straight-wing fully integrated and straight-wing pure waverider configurations.

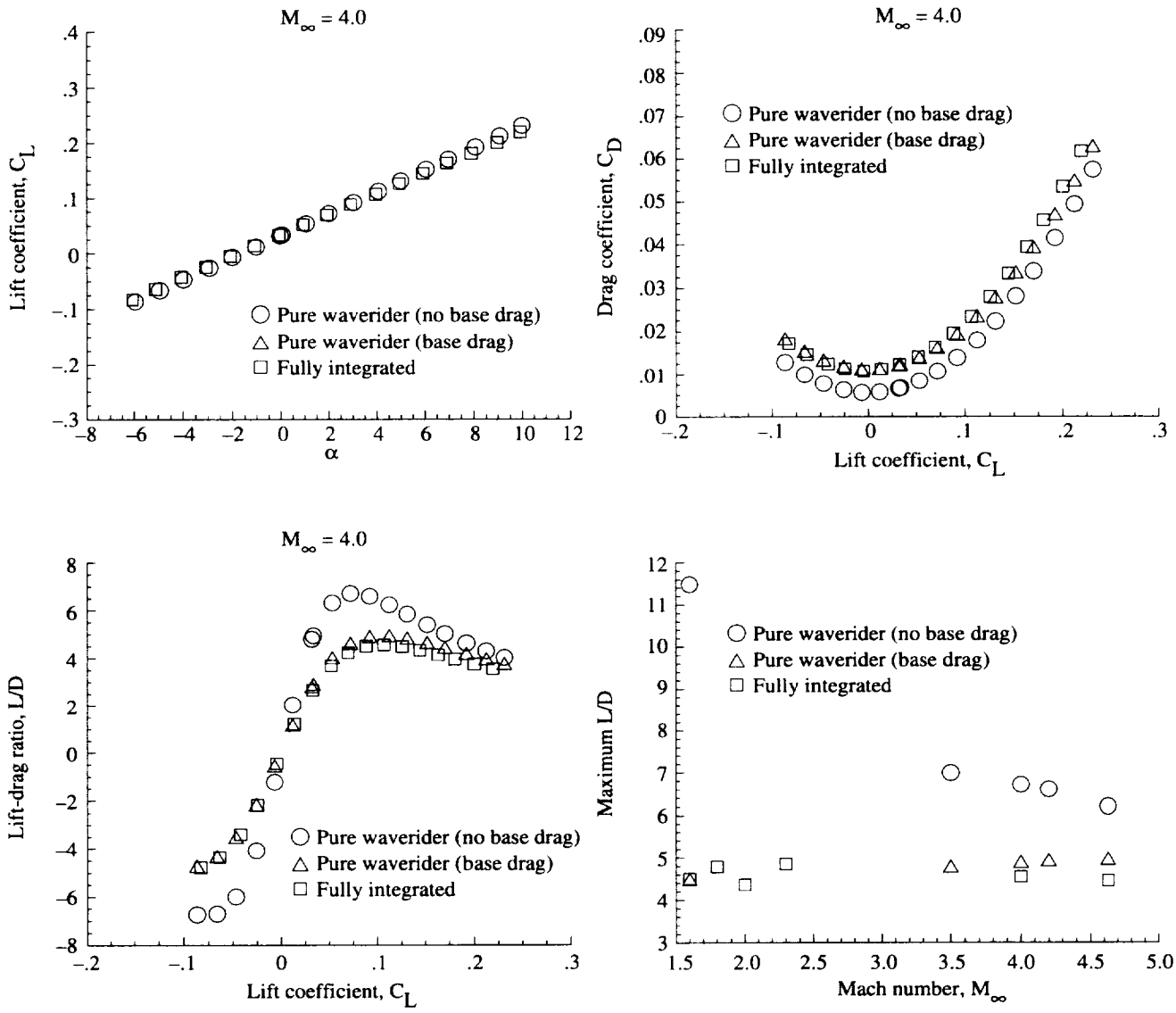

Figure 40. Comparison of aerodynamic performance of cranked-wing fully integrated and cranked-wing pure waverider configurations.

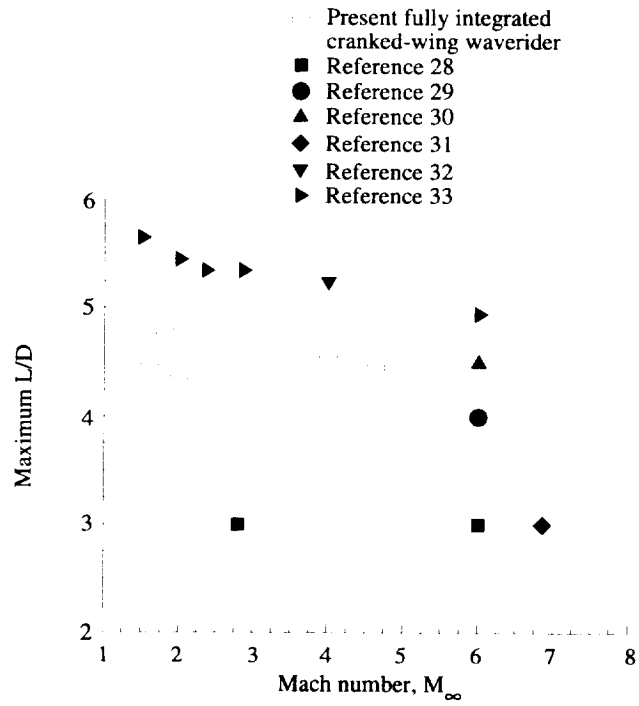

Figure 41. Assessment of aerodynamic performance of waverider-derived vehicle.

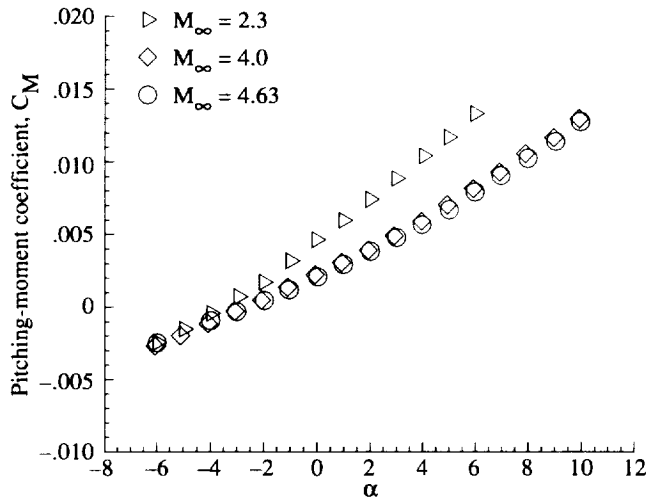

(a) Straight wing.

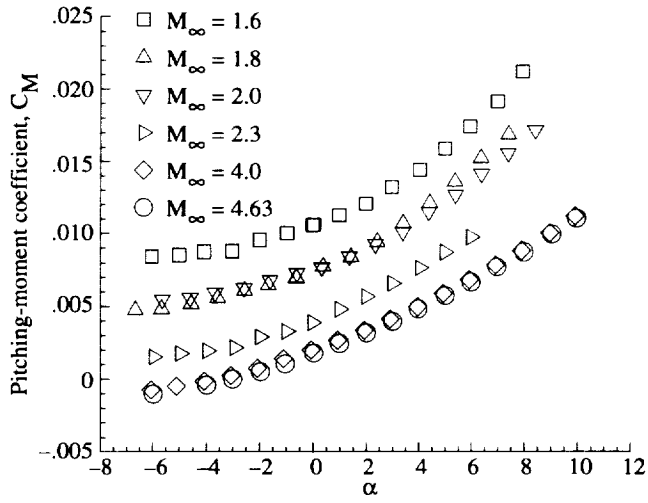

(b) Cranked wing.

Figure 42. Longitudinal stability of each fully integrated waverider-derived configuration with undeflected elevons and ailerons.

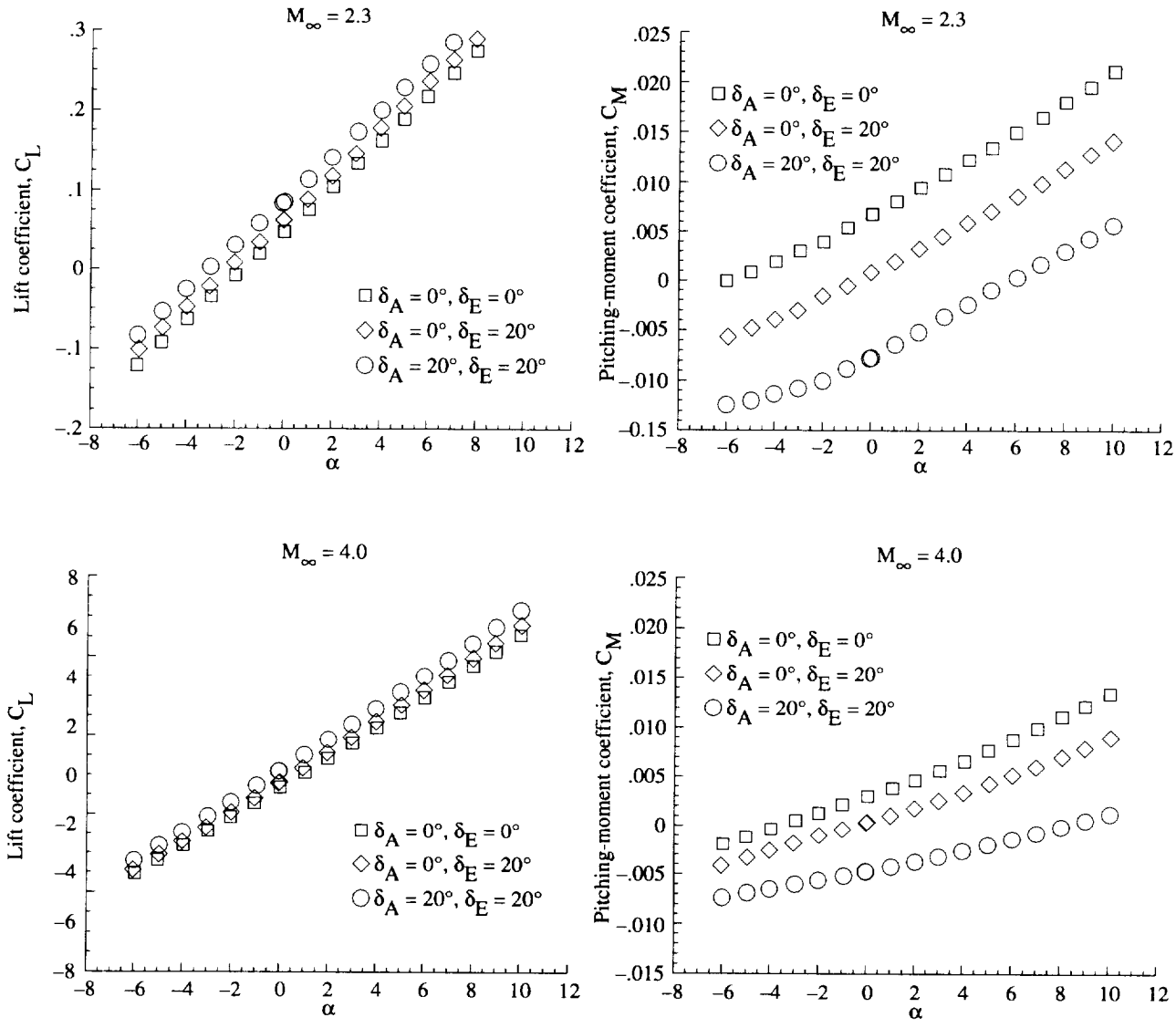

(a) $M_\infty = 2.3$ and 4.0.

Figure 43. Pitch control effectiveness of elevons and elevon/aileron combination for straight-wing fully integrated configuration.

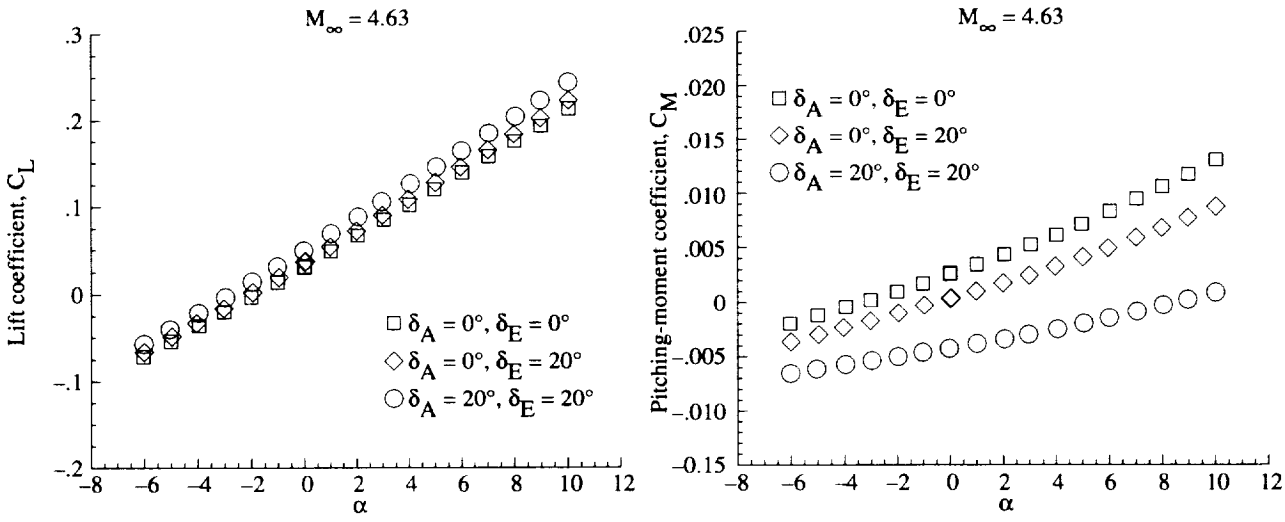

(b) $M_\infty = 4.63$.

Figure 43. Concluded.

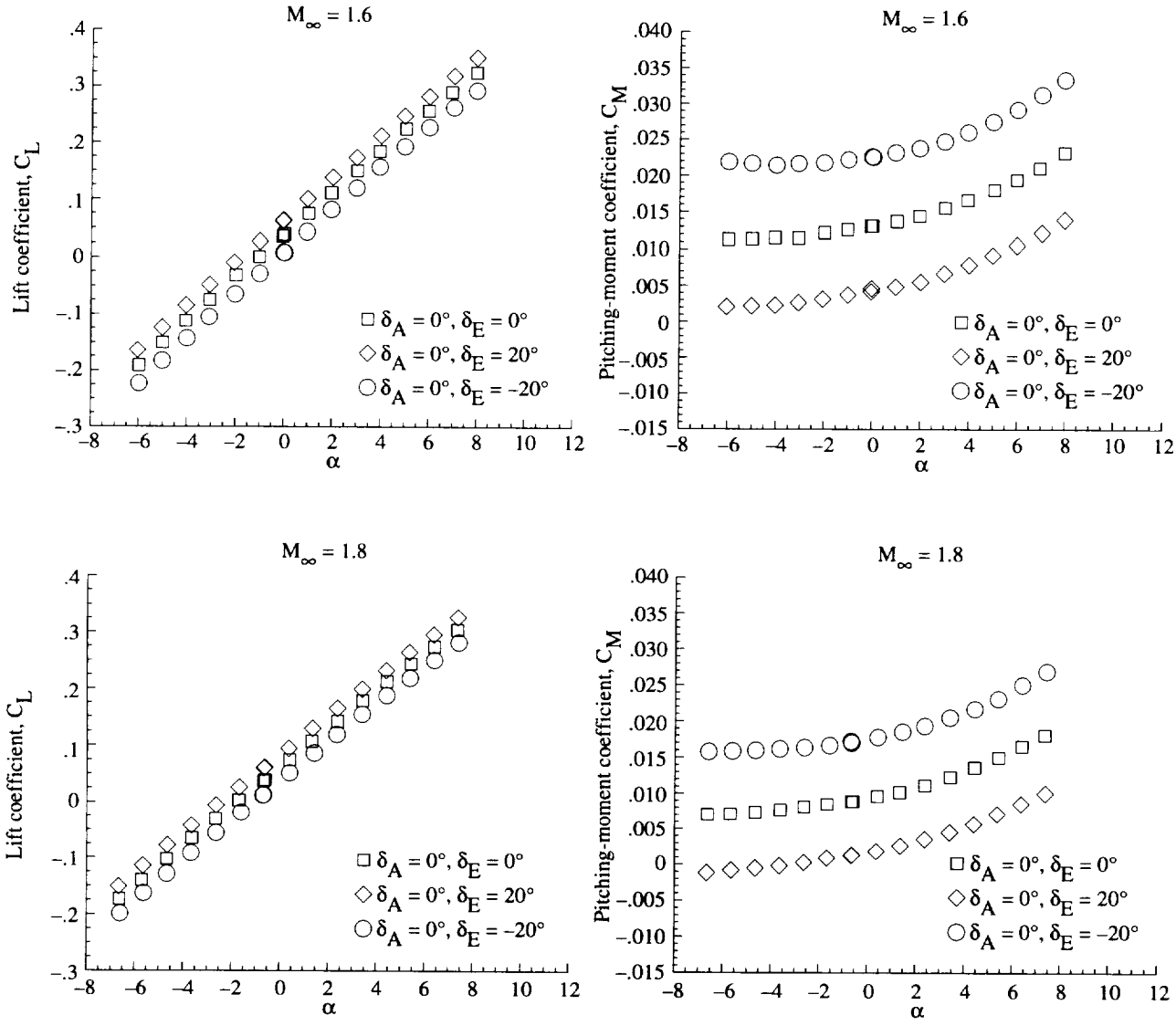

(a) $M_\infty = 1.6$ and 1.8.

Figure 44. Pitch control effectiveness of elevons for cranked-wing fully integrated configuration.

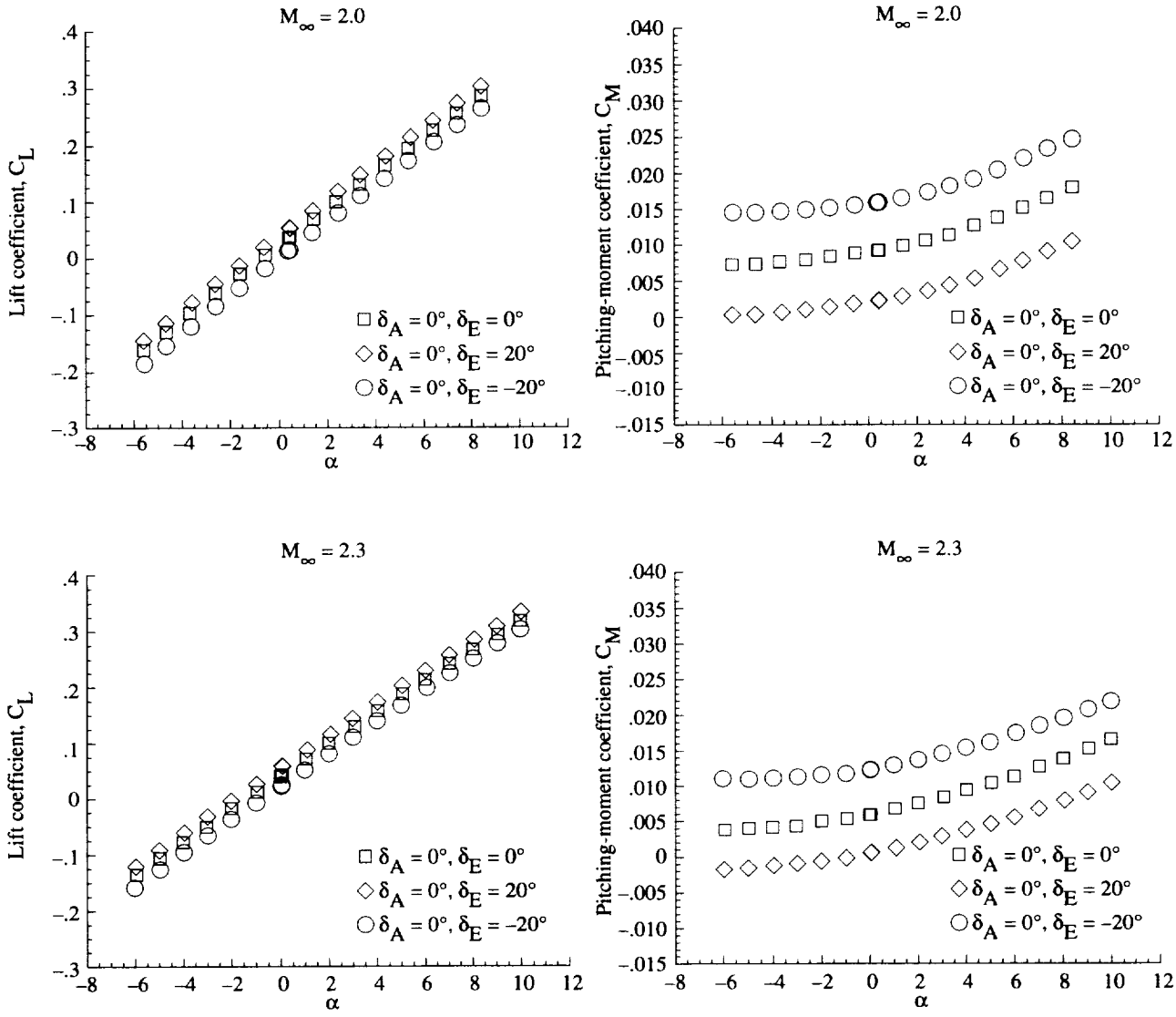

(b) M_∞ = 2.0 and 2.3.

Figure 44. Continued.

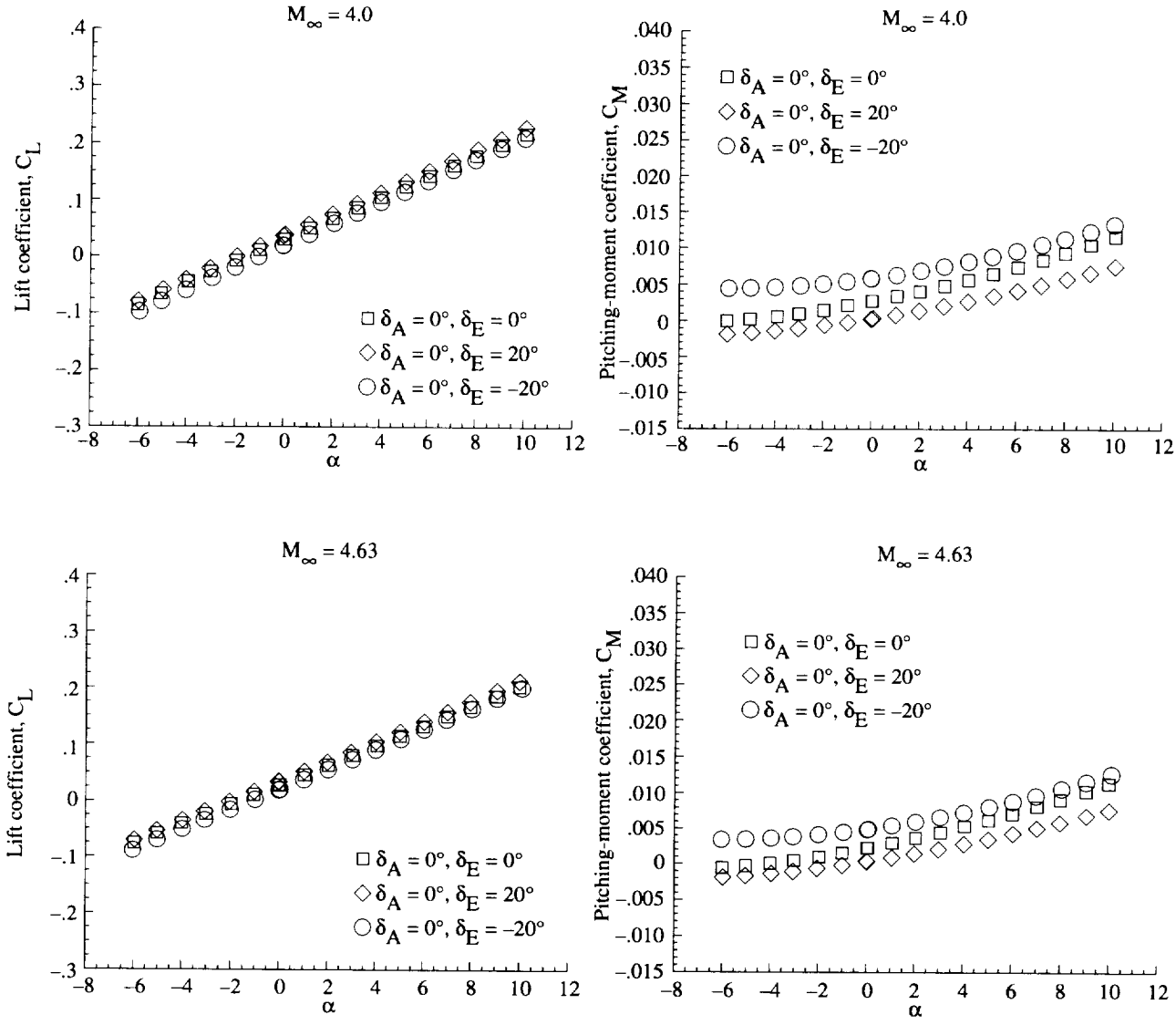

(c) M_∞ = 4.0 and 4.63.

Figure 44. Concluded.

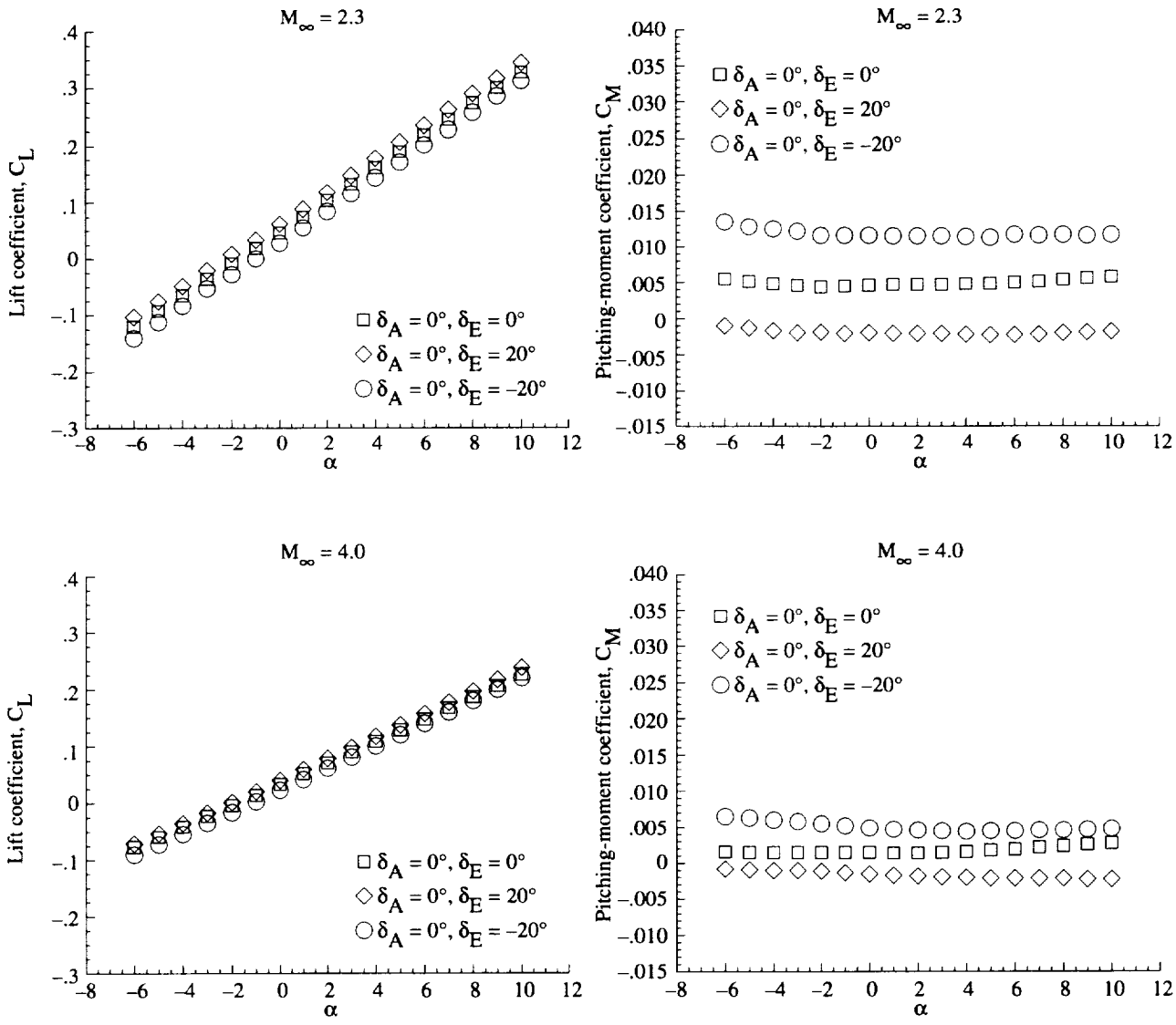

(a) $M_\infty = 2.3$ and 4.0.

Figure 45. Pitch control effectiveness of elevons for straight-wing fully integrated configuration with moment reference center at 58 percent of body length.

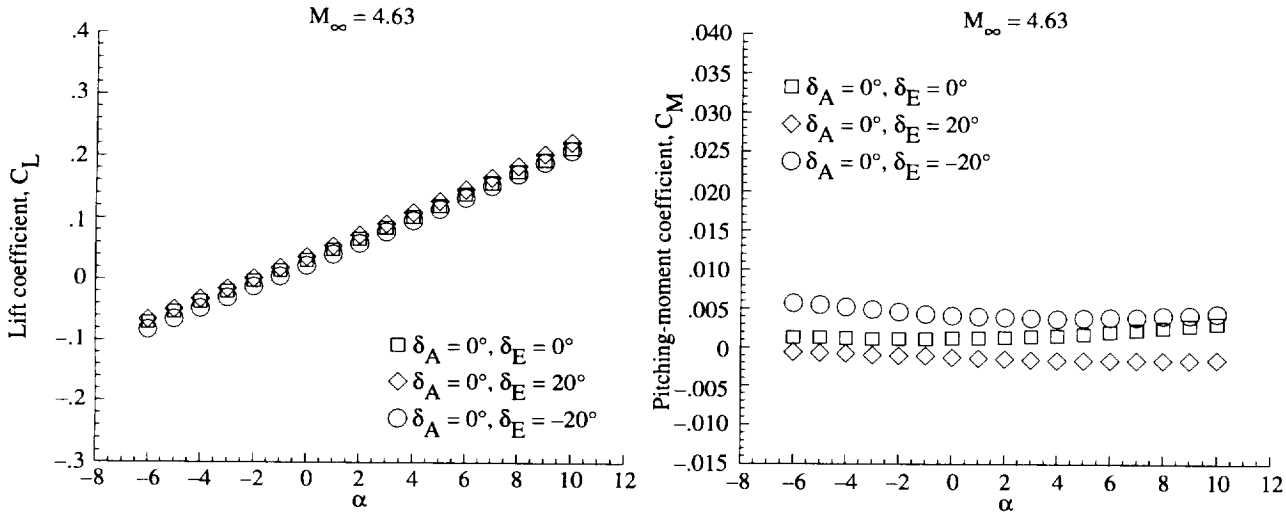

(b) $M_\infty = 4.63$.

Figure 45. Concluded.

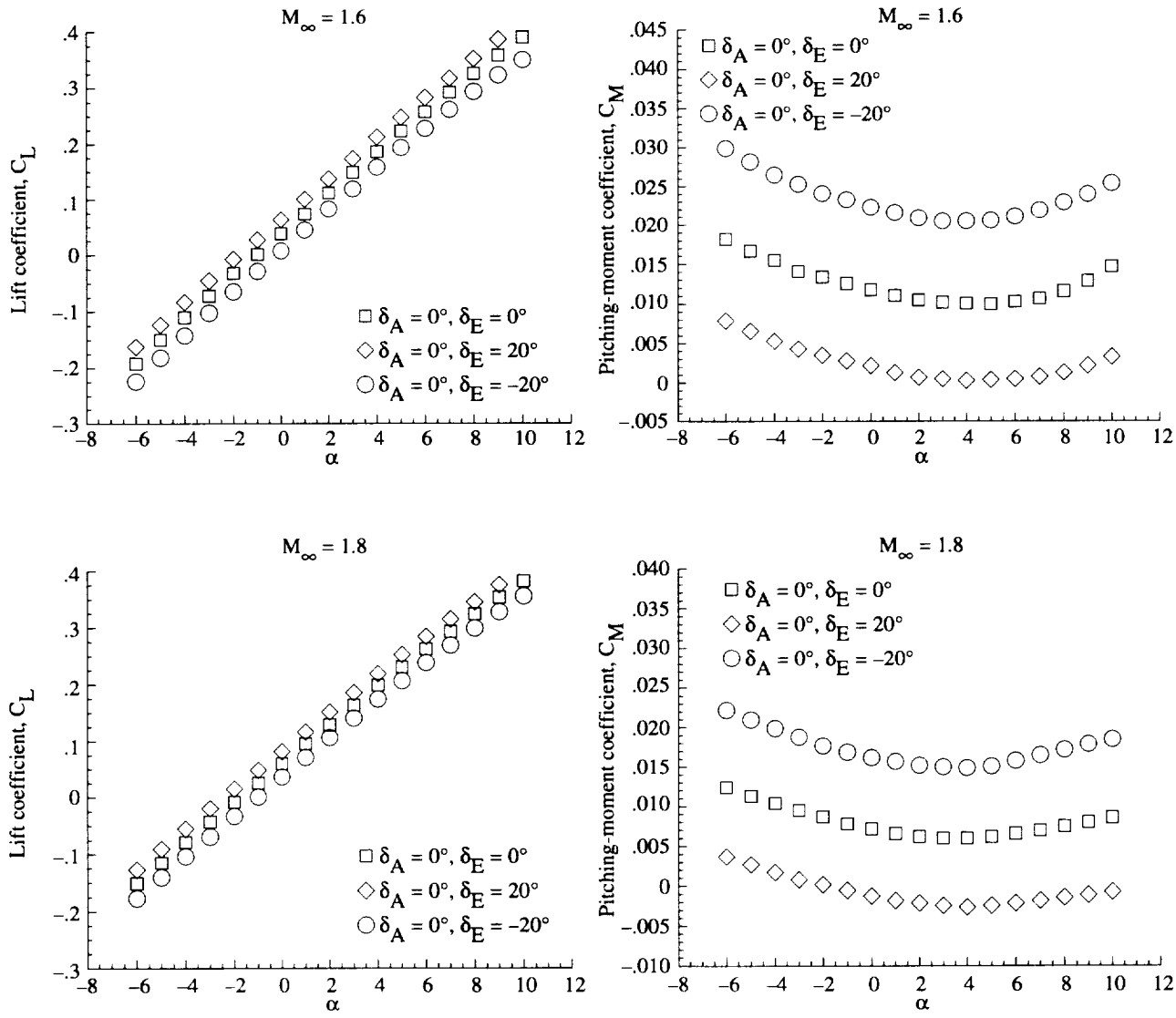

(a) M_∞ = 1.6 and 1.8.

Figure 46. Pitch control effectiveness of elevons for cranked-wing fully integrated configuration with moment reference center at 59 percent of body length.

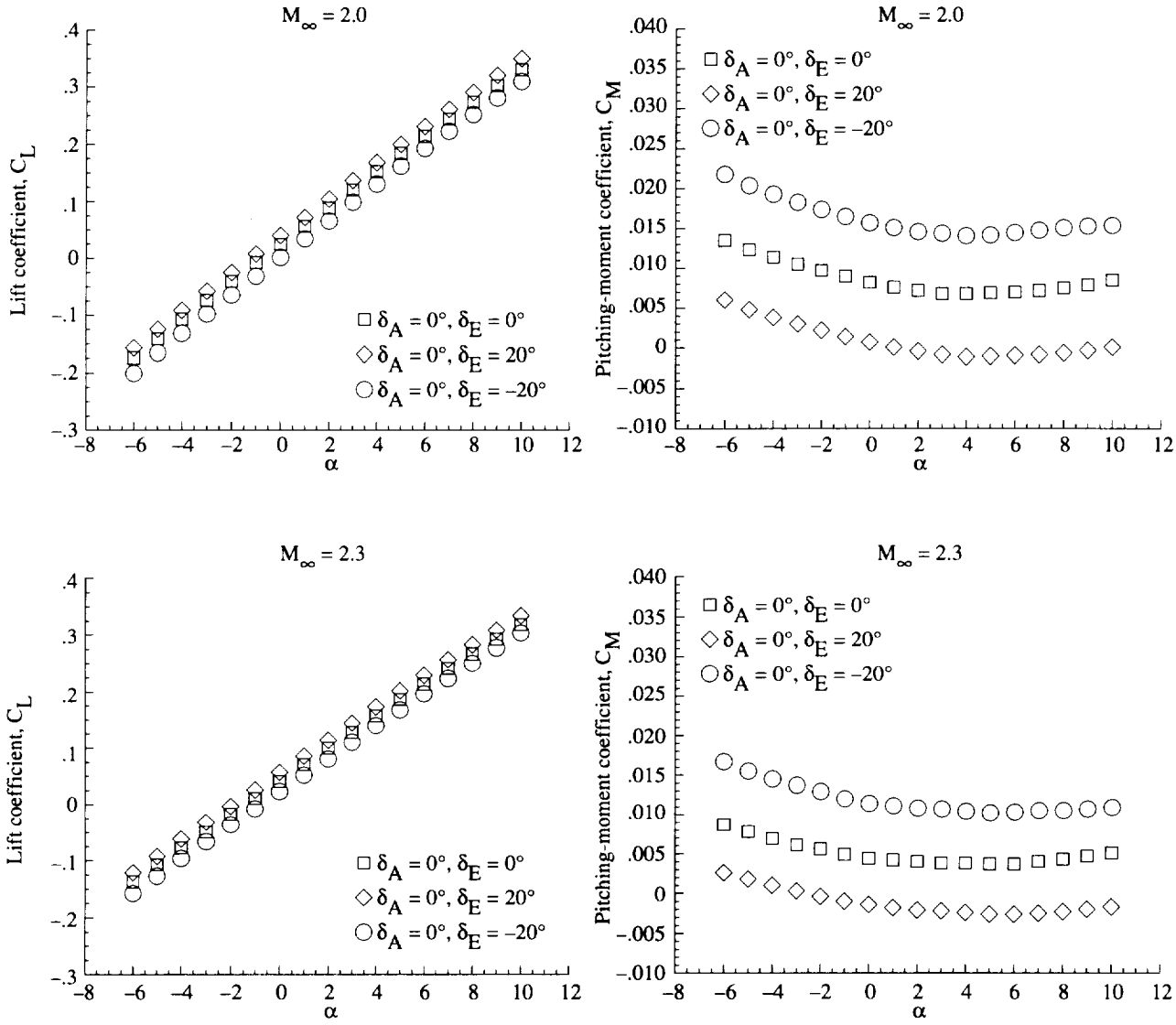

(b) M_∞ = 2.0 and 2.3.

Figure 46. Continued.

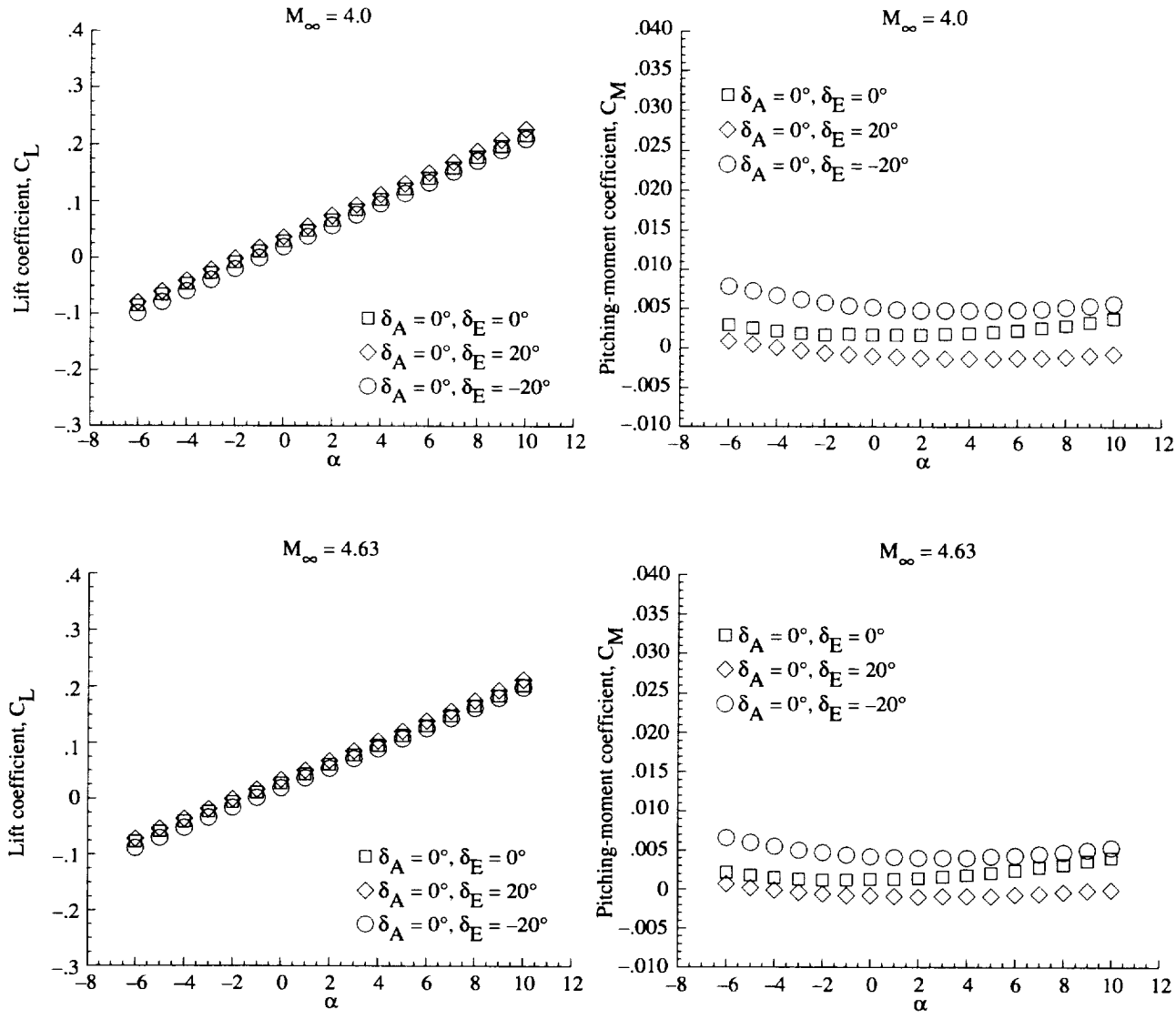

(c) $M_\infty = 4.0$ and 4.63.

Figure 46. Concluded.

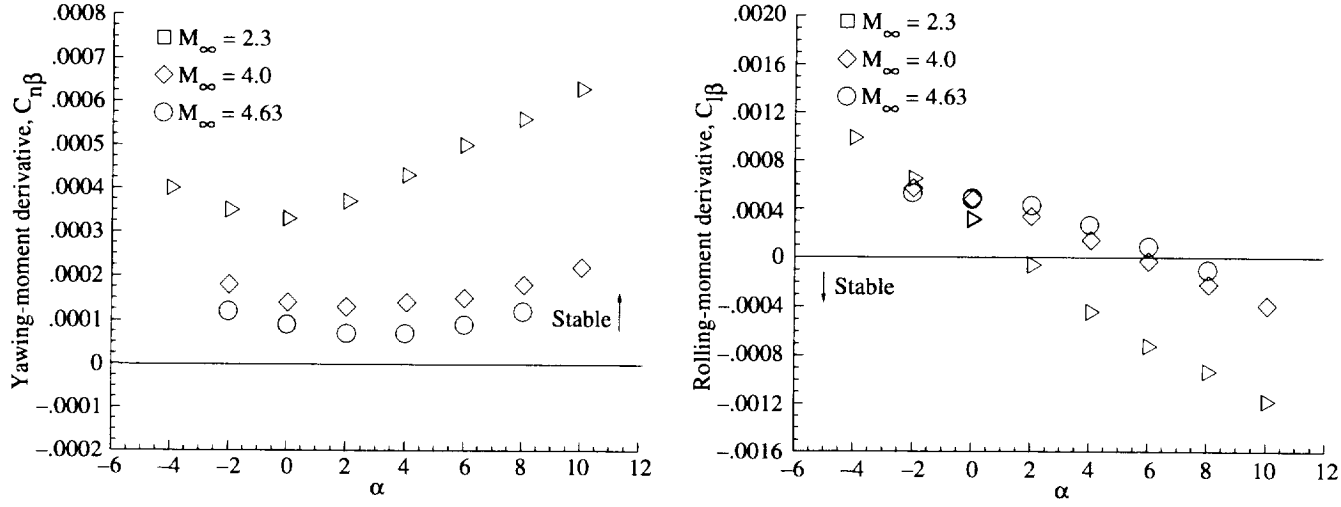

Figure 47. Lateral-directional stability of straight-wing fully integrated configuration.

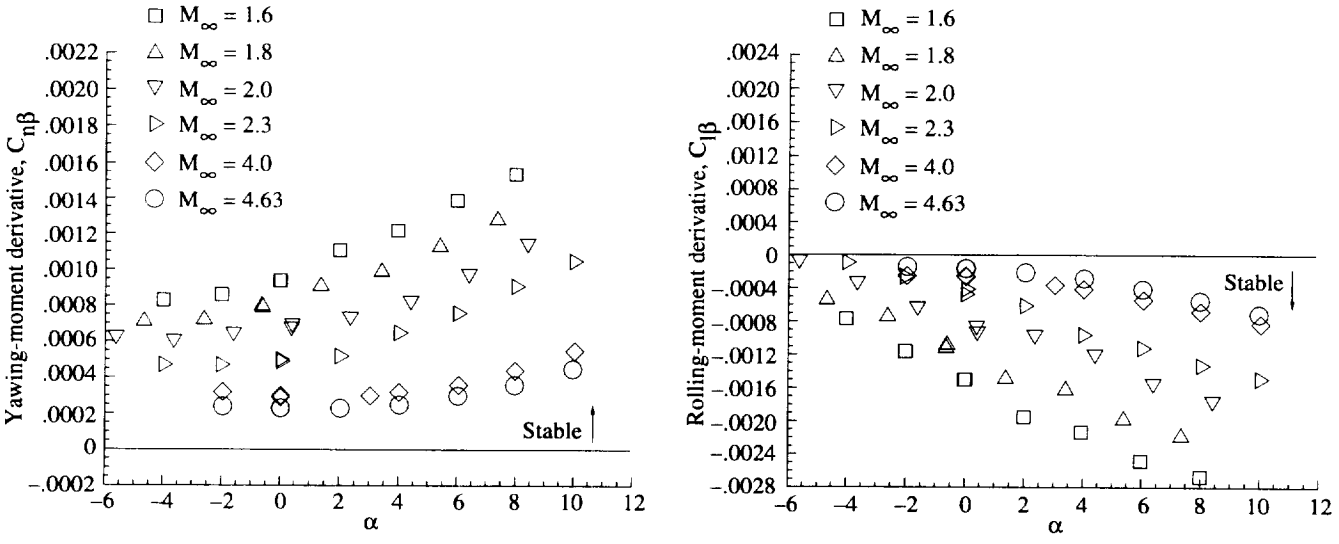

Figure 48. Lateral-directional stability of cranked-wing fully integrated configuration.

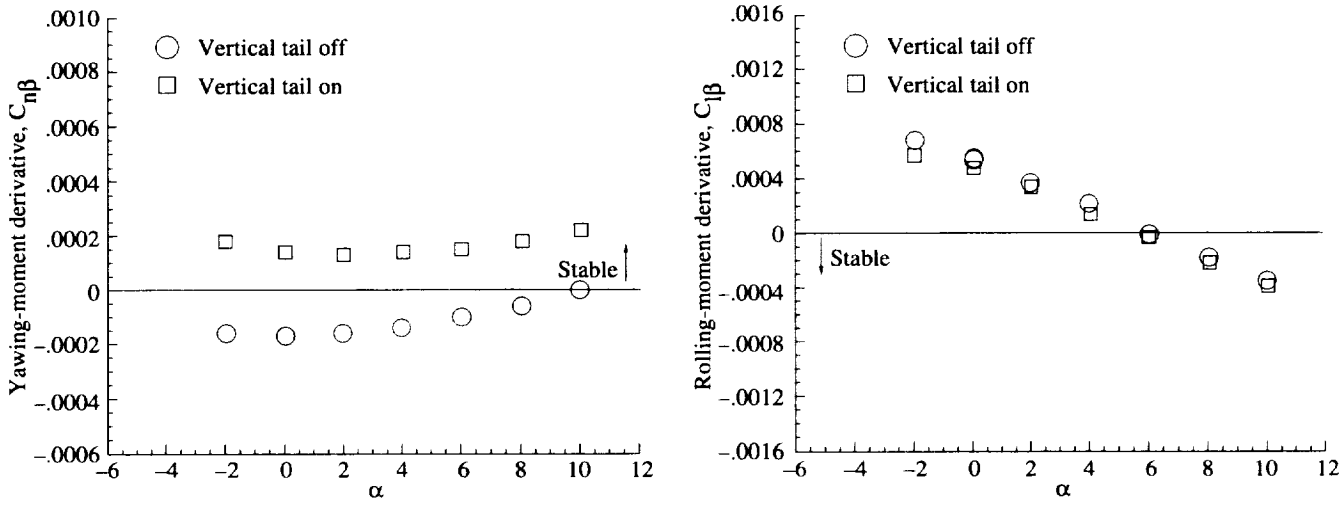

Figure 49. Effects of vertical tail on lateral-directional stability of straight-wing fully integrated configuration at $M_\infty = 4.0$.

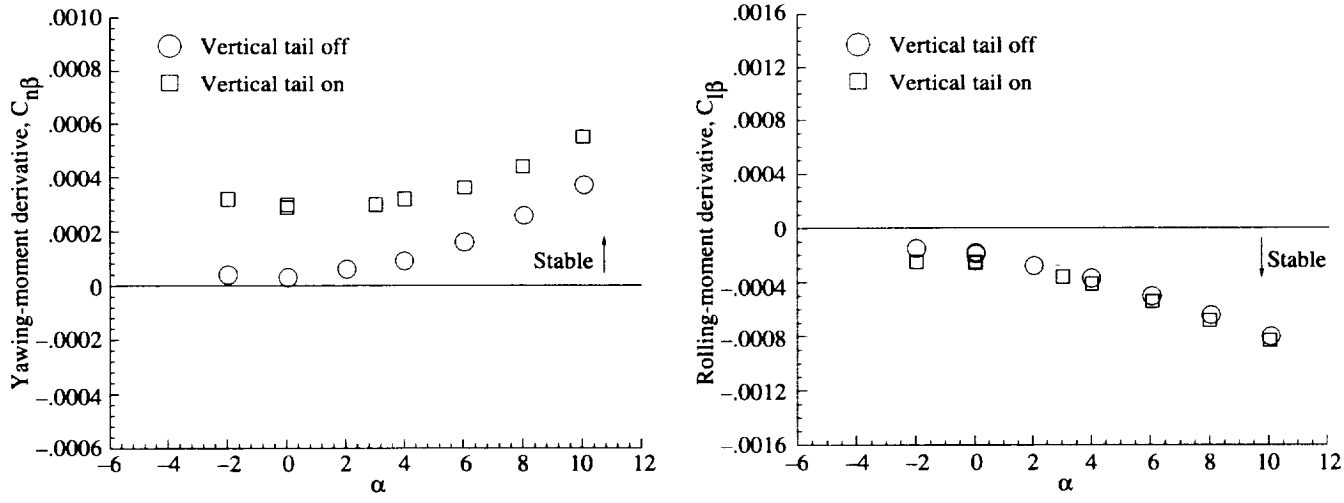

Figure 50. Effects of vertical tail on lateral-directional stability of cranked-wing fully integrated configuration at $M_\infty = 4.0$.

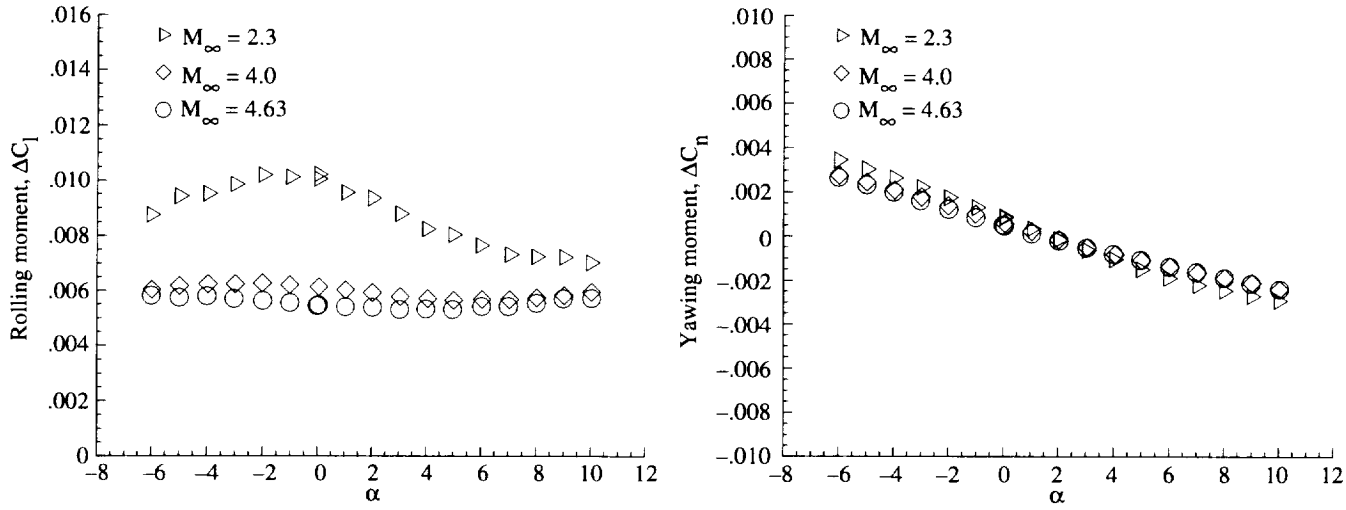

Figure 51. Aileron effectiveness on lateral-directional stability of straight-wing fully integrated configuration; $\delta_A = \pm 20°$ and $\delta_E = 0°$.

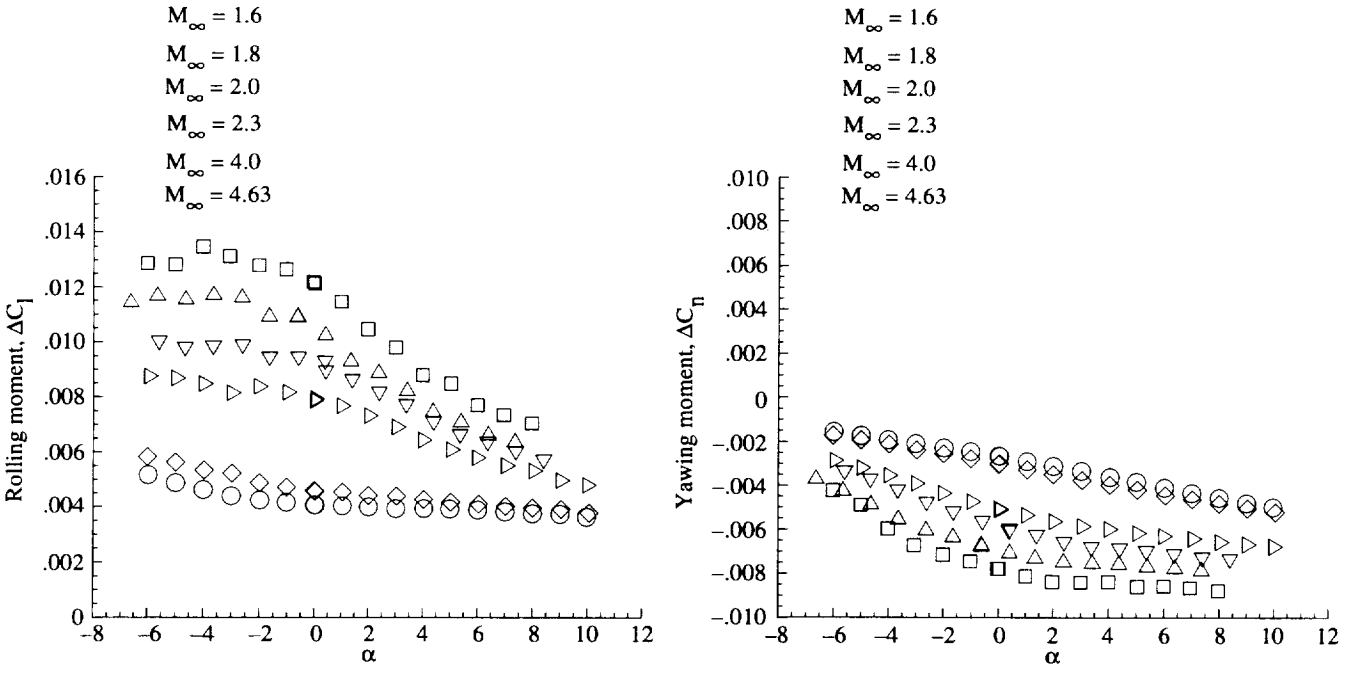

Figure 52. Aileron effectiveness on lateral-directional stability of cranked-wing fully integrated configuration; $\delta_A = \pm 20°$ and $\delta_E = 0°$.

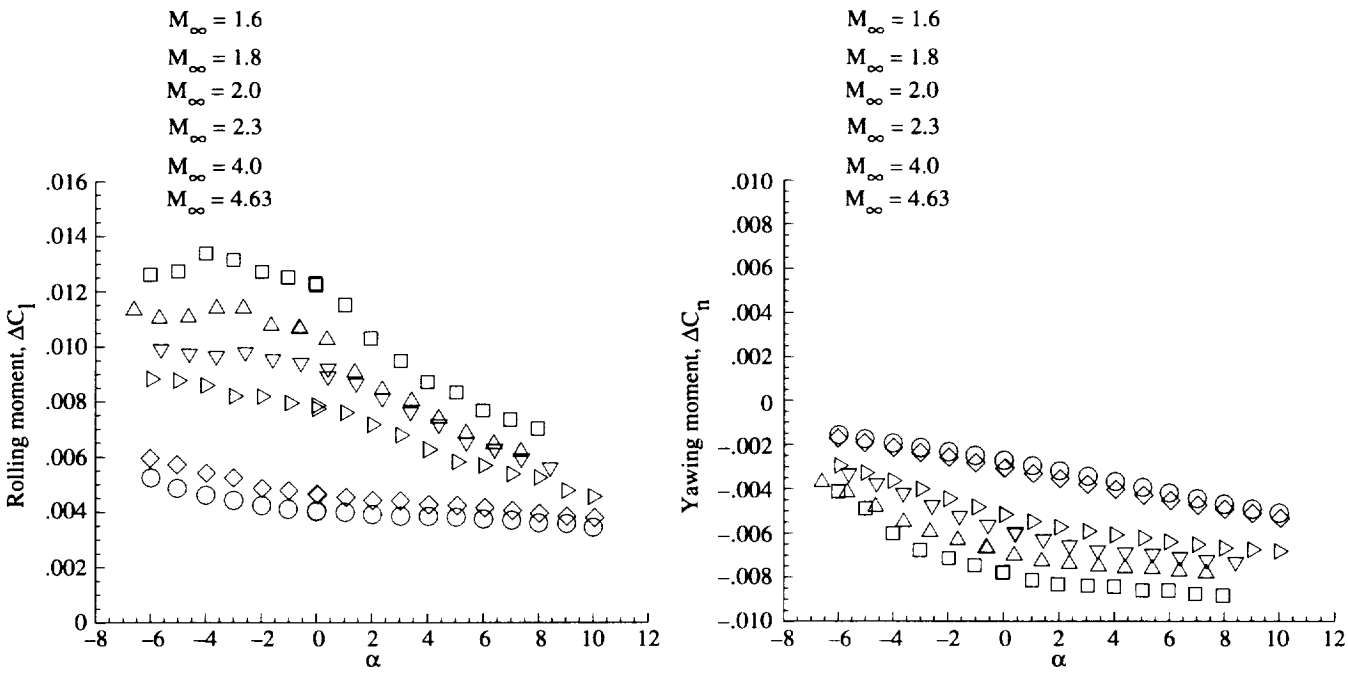

Figure 53. Combined roll/pitch effectiveness on lateral-directional stability of cranked-wing fully integrated configuration; $\delta_A = \pm 20°$ and $\delta_E = 20°$.

REPORT DOCUMENTATION PAGE

Form Approved
OMB No. 0704-0188

1. AGENCY USE ONLY *(Leave blank)*	2. REPORT DATE	3. REPORT TYPE AND DATES COVERED
	July 1996	Technical Paper

4. TITLE AND SUBTITLE
Aerodynamic Characteristics of Two Waverider-Derived Hypersonic Cruise Configurations

5. FUNDING NUMBERS
WU 466-02-01-01

6. AUTHOR(S)
Charles E. Cockrell, Jr., Lawrence D. Huebner, and Dennis B. Finley

7. PERFORMING ORGANIZATION NAME(S) AND ADDRESS(ES)
NASA Langley Research Center
Hampton, VA 23681-0001

8. PERFORMING ORGANIZATION REPORT NUMBER
L-17479

9. SPONSORING/MONITORING AGENCY NAME(S) AND ADDRESS(ES)
National Aeronautics and Space Administration
Washington, DC 20546-0001

10. SPONSORING/MONITORING AGENCY REPORT NUMBER
NASA TP-3559

11. SUPPLEMENTARY NOTES
Cockrell and Huebner: Langley Research Center, Hampton, VA; Finley: Lockheed-Fort Worth Company, Fort Worth, TX.

12a. DISTRIBUTION/AVAILABILITY STATEMENT
Unclassified–Unlimited
Subject Category 02
Availability: NASA CASI (301) 621-0390

12b. DISTRIBUTION CODE

13. ABSTRACT *(Maximum 200 words)*
An evaluation was made on the effects of integrating the required aircraft components with hypersonic high-lift configurations known as waveriders to create hypersonic cruise vehicles. Previous studies suggest that waveriders offer advantages in aerodynamic performance and propulsion/airframe integration (PAI) characteristics over conventional non-waverider hypersonic shapes. A wind-tunnel model was developed that integrates vehicle components, including canopies, engine components, and control surfaces, with two pure waverider shapes, both conical-flow-derived waveriders for a design Mach number of 4.0. Experimental data and limited computational fluid dynamics (CFD) solutions were obtained over a Mach number range of 1.6 to 4.63. The experimental data show the component build-up effects and the aerodynamic characteristics of the fully integrated configurations, including control surface effectiveness. The aerodynamic performance of the fully integrated configurations is not comparable to that of the pure waverider shapes, but is comparable to previously tested hypersonic models. Both configurations exhibit good lateral-directional stability characteristics.

14. SUBJECT TERMS
Hypersonic cruise; Waveriders; Airbreathing vehicles

15. NUMBER OF PAGES
73

16. PRICE CODE
A04

17. SECURITY CLASSIFICATION OF REPORT	18. SECURITY CLASSIFICATION OF THIS PAGE	19. SECURITY CLASSIFICATION OF ABSTRACT	20. LIMITATION OF ABSTRACT
Unclassified	Unclassified	Unclassified	